

1 **Title: Neural Circuit Underlying Individual differences in Visual Escape**
2 **Habituation**

3 **SUMMARY:**

4 Emotions, like fear, are internal states enabling organisms to effectively confront
5 environmental threats. When repeatedly exposed to predators, individuals show
6 divergent adaptive responses. However, the neural circuit mechanisms underlying
7 individual differences in to repeated threats remain largely unknown. Here, we identify
8 two distinct types of visual escape—consistent escape (T1) and rapid habituation (T2)
9 —with unambiguous arousal states to repetitive threat stimuli. We systematically
10 investigate distinct pathways originating from the superior colliculus (SC) and insula
11 that project to the basolateral amygdala (BLA), with relay stations in the mediodorsal
12 thalamus (MD) and ventral tegmental area (VTA), mediating T1 and T2 behavioral
13 types. Additionally, we identify the MD as a critical hub integrating SC and insula
14 inputs, projecting to the BLA and contributing to reduced arousal and attenuated
15 defensive behaviors against looming stimuli. Our findings offer significant insights into
16 the mechanisms of internal states, arousal modulation, and behavioral adaptability.

17
18
19
20

21 **Authors:** Xuemei Liu^{1-4,6#*}, Juan Lai^{1-2,6#}, Chuanliang Han^{1-2,6,#}, Kang Huang¹⁻², Qin
22 Yang¹⁻², Yuanming Liu¹⁻², Xutao Zhu¹⁻², Pengfei Wei¹⁻⁴, Liming Tan¹⁻³, Fuqiang Xu¹⁻
23 ³, Liping Wang^{1-5*}

24 ¹CAS Key Laboratory of Brain Connectome and Manipulation, Shenzhen–Hong Kong Institute of Brain
25 Science Shenzhen Institute of Advanced Technology, Chinese Academy of Sciences, Shenzhen, 518055,
26 China

27 ²Guangdong Provincial Key Laboratory of Brain Connectome and Behavior, Brain Cognition and Brain
28 Disease Institute, Shenzhen Institute of Advanced Technology, Chinese Academy of Sciences, Shenzhen
29 518055, China

30 ³University of Chinese Academy of Sciences, Beijing, 10049, China

31 ⁴Key Laboratory of Brain Cognition and Brain-inspired Intelligence Technology, Center for Excellence in
32 Brain Science and Intelligence Technology, Chinese Academy of Sciences

33 ⁵Lead contact corresponding lp.wang@siat.ac.cn

34 ⁶These author contribute equally.

35 ***Corresponding author:**

36 Xuemei Liu
37 Email: xm.liu@siat.ac.cn
38 Liping Wang
39 Email: lp.wang@siat.ac.cn

40
41 **Keywords:** Visual escape, Individual differences, Arousal, Habituation, Superior
42 Colliculus, Insula cortex, Basolateral Amygdala

43
44 **Author Contributions:**

45 X.L. and L.W. designed the project, X.L., J.L., Q.Y., Y.L., X.Z. executed the
46 experiments. X.L., C.H., J.L., K.H., analyzed the data. X.L., C.H., L.W. wrote the
47 manuscript. X.L., L.W., P.W., L.T., F.X. revised the manuscript. L.W. and X.L.
48 supervised the project.

49

50

51

52 **Conflicts of interest statement:**

53 The co-authors declare that the research was conducted in the absence of any
54 commercial or financial relationships that could be construed as a potential conflict of
55 interest.

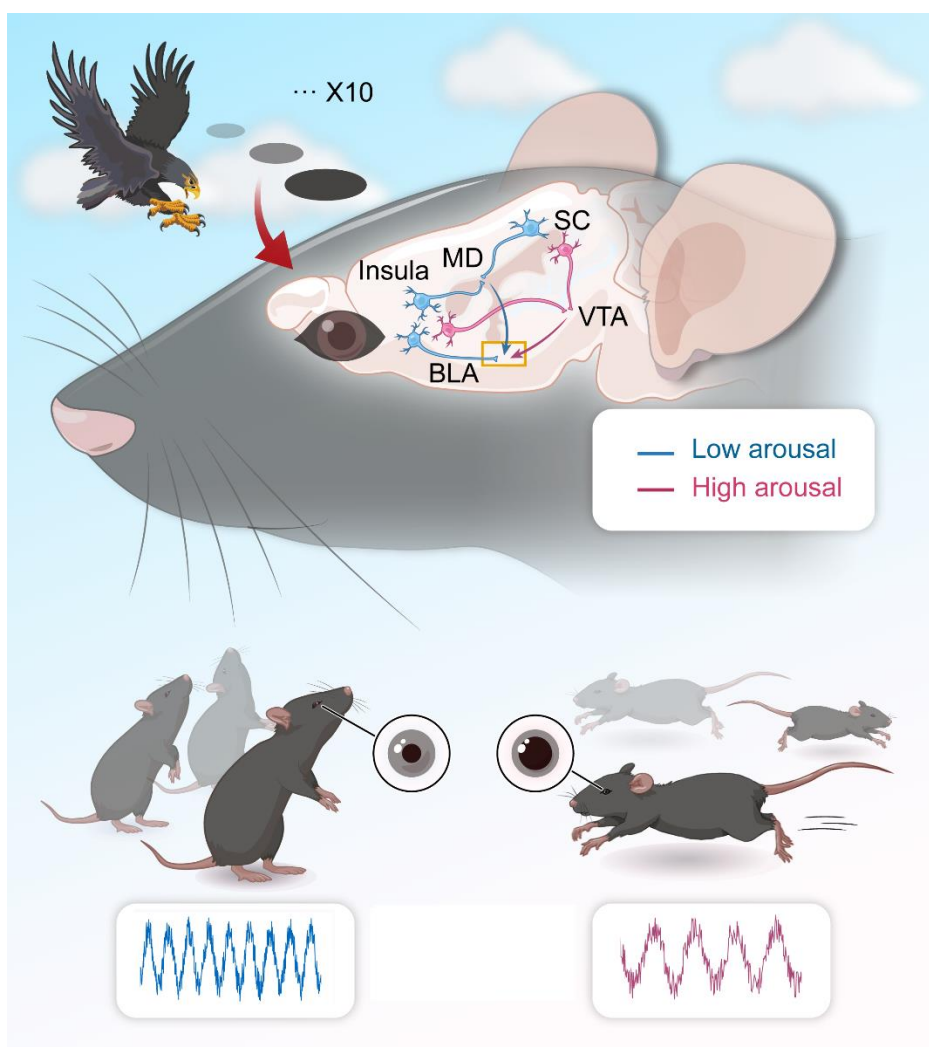
56

57 **Acknowledgments:**

58 We thank Peng Cao for providing the FosTrap2 mice line (Jackson Laboratory). This
59 work was funded by the National Natural Science Foundation of China (32230042 to
60 L.W., 32371069 to X.L.,); Strategic Priority Research Program of CAS
61 (XDB32030100), Financial Support for Outstanding Talents Training Fund in
62 Shenzhen (L.W.); STI2030-Major Projects-2022ZD0211700, the Ten Thousand Talent
63 Program, the Chang Jiang Scholars Program, Financial Support for Outstanding Talents
64 Training Fund in Shenzhen (L.W.);Guangdong Province Basic Research Grant
65 (2023B1515040009) and the China Postdoctoral Science Foundation (2022M723299,
66 2023T160666).

67

68



69

70 **Graph Abstract**

71 **In brief**

72 We identify two distinct visual escape behaviors—consistent escape (T1) and rapid
73 habituation (T2)—linked to unique SC and insula pathways projecting to the BLA via
74 MD and VTA. The MD acts as a hub integrating sensory inputs to modulate arousal
75 and defensive responses. These findings advance our understanding of the neural
76 mechanisms driving internal states, arousal modulation, and behavioral adaptability.

77

78 **Highlights**

- 79 ● We identify two distinct visual escape behaviors with unambiguous arousal
80 states—consistent escape (T1) and rapid habituation (T2) —to repeated
81 looming stimuli.
- 82 ● The SC-VTA-BLA pathway mediated T1 behavioral type, while the SC-
83 MD-BLA pathway mediated T2 type.
- 84 ● MD as a central hub integrating SC and insula inputs to modulate arousal
85 and defensive behavioral adaptation.

86

87 **Introduction**

88 Emotional responses, including fear behaviors, are hallmark features of internal
89 states, hardwired in the brain to facilitate threat avoidance and coping^{1–5}. Arousal states
90 typically heighten the probability of exhibiting specific behaviors or influence the
91 behavioral choice^{4,6–8}. Notably, an animal's capacity to quickly adapt to external
92 challenges is driven by the biological significance of repeated predator encounters
93 compared to singular events. Individuals, across various species, exposed to recurring
94 threats may express two distinct coping strategies habituation and sensitization
95 dependent on sensory inputs, internal states, and previous experiences^{9–12}. The neural
96 circuits underpinning individual internal state regulation and habituation in response to
97 repeated predator threats remain largely elusive.

98 Visual looming stimuli (LS), which simulate predator approach, elicit strong
99 innate defensive responses across various species^{13–18}, along with habituation behaviors
100 upon repeated exposure^{19–23}. Effective adaptive defense mechanisms necessitate a
101 heightened state of awareness, an optimal level of arousal, and a focus on visually
102 salient and biologically relevant stimuli. Previous research indicates that the magnitude
103 and intensity of innate escape responses are influenced by external environmental
104 factors and the organism's internal state^{24–31}. Despite these insights, the neural circuitry
105 underlying the modulation of arousal levels and habituation in response to repeated LS
106 remains inadequately understood.

107 The superior colliculus (SC), a retina-receipt brainstem that receive inputs from
108 multiple sensory modalities and controls orienting, saccadic eye movement and
109 defensive behaviors³². It is instrumental in capturing and allocating attention, directing
110 both eye movements and covert attention toward visually salient stimuli^{33–36}. The
111 "subcortical route to the amygdala," also known as the "innate alarm system," originates
112 from the SC and bypasses the cortex, serving as a rapid and efficient shortcut for threat
113 avoidance³⁶. The ventral tegmental area (VTA) is a SC-originating pathway, which is
114 a crucial component in motivation control, value evaluation, and salience detection
115 following an aversive stimulus^{37–39} and even innate defensive responses^{40,41}.

116 Consequently, the SC-VTA-amygala pathway is well-suited for facilitating fear
117 learning and mediating habituation or dishabituation effects⁴⁰. Additionally, the
118 mediiodorsal thalamus (MD), a downstream target of the SC, is involved in processing
119 visual salience and arousal levels induced by sensory stimuli⁴²⁻⁴⁴. The SC-MD-
120 amygdala pathway has been identified as mediating persistent fear attenuation,
121 contributing to the underlying neurobiology that modulates visual-attentional processes
122 ⁴⁵.

123 The insular cortex is pivotal in detection internal states, risk assessment, decision-
124 making, and promoting bodily and self-awareness⁴⁶⁻⁵⁰. Previous research demonstrates
125 that the insula processes fear-related emotions by modulating the amygdala, a key node
126 in subcortical pathways⁵¹⁻⁵³. However, the coordination between insula cortex and
127 subcortical pathways that modulate defensive arousal and habituation to repeated
128 predator exposures via the amygdala remains underexplored. Surprisingly, we found
129 that approximately one-third of the mice (T2) exhibited rapid habituation characterized
130 by low arousal (as indicated by decreased pupil size) but high attention levels
131 (demonstrated by elevated rearing frequency) in response to repeated LS. Conversely,
132 the remaining two-thirds of the mice (T1) consistently exhibited escape responses with
133 corresponding arousal and rearing frequencies. We identified parallel pathways
134 originating from the SC and insula that project to the amygdala, using relay stations in
135 the MD and VTA, which separately mediate the T1 and T2 behavioral responses. Our
136 study systematically explores the neural circuit mechanisms underlying distinct
137 behavioral choices when facing repeated threats, shedding light on their internal states,
138 arousal, and behavioral adaptability.

139

140 **RESULTS**

141 **Individual Variability in Escape Habituation to Repeated Looming Stimuli**

142 Previous studies have established that looming stimuli (LS) reliably elicit innate escape
143 behaviors. To explore the escape habituation to repeated LS, we exposed 52 wildtype
144 (WT) adult male mice to 10 LS trials per session, with each trial lasting 5.5 seconds
145 and inter-stimulus intervals (ISIs) of no less than 2 minutes ([Figure 1A](#)). Notably, our
146 findings revealed individual differences in escape behavior. Only one mouse (~2%)
147 exhibited no response, while the remaining 51 mice were categorized into two distinct
148 response types. Mice with an average response latency shorter than 5.5 seconds were
149 designated as "consistent escape" (Type I, T1, n=35, 67.31%), while those with
150 latencies exceeding 5.5 seconds were identified as exhibiting "rapid habituation" (Type
151 II, T2, n=16, 30.77%) ([Figure 1B](#)). Compared to the T1 group, mice in the T2 group
152 had a significantly lower average escape proportion (35.63% vs. 98.57) ([Figure 1C](#)),
153 and exhibited longer average response latency (17.78±1.10 s vs 1.56±1.10 s), longer
154 return time (19.86±0.31 s vs 2.91±1.09 s), and spent less time in the nest (24.68±0.59 s
155 vs 72.96±1.15 s) ([Figure 1F,G](#)).

156 Analysis of average scores over trials revealed that the T2 group showed increased
157 latency and time to return to the nest across initial, middle, and final trial phases ([Figure](#)
158 [S1](#)).

159 Non-selective attention (NSA), characterized by scanning, orienting, and detecting
160 stimuli, correlates with rearing frequency in novel settings ⁵⁴⁻⁵⁶. The T2 group
161 consistently exhibited higher rearing frequency (RF) across all trials compared to the
162 T1 group ([Figure 1D](#)). Remarkably, in the T2 group, RF significantly increased
163 following LS onset, in contrast to a decrease observed in the T1 group. No RF
164 differences were noted between T1 and T2 groups before LS onset, indicating stimulus-
165 specific RF patterns ([Figure 1E](#)). To assess arousal state, we performed pupillometry
166 on head-fixed, awake mice placed on a ball treadmill ([Figure 1H](#)). Pupil size, measured
167 10 seconds post-LS onset, was significantly larger in the T1 group compared to the T2
168 group ([Figure 1 IJK](#)). No significant pupil size differences were observed between

169 groups prior to or during LS exposure. Collectively, our results demonstrate that the T2
170 group, characterized by higher habituation, exhibits enhanced stimuli-evoked NSA and
171 reduced arousal in response to repeated LS presentations.

172

173 **Divergent Superior Colliculus Pathways Modulate Arousal and Escape Behavior**

174 To elucidate the role of SC neurons activated during habituation to LS, we employed
175 the FosTRAP2 technique ^{57,58}. On day 1, AAV5-DIO-EGFP was injected unilaterally
176 into the SC of FosTRAP2 mice. On day 3, FosFRAP2 mice were injected with
177 tamoxifen and exposed to repeated LS to activate TRAPed cells. On day 24, FosFRAP2
178 mice were exposed to LS again before perfusion (Figure 2A). Our results showed a
179 higher density of EGFP+ SC neurons in the T1 group compared to the T2 group,
180 suggesting the SC's involvement in LS habituation and attenuation of innate escape
181 behavior (Figure 2B-C).

182 We investigated whether the SC-VTA and SC-MD pathways differentially affect
183 arousal during LS habituation. Using AAV5-CaMKIIα-ChR2-mcherry injections into
184 the SC and optic fiber implantation into the MD and VTA (Figure 2D-E), we performed
185 pupillometry on head-fixed mice. Optogenetic stimulation (473 nm, 2.5 s, 20 Hz, 50
186 pulses) altered pupil size during LS presentation. SC-MD activation led to pupil
187 constriction, while SC-VTA activation resulted in pupil dilation (Figure 2F-G). Before
188 optogenetic stimulation (OS), there was no significant difference in pupil size between
189 the groups. However, the mean pupil size during and after OS was significantly larger
190 in the SC-VTA group than in the SC-MD group (Figure 2H-I).

191 Considering the larger pupil size in the T1 group and following SC-VTA activation, we
192 hypothesized that repeated SC-VTA stimulation would elicit T1-like behavior. Indeed,
193 repeated SC-VTA OS resulted in stable escape behavior in an open field with shelter,
194 mimicking T1 group responses (Figure S2).

195 Further investigations assessed the SC pathways' roles via ChR2-mcherry expression
196 in SC neurons. SC-MD OS increased rearing frequency, response latency, and return
197 time but SC-VTA OS did not, indicating SC-MD OS disrupts looming-induced escape
198 behaviors. Thus, SC-MD activation decreased arousal and increased NSA, impairing

199 innate escape, whereas SC-VTA activation increased arousal without affecting NSA or
200 escape behavior.

201 To trace SC projections, we injected rabies virus (RV) conjugated with dsRed into the
202 VTA and RV-EGFP into the MD, quantifying labeled neurons across the brain. Among
203 retrogradely labeled neurons, 51% in the SC were from the MD, and 63% from the
204 VTA, with 14.4% co-labeled from both sites (Figure S3), indicating SC collaterals
205 project to both MD and VTA.

206 To rule out collateral effects, we blocked SC action potential backpropagation using
207 0.3 μ l of 4% bupivacaine ⁵⁹. Bupivacaine had no impact on behavior change during
208 either SC-VTA or SC-MD pathway activation in an open field with shelter paradigm
209 (Figure S3), suggesting parallel processing between SC pathways modulates variability
210 in innate escape responses.

211

212 **VTA-projecting and MD-projecting SC neurons functionally target the BLA**

213 The amygdala is pivotal for both conditioned and innate fear responses, with the
214 basolateral amygdala (BLA) playing a central role in encoding threat-related
215 information ^{3,60}. We investigated whether SC neurons projecting to the VTA and the
216 MD converge on the BLA. Using AAV1-mediated anterograde transsynaptic tagging
217 ⁶¹, we injected AAV1-Cre into the SC, followed by injections of AAV5-DIO-EYFP
218 into the MD and AAV5-DIO-mCherry into the VTA (Figure 3A). Cre expression
219 revealed overlapping axonal projections in the BLA, indicating that both VTA-
220 projecting and MD-projecting SC neurons innervate a common region within the BLA
221 (Figure 3B). Fluorescence density analysis showed that VTA-projecting SC neurons
222 primarily innervated the medial BLA, while MD-projecting neurons targeted the
223 anterior and posterior parts (Figure 3C).

224

225 **SC Pathways Modulate Connectivity and Oscillations in the BLA**

226 To explore this functional connectivity further, we conducted *in vivo* multi-channel
227 recordings in the BLA and pupillometry during selective optogenetic activation of SC-
228 VTA and SC-MD pathways (Figure 4A). OS of the SC-VTA pathway caused an

229 increase in pupil size, while SC-MD activation led to a decrease ([Figure 4B](#)). Neuronal
230 firing rates within the BLA significantly changed following the activation of each
231 pathway; SC-MD activation affected 11% of neurons (9% excitation, 2% inhibition),
232 and SC-VTA activation affected 9% (7% excitation, 2% inhibition) ([Figure S4,S5](#)).
233 The analysis of local field potential (LFP) power spectra in the BLA revealed distinct
234 oscillatory patterns associated with each pathway. SC-VTA activation led to increased
235 power in low-frequency bands (theta and alpha), whereas SC-MD activation enhanced
236 power in higher frequency bands (beta and low gamma) ([Figure 4D-F](#)). These findings
237 underscore the distinct oscillatory characteristics modulated by SC-MD and SC-VTA
238 pathways, highlighting their unique roles in amygdala circuitry and fear-related
239 behaviors.
240

241 **Distinct Arousal and Defense Modulation by Divergent Insula Cortex Pathways**

242 The insula cortex, a key integration center for sensory feedback and autonomic arousal
243 ⁴⁶, projects to both the MD and the VTA, as confirmed by our previous tracing studies
244 ([Figure S3](#)). To assess whether the insula-MD and insula-VTA pathways modulate
245 arousal differently, we used optogenetic manipulation and pupillometry ([Figure 5A](#)).
246 AAV5-CaMKIIα-ChR2-mCherry was injected into the insula cortex, with optical fibers
247 placed in the MD and VTA ([Figure 5D](#)). OS of MD terminals significantly decreased
248 pupil size, while OS of VTA terminals increased pupil size ([Figure 5B, 5E-F](#)). No
249 significant differences in baseline pupil size were observed between groups prior to OS
250 ([Figure 5E-F](#)). During and post-stimulation, pupil size was smaller in the insula-MD
251 group than in the insula-VTA group, indicating distinct effects on arousal ([Figure 5E-F](#)).
252

253 We explored the involvement of these pathways during LS presentations by testing
254 mice with ChR2-mCherry in insula cortex neurons. Activation of the insula-MD
255 pathway increased rearing frequency, response latency, and return time, while reducing
256 time spent in the nest. However, insula-VTA activation did not affect LS-evoked
257 behaviors. Thus, insula-MD activation decreased arousal levels and increased non-

258 selective attention (NSA), diminishing LS-induced escape responses, whereas insula-
259 VTA activation heightened arousal without influencing escape ([Figure 5C-D, 5G-H](#)).
260 To further investigate functional connectivity, we conducted *in vivo* multi-channel
261 recordings in the BLA and pupillometry during insula-MD pathway activation ([Figure](#)
262 [6A](#)). Insula-MD stimulation decreased pupil size ([Figure 6B](#)) and altered neuronal
263 firing rates in the BLA, with 30% of neurons responding (8% excitation, 22% inhibition)
264 ([Figure S6](#)); Although LFP power spectra in the BLA were analyzed, insula-MD
265 activation did not significantly alter powers across frequency bands ([Figure 6D-F](#)).
266 We examined whether the insula-BLA pathway impacts arousal using optogenetic
267 manipulation and pupillometry ([Figure 7](#)). We performed optogenetic manipulation
268 combined with pupillometry recording as described above ([Figure 7A](#)). Following
269 ChR2-mCherry injections into the insula cortex and fiber placement in the BLA, OS
270 reduced pupil size ([Figure 7 B-D](#)). Insula-BLA activation increased rearing frequency,
271 response latency, and return time, suggesting reduced LS-induced escape behaviors. In
272 further recordings ([Figure 8A](#)), insula-BLA activation affected 42% of BLA neurons
273 (40% excitation, 2% inhibition, [Figure S7](#)) and decreased pupil size ([Figure 8B-E](#)); LFP
274 power analyses showed no significant changes, contrasting with SC-MD activation and
275 suggesting a more pronounced role for subcortical versus cortical pathways in
276 modulating escape responses ([Figure 8D-F](#)).

277

278 **Discussion**

279 In the study, we found that rodents exhibit two types of behavioral responses to repeated
280 light stimulation (LS): "consistent escape" (T1) and "rapid habituation" (T2), each
281 characterized by distinct pupil sizes and rearing frequencies. Additionally, we identified
282 divergent pathways originating from the SC and the insula, which project to BLA and
283 contribute to different levels of defensive arousal and habituation responses to repeated
284 LS. Furthermore, the state of defensive arousal and the manipulation of separate circuits
285 play distinct roles in regulating the power of LFP in the BLA. This research enhances
286 our understanding of how internal states, such as arousal and fear, are modulated at the
287 neural level, and highlights the complexity of these processes.

288 Individual differences are crucial as they supply the raw materials for natural
289 selection, as evidenced by the variability in individual adaptations to repeated predator
290 encounters^{62,63}. The behavioral adaptation need optimizing perception and attention by
291 conserving cognitive resources, enhancing biological salience detection thereby enable
292 threat detection and resilience^{52,64}. The SC's well-documented functions in detecting
293 and directing attention to salient visual stimuli align with its involvement in both T1
294 and T2 behaviors. In T1, consistent escape behavior is driven by sustained activation
295 of the SC-VTA-amygda pathway, maintaining the high arousal needed for continuous
296 defensive responses, which, despite its energy cost, this sensitization-like response
297 enhances survival probability in environments with unpredictable threats⁶⁵. This
298 pathway's role in reinforcement fear learning and mediating potential sensitization or
299 dishabituation effects is consistent with its established contributions to innate defensive
300 responses and motivational control^{32,37}.

301 Conversely, T2 behavior involves rapid habituation via transient SC-MD-
302 amygdala pathway or insula-MD-amygda pathway activation, swiftly reducing
303 arousal and defensive responses. This rapid habituation aligns with previous studies in
304 larval zebrafish, crabs, and other species⁶⁶⁻⁶⁸, enabling animals to disregard irrelevant
305 stimuli and focus on biologically significant threats, thereby enhancing adaptive
306 survival by reducing responses to non-threatening cues. The SC also influences higher-

307 order regions by directing attention in a bottom-up manner ^{69–71}. These findings
308 underscore the role of a “visual salience network”, comprising subcortical pathways
309 and top-down cortical visuomotor control, in coordinating visual attention towards
310 novel, salient stimuli and unexpected threats ^{49,72}.

311 Our study investigates the relationship between arousal and non-selective attention
312 in rodents, as indexed by pupil size and rearing frequency, respectively. Traditionally,
313 rearing is associated with non-selective attention, while arousal definitions vary,
314 sometimes linked to awareness or energy states. Despite extensive research on
315 neuromodulators affecting pupil size, the neural circuitry underpinning rearing
316 frequency remains less understood, and their correlation unexamined. We found T1
317 subjects exhibit high pupil dilation and low rearing frequency, whereas T2 subjects
318 show the opposite. This aligns with our optogenetic and electrophysiological data,
319 suggesting distinct neural pathways from the SC and insula to the amygdala (via the
320 VTA or MD) govern these responses. Interestingly, rearing frequency differences only
321 emerged post-stimulus (Fig 1 E), indicating a stimulus-specific adaptation rather than
322 innate resting state differences. This reveals a dissociation, and even a counterbalance,
323 between arousal and non-selective attention during repeated threat exposure.

324 Our electrophysiological findings show differences between VTA- and MD-
325 projecting SC neurons targeting the BLA: activation of the SC-MD circuit increases
326 high-frequency beta (12-30 Hz) and low gamma (30-60 Hz) oscillations, while SC-
327 VTA activation boosts lower-frequency theta (3-7 Hz) and alpha (7-12 Hz) oscillations.
328 These patterns align with the notion that attention correlates positively with high-
329 frequency and negatively with low-frequency oscillations. Elevated rearing frequency
330 upon SC-MD activation suggests heightened attention due to increased beta and low
331 gamma oscillatory power. Conversely, SC-VTA activation suggests diminished
332 attention, correlating with enhanced engagement in escape behavior and increased
333 lower-frequency power. Activation of the insula-MD pathway results in different
334 oscillatory changes than SC-MD, less significantly altering attention as indicated by
335 pupil size changes. This complexity in the insula's regulation of the BLA suggests
336 intricate interactions worth further investigation to understand MD and VTA functions.

337 This study underscores how distinct neural pathways from shared sensory inputs
338 lead to varied behavioral outcomes based on individual internal states. By identifying
339 the MD as a common hub projecting to the amygdala from both the SC and insula, we
340 unveil the neural basis for modulating attention and arousal in response to threats. Our
341 findings enhance understanding of the interplay between sensory processing and
342 emotional states in behavior, offering a framework for future exploration of these
343 adaptable neural circuits, central to survival in dynamic environments.

344 Maladaptive behaviors in response to extreme fear can lead to either heightened
345 sensitivity to harmless stimuli (overreaction) or reduced detection and response to
346 actual threats (underreaction)^{73–75}. In humans, these responses are common in fear-
347 related disorders such as phobias, anxiety, PTSD, and delusional disorders.

348 Our findings have significant implications for understanding individual variability
349 in emotional processing and resilience. The ability to rapidly habituate to repeated
350 threats could confer advantages in certain environments, reducing stress-related
351 pathologies. Conversely, a consistent escape response might be advantageous in
352 environments where threats are unpredictable and potentially lethal. Understanding the
353 neural circuits and molecular mechanisms behind individual differences in habituation
354 to repeated predator exposures could inform personalized treatments for
355 neuropsychiatric conditions³⁶. By concentrating on evolutionarily conserved circuits
356 like the SC – MD – amygdala pathway, our research establishes a physiological basis
357 for developing potential therapies. The further detailed analysis of the molecular
358 mechanisms of the subcortical pathway could enhance the translational value of
359 research by identifying a key target for PTSD treatment^{45,76,77}.

360

361 **References**

- 362 1. Anderson, D.J., and Adolphs, R. (2014). A Framework for Studying Emotions across Species.
363 *Cell* *157*, 187–200. <https://doi.org/10.1016/j.cell.2014.03.003>.
- 364 2. LeDoux, J. (2012). Rethinking the emotional brain. *Neuron* *73*, 653–676.
365 <https://doi.org/10.1016/j.neuron.2012.02.004>.
- 366 3. Gross, C.T., and Canteras, N.S. (2012). The many paths to fear. *Nat Rev Neurosci* *13*, 651–
367 658. <https://doi.org/10.1038/nrn3301>.
- 368 4. Flavell, S.W., Gogolla, N., Lovett-Barron, M., and Zelikowsky, M. (2022). The emergence and
369 influence of internal states. *Neuron* *110*, 2545–2570.
370 <https://doi.org/10.1016/j.neuron.2022.04.030>.
- 371 5. Tseng, Y.-T., Schaefer, B., Wei, P., and Wang, L. (2023). Defensive responses: behaviour, the
372 brain and the body. *Nat Rev Neurosci* *24*, 655–671. <https://doi.org/10.1038/s41583-023-00736-3>.
- 374 6. Anderson, D.J. (2016). Circuit modules linking internal states and social behaviour in flies and
375 mice. *Nat Rev Neurosci* *17*, 692–704. <https://doi.org/10.1038/nrn.2016.125>.
- 376 7. McCormick, D.A., Nestvogel, D.B., and He, B.J. (2020). Neuromodulation of Brain State and
377 Behavior. *Annu Rev Neurosci* *43*, 391–415. <https://doi.org/10.1146/annurev-neuro-100219-105424>.
- 379 8. Hulsey, D., Zumwalt, K., Mazzucato, L., McCormick, D.A., and Jaramillo, S. (2024).
380 Decision-making dynamics are predicted by arousal and uninstructed movements. *Cell Rep* *43*,
381 113709. <https://doi.org/10.1016/j.celrep.2024.113709>.
- 382 9. Thompson, R.F., and Spencer, W.A. (1966). Habituation: A model phenomenon for the study
383 of neuronal substrates of behavior. *Psychol Rev* *73*, 16–43. <https://doi.org/10.1037/h0022681>.
- 384 10. Steketee, J.D. (2016). The Neurobiology of Behavioral Sensitization. In *Neurobiology of
385 Addictions* (Oxford University Press), pp. 138–152.
386 <https://doi.org/10.1093/med/9780199367894.003.0006>.
- 387 11. Rankin, C.H., Abrams, T., Barry, R.J., Bhatnagar, S., Clayton, D.F., Colombo, J., Coppola, G.,
388 Geyer, M.A., Glanzman, D.L., Marsland, S., et al. (2009). Habituation revisited: An updated

- 389 and revised description of the behavioral characteristics of habituation. *Neurobiol Learn Mem*
390 92, 135–138. <https://doi.org/10.1016/j.nlm.2008.09.012>.
- 391 12. Hattori, D., Aso, Y., Swartz, K.J., Rubin, G.M., Abbott, L.F., and Axel, R. (2017).
392 Representations of Novelty and Familiarity in a Mushroom Body Compartment. *Cell* 169, 956–
393 969.e17. <https://doi.org/10.1016/j.cell.2017.04.028>.
- 394 13. Yilmaz, M., and Meister, M. (2013). Rapid Innate Defensive Responses of Mice to Looming
395 Visual Stimuli. *Current Biology* 23, 2011–2015. <https://doi.org/10.1016/j.cub.2013.08.015>.
- 396 14. Wei, P., Liu, N., Zhang, Z., Liu, X., Tang, Y., He, X., Wu, B., Zhou, Z., Liu, Y., Li, J., et al.
397 (2015). Processing of visually evoked innate fear by a non-canonical thalamic pathway. *Nat
398 Commun* 6, 6756. <https://doi.org/10.1038/ncomms7756>.
- 399 15. Shang, C., Chen, Z., Liu, A., Li, Y., Zhang, J., Qu, B., Yan, F., Zhang, Y., Liu, W., Liu, Z., et
400 al. (2018). Divergent midbrain circuits orchestrate escape and freezing responses to looming
401 stimuli in mice. *Nat Commun* 9, 1232. <https://doi.org/10.1038/s41467-018-03580-7>.
- 402 16. Salay, L.D., Ishiko, N., and Huberman, A.D. (2018). A midline thalamic circuit determines
403 reactions to visual threat. *Nature* 557, 183–189. <https://doi.org/10.1038/s41586-018-0078-2>.
- 404 17. Evans, D.A., Stempel, A.V., Vale, R., Ruehle, S., Lefler, Y., and Branco, T. (2018). A synaptic
405 threshold mechanism for computing escape decisions. *Nature* 558, 590–594.
406 <https://doi.org/10.1038/s41586-018-0244-6>.
- 407 18. Huang, L., Yuan, T., Tan, M., Xi, Y., Hu, Y., Tao, Q., Zhao, Z., Zheng, J., Han, Y., Xu, F., et
408 al. (2017). A retinoraphe projection regulates serotonergic activity and looming-evoked
409 defensive behaviour. *Nat Commun* 8. <https://doi.org/10.1038/ncomms14908>.
- 410 19. Hayes, W.N., and Saiff, E.I. (1967). Visual alarm reactions in turtles. *Anim Behav* 15, 102–
411 106. [https://doi.org/10.1016/S0003-3472\(67\)80018-6](https://doi.org/10.1016/S0003-3472(67)80018-6).
- 412 20. Matheson, T., Rogers, S.M., and Krapp, H.G. (2004). Plasticity in the Visual System Is
413 Correlated With a Change in Lifestyle of Solitarious and Gregarious Locusts. *J Neurophysiol*
414 91, 1–12. <https://doi.org/10.1152/jn.00795.2003>.
- 415 21. Oliva, D., Medan, V., and Tomsic, D. (2007). Escape behavior and neuronal responses to
416 looming stimuli in the crab Chasmagnathus granulatus (Decapoda: Grapsidae). *J Exp Biol* 210,
417 865–880. <https://doi.org/10.1242/jeb.02707>.

- 418 22. Mancienne, T., Marquez-Legorreta, E., Wilde, M., Piber, M., Favre-Bulle, I., Vanwalleghem,
419 G., and Scott, E.K. (2021). Contributions of Luminance and Motion to Visual Escape and
420 Habituation in Larval Zebrafish. *Front Neural Circuits* *15*.
421 <https://doi.org/10.3389/fncir.2021.748535>.
- 422 23. Marquez-Legorreta, E., Constantin, L., Piber, M., Favre-Bulle, I.A., Taylor, M.A., Blevins,
423 A.S., Giacometto, J., Bassett, D.S., Vanwalleghem, G.C., and Scott, E.K. (2022). Brain-wide
424 visual habituation networks in wild type and fmr1 zebrafish. *Nat Commun* *13*, 895.
425 <https://doi.org/10.1038/s41467-022-28299-4>.
- 426 24. Zhao, X., Liu, M., and Cang, J. (2014). Visual Cortex Modulates the Magnitude but Not the
427 Selectivity of Looming-Evoked Responses in the Superior Colliculus of Awake Mice. *Neuron*
428 *84*, 202–213. <https://doi.org/10.1016/j.neuron.2014.08.037>.
- 429 25. Li, L., Feng, X., Zhou, Z., Zhang, H., Shi, Q., Lei, Z., Shen, P., Yang, Q., Zhao, B., Chen, S., et
430 al. (2018). Stress Accelerates Defensive Responses to Looming in Mice and Involves a Locus
431 Coeruleus-Superior Colliculus Projection. *Curr Biol* *28*, 859-871.e5.
432 <https://doi.org/10.1016/j.cub.2018.02.005>.
- 433 26. Liu, X., Chen, C., Liu, Y., Wang, Z., Huang, K., Wang, F., and Wang, L. (2018). Gentle
434 Handling Attenuates Innate Defensive Responses to Visual Threats. *Front Behav Neurosci* *12*.
435 <https://doi.org/10.3389/fnbeh.2018.00239>.
- 436 27. Tseng, Y.T., Zhao, B., Chen, S., Ye, J., Liu, J., Liang, L., Ding, H., Schaeck, B., Yang, Q.,
437 Wang, L., et al. (2022). The subthalamic corticotropin-releasing hormone neurons mediate
438 adaptive REM-sleep responses to threat. *Neuron* *110*, 1223-1239.e8.
439 <https://doi.org/10.1016/j.neuron.2021.12.033>.
- 440 28. Liang, F., Xiong, X.R., Zingg, B., Ji, X., Zhang, L.I., and Tao, H.W. (2015). Sensory Cortical
441 Control of a Visually Induced Arrest Behavior via Corticotectal Projections. *Neuron* *86*, 755–
442 767. <https://doi.org/10.1016/j.neuron.2015.03.048>.
- 443 29. Daviu, N., Füzesi, T., Rosenegger, D.G., Rasiah, N.P., Sterley, T.-L., Peringod, G., and Bains,
444 J.S. (2020). Paraventricular nucleus CRH neurons encode stress controllability and regulate
445 defensive behavior selection. *Nat Neurosci* *23*, 398–410. <https://doi.org/10.1038/s41593-020-0591-0>.

- 447 30. Li, C., Kühn, N.K., Alkislar, I., Sans-Dublanc, A., Zemmouri, F., Paesmans, S., Calzoni, A.,
448 Ooms, F., Reinhard, K., and Farrow, K. (2023). Pathway-specific inputs to the superior
449 colliculus support flexible responses to visual threat. *Sci Adv* 9.
450 <https://doi.org/10.1126/sciadv.ade3874>.
- 451 31. Yang, X., Liu, Q., Zhong, J., Song, R., Zhang, L., and Wang, L. (2020). A simple threat-
452 detection strategy in mice. *BMC Biol* 18, 93. <https://doi.org/10.1186/s12915-020-00825-0>.
- 453 32. Redgrave, P., and Gurney, K. (2006). The short-latency dopamine signal: a role in discovering
454 novel actions? *Nat Rev Neurosci* 7, 967–975. <https://doi.org/10.1038/nrn2022>.
- 455 33. Goldberg, M.E., and Wurtz, R.H. (1972). Activity of superior colliculus in behaving monkey.
456 II. Effect of attention on neuronal responses. *J Neurophysiol* 35, 560–574.
457 <https://doi.org/10.1152/jn.1972.35.4.560>.
- 458 34. Ignashchenkova, A., Dicke, P.W., Haarmeier, T., and Thier, P. (2004). Neuron-specific
459 contribution of the superior colliculus to overt and covert shifts of attention. *Nat Neurosci* 7,
460 56–64. <https://doi.org/10.1038/nn1169>.
- 461 35. Krauzlis, R.J., Lovejoy, L.P., and Zénon, A. (2013). Superior Colliculus and Visual Spatial
462 Attention. *Annu Rev Neurosci* 36, 165–182. <https://doi.org/10.1146/annurev-neuro-062012-170249>.
- 463 36. McFadyen, J., Dolan, R.J., and Garrido, M.I. (2020). The influence of subcortical shortcuts on
464 disordered sensory and cognitive processing. *Nat Rev Neurosci* 21, 264–276.
465 <https://doi.org/10.1038/s41583-020-0287-1>.
- 466 37. Bromberg-Martin, E.S., Matsumoto, M., and Hikosaka, O. (2010). Dopamine in Motivational
467 Control: Rewarding, Aversive, and Alerting. *Neuron* 68, 815–834.
468 <https://doi.org/10.1016/j.neuron.2010.11.022>.
- 469 38. Brischoux, F., Chakraborty, S., Brierley, D.I., and Ungless, M.A. (2009). Phasic excitation of
470 dopamine neurons in ventral VTA by noxious stimuli. *Proceedings of the National Academy of
471 Sciences* 106, 4894–4899. <https://doi.org/10.1073/pnas.0811507106>.
- 472 39. Lammel, S., Lim, B.K., Ran, C., Huang, K.W., Betley, M.J., Tye, K.M., Deisseroth, K., and
473 Malenka, R.C. (2012). Input-specific control of reward and aversion in the ventral tegmental
474 area. *Nature* 491, 212–217. <https://doi.org/10.1038/nature11527>.
- 475

- 476 40. Zhou, Z., Liu, X., Chen, S., Zhang, Z., Liu, Y., Montardy, Q., Tang, Y., Wei, P., Liu, N., Li, L.,
477 et al. (2019). A VTA GABAergic Neural Circuit Mediates Visually Evoked Innate Defensive
478 Responses. *Neuron* *103*, 473-488.e6. <https://doi.org/10.1016/j.neuron.2019.05.027>.
- 479 41. Barbano, M.F., Wang, H.L., Zhang, S., Miranda-Barrientos, J., Estrin, D.J., Figueroa-
480 González, A., Liu, B., Barker, D.J., and Morales, M. (2020). VTA Glutamatergic Neurons
481 Mediate Innate Defensive Behaviors. *Neuron* *107*, 368-382.e8.
482 <https://doi.org/10.1016/j.neuron.2020.04.024>.
- 483 42. Sommer, M.A., and Wurtz, R.H. (2006). Influence of the thalamus on spatial visual processing
484 in frontal cortex. *Nature* *444*, 374–377. <https://doi.org/10.1038/nature05279>.
- 485 43. Shin, A., Park, S., Shin, W., Woo, J., Jeong, M., Kim, J., and Kim, D. (2023). A brainstem-to-
486 mediodorsal thalamic pathway mediates sound-induced arousal from slow-wave sleep. *Current
487 Biology* *33*, 875-885.e5. <https://doi.org/10.1016/j.cub.2023.01.033>.
- 488 44. Wolff, M., and Halassa, M.M. (2024). The mediodorsal thalamus in executive control. *Neuron*
489 *112*, 893–908. <https://doi.org/10.1016/j.neuron.2024.01.002>.
- 490 45. Baek, J., Lee, S., Cho, T., Kim, S.-W., Kim, M., Yoon, Y., Kim, K.K., Byun, J., Kim, S.J.,
491 Jeong, J., et al. (2019). Neural circuits underlying a psychotherapeutic regimen for fear
492 disorders. *Nature* *566*, 339–343. <https://doi.org/10.1038/s41586-019-0931-y>.
- 493 46. Craig, A.D.B. (2009). How do you feel--now? The anterior insula and human awareness. *Nat
494 Rev Neurosci* *10*, 59–70. <https://doi.org/10.1038/nrn2555>.
- 495 47. Underwood, E. (2021). A sense of self. *Science* (1979) *372*, 1142–1145.
496 <https://doi.org/10.1126/science.372.6547.1142>.
- 497 48. Gogolla, N. (2017). The insular cortex. *Current Biology* *27*, R580–R586.
498 <https://doi.org/10.1016/j.cub.2017.05.010>.
- 499 49. Uddin, L.Q. (2015). Salience processing and insular cortical function and dysfunction. *Nat Rev
500 Neurosci* *16*, 55–61. <https://doi.org/10.1038/nrn3857>.
- 501 50. Deng, H., Xiao, X., Yang, T., Ritola, K., Hantman, A., Li, Y., Huang, Z.J., and Li, B. (2021). A
502 genetically defined insula-brainstem circuit selectively controls motivational vigor. *Cell* *184*,
503 6344-6360.e18. <https://doi.org/10.1016/j.cell.2021.11.019>.

- 504 51. Nicolas, C., Ju, A., Wu, Y., Eldirdiri, H., Delcasso, S., Couderc, Y., Fornari, C., Mitra, A.,
505 Supiot, L., Vérité, A., et al. (2023). Linking emotional valence and anxiety in a mouse insula-
506 amygdala circuit. *Nat Commun* 14, 5073. <https://doi.org/10.1038/s41467-023-40517-1>.
- 507 52. Gehrlach, D.A., Dolensek, N., Klein, A.S., Roy Chowdhury, R., Matthys, A., Junghänel, M.,
508 Gaitanos, T.N., Podgornik, A., Black, T.D., Reddy Vaka, N., et al. (2019). Aversive state
509 processing in the posterior insular cortex. *Nat Neurosci* 22, 1424–1437.
510 <https://doi.org/10.1038/s41593-019-0469-1>.
- 511 53. Wang, Q., Zhu, J.-J., Wang, L., Kan, Y.-P., Liu, Y.-M., Wu, Y.-J., Gu, X., Yi, X., Lin, Z.-J.,
512 Wang, Q., et al. (2022). Insular cortical circuits as an executive gateway to decipher threat or
513 extinction memory via distinct subcortical pathways. *Nat Commun* 13, 5540.
514 <https://doi.org/10.1038/s41467-022-33241-9>.
- 515 54. Aspide, R., Gironi Carnevale, U.A., Sergeant, J.A., and Sadile, A.G. (1998). Non-selective
516 attention and nitric oxide in putative animal models of Attention-Deficit Hyperactivity
517 Disorder. *Behavioural Brain Research* 95, 123–133. [https://doi.org/10.1016/S0166-4328\(97\)00217-9](https://doi.org/10.1016/S0166-4328(97)00217-9).
- 519 55. Aspide, R., Fresiello, A., de Filippis, G., Gironi Carnevale, U.A., and Sadile, A.G. (2000).
520 Non-selective attention in a rat model of hyperactivity and attention deficit: subchronic
521 methylphenydate and nitric oxide synthesis inhibitor treatment. *Neurosci Biobehav Rev* 24,
522 59–71. [https://doi.org/10.1016/S0149-7634\(99\)00045-7](https://doi.org/10.1016/S0149-7634(99)00045-7).
- 523 56. Lawson, S.K., Gray, A.C., and Woehrle, N.S. (2016). Effects of oxytocin on serotonin 1B
524 agonist-induced autism-like behavior in mice. *Behavioural Brain Research* 314, 52–64.
525 <https://doi.org/10.1016/j.bbr.2016.07.027>.
- 526 57. DeNardo, L.A., Liu, C.D., Allen, W.E., Adams, E.L., Friedmann, D., Fu, L., Guenthner, C.J.,
527 Tessier-Lavigne, M., and Luo, L. (2019). Temporal evolution of cortical ensembles promoting
528 remote memory retrieval. *Nat Neurosci* 22, 460–469. <https://doi.org/10.1038/s41593-018-0318-7>.
- 530 58. Shang, C., Liu, A., Li, D., Xie, Z., Chen, Z., Huang, M., Li, Y., Wang, Y., Shen, W.L., and
531 Cao, P. (2019). A subcortical excitatory circuit for sensory-triggered predatory hunting in mice.
532 *Nat Neurosci* 22, 909–920. <https://doi.org/10.1038/s41593-019-0405-4>.

- 533 59. Wang, L., Chen, I.Z., and Lin, D. (2015). Collateral Pathways from the Ventromedial
534 Hypothalamus Mediate Defensive Behaviors. *Neuron* *85*, 1344–1358.
535 <https://doi.org/10.1016/j.neuron.2014.12.025>.
- 536 60. Zhang, X., and Li, B. (2018). Population coding of valence in the basolateral amygdala. *Nat*
537 *Commun* *9*, 5195. <https://doi.org/10.1038/s41467-018-07679-9>.
- 538 61. Zingg, B., Chou, X. lin, Zhang, Z. gang, Mesik, L., Liang, F., Tao, H.W., and Zhang, L.I.
539 (2017). AAV-Mediated Anterograde Transsynaptic Tagging: Mapping Corticocollicular Input-
540 Defined Neural Pathways for Defense Behaviors. *Neuron* *93*, 33–47.
541 <https://doi.org/10.1016/j.neuron.2016.11.045>.
- 542 62. Darwin, C. On the Origin of Species . Evolution and Creationism .
- 543 63. Abbey-Lee, R.N., and Dingemanse, N.J. (2019). Adaptive individual variation in phenological
544 responses to perceived predation levels. *Nat Commun* *10*, 1601.
545 <https://doi.org/10.1038/s41467-019-09138-5>.
- 546 64. Costa-Mattioli, M., and Walter, P. (2020). The integrated stress response: From mechanism to
547 disease. *Science* (1979) *368*. <https://doi.org/10.1126/science.aat5314>.
- 548 65. Hoverman, J.T., and Searle, C.L. (2016). Behavioural influences on disease risk: implications
549 for conservation and management. *Anim Behav* *120*, 263–271.
550 <https://doi.org/10.1016/j.anbehav.2016.05.013>.
- 551 66. Marquez-Legorreta, E., Constantin, L., Piber, M., Favre-Bulle, I.A., Taylor, M.A., Blevins,
552 A.S., Giacometto, J., Bassett, D.S., Vanwalleghem, G.C., and Scott, E.K. (2022). Brain-wide
553 visual habituation networks in wild type and fmr1 zebrafish. *Nat Commun* *13*, 895.
554 <https://doi.org/10.1038/s41467-022-28299-4>.
- 555 67. Fotowat, H., and Engert, F. (2023). Neural circuits underlying habituation of visually evoked
556 escape behaviors in larval zebrafish. *eLife* *12*. <https://doi.org/10.7554/eLife.82916>.
- 557 68. Oliva, D., Medan, V., and Tomsic, D. (2007). Escape behavior and neuronal responses to
558 looming stimuli in the crab *Chasmagnathus granulatus* (Decapoda: Grapsidae). *Journal of*
559 *Experimental Biology* *210*, 865–880. <https://doi.org/10.1242/jeb.02707>.
- 560 69. Sprague, J.M. (1966). Interaction of Cortex and Superior Colliculus in Mediation of Visually
561 Guided Behavior in the Cat. *Science* (1979) *153*, 1544–1547.
562 <https://doi.org/10.1126/science.153.3743.1544>.

- 563 70. Zénon, A., and Krauzlis, R.J. (2012). Attention deficits without cortical neuronal deficits.
564 Nature 489, 434–437. <https://doi.org/10.1038/nature11497>.
- 565 71. Hu, F., and Dan, Y. (2022). An inferior-superior colliculus circuit controls auditory cue-
566 directed visual spatial attention. Neuron 110, 109-119.e3.
567 <https://doi.org/10.1016/j.neuron.2021.10.004>.
- 568 72. Itti, L., and Koch, C. (2001). Computational modelling of visual attention. Nat Rev Neurosci 2,
569 194–203. <https://doi.org/10.1038/35058500>.
- 570 73. Beckers, T., Hermans, D., Lange, I., Luyten, L., Schevaneels, S., and Vervliet, B. (2023).
571 Understanding clinical fear and anxiety through the lens of human fear conditioning. Nature
572 Reviews Psychology 2, 233–245. <https://doi.org/10.1038/s44159-023-00156-1>.
- 573 74. Deisseroth, K. (2014). Circuit dynamics of adaptive and maladaptive behaviour. Nature 505,
574 309–317. <https://doi.org/10.1038/nature12982>.
- 575 75. Anderson, D.J., and Adolphs, R. (2014). A Framework for Studying Emotions across Species.
576 Cell 157, 187–200. <https://doi.org/10.1016/j.cell.2014.03.003>.
- 577 76. Kaiser, T., and Feng, G. (2015). Modeling psychiatric disorders for developing effective
578 treatments. Nat Med 21, 979–988. <https://doi.org/10.1038/nm.3935>.
- 579 77. Gururajan, A., Reif, A., Cryan, J.F., and Slattery, D.A. (2019). The future of rodent models in
580 depression research. Nat Rev Neurosci 20, 686–701. <https://doi.org/10.1038/s41583-019-0221->
581 6.
- 582
- 583
- 584
- 585

586 **STAR*METHODS**

587 **METHOD DETAILS**

588 **Animal Preparation**

589 All experimental procedures were approved by the Animal Care and Use Committees
590 at the Shenzhen Institute of Advanced Technology (SIAT), Chinese Academy of
591 Sciences (CAS). Adult (6– 8 week-old) male C57BL/6J (Beijing Vital River Laboratory
592 Animal Technology Co., Ltd., Beijing, China), VGLUT2-ires-Cre (#016963) mice
593 were used in this study. Mice were housed at 22–25 °C on a circadian cycle of 12-hour
594 light and 12-hour dark with ad-libitum access to food and water.

595

596 **Viral vector preparation**

597 For optogenetic experiments, we used plasmids for AAV2/9 viruses encoding
598 *CaMKIIα:: hChR2* (H134R)-mCherry, *CaMKIIα:: mCherry*, *EF1α:: DIO-hChR2*
599 (H134R)-mCherry, *EF1α:: DIO-mCherry*, *EF1α:: DIO-EYFP* (gifts from Dr. Karl
600 Deisseroth, Stanford University) and Retro-AAV-*EF1α-DIO-hChR2* (H134R)-
601 mCherry (packaged by BrainCase Co., Ltd., Shenzhen). Viral vector titers were in the
602 range of 3-6x10¹² genome copies per ml (gc)/mL.

603 For viral tracing, viral vectors RV-dG-dsRed, RV-dG-GFP, Retro-AAV-hSyn-mcherry,
604 Retro-AAV-hSyn-eYFP, AAV1-hSyn-SV40 NLS-Cre were used (packaged by
605 BrainCase Co.). Adeno-associated and rabies viruses were purified and concentrated to
606 titers at approximately 3×10¹² v.g/ml and 1×10⁹ pfu/ml, respectively.

607

608 **Stereotaxic Surgery**

609 Animals were anesthetized with pentobarbital (i.p., 80 mg/kg) before stereotaxic
610 injection. The viruses were injected into the SC (AP –3.80 mm, ML ±0.8 mm, and DV
611 –1.8 mm), the insula (AP +0.14 mm, ML ±3.75 mm, DV range between –3.75 and –3.9
612 mm), and the Cg (AP +0.3 mm, ML ±0.30 mm, DV –1.5 mm). Optical stimulation of
613 terminals was conducted using a 200-μm optic fiber (NA: 0.37; NEWDOON,
614 Hangzhou) unilaterally implanted into the VTA (AP –3.20 mm, ML –0.25 mm, DV

615 –3.8 mm), MD (AP –1.3 mm, ML –0.30 mm, DV –3.2 mm), the SC (AP –3.80 mm,
616 ML ±0.8 mm, DV –1.8 mm), and the BLA (AP –1.5 mm, ML ±3.1 mm, DV –4.70
617 mm). To block backpropagation of virus in SC, cannulas were implanted 0.3 mm above
618 the SC (AP –3.80 mm, ML ±0.8 mm, DV –1.5 mm). Either bupivacaine (4%, 0.3 µl)
619 or saline (control) was delivered into the SC 30 min before optogenetic modulation and
620 behavioral tests. Mice had at least 2 weeks to recover after surgery before testing.
621

622 **Anatomical tracing**

623 To investigate the origin of the SC-MD and SC-VTA or insula-MD and insula-VTA
624 projecting neurons, we injected RV-dG-dsRed into the VTA and RV-dG-EGFP into the
625 MD in the same animal. To demonstrate the different SC and insula outputs, we injected
626 AAV9-EF1 α -mCherry into the SC and AAV9-EF1 α -EYFP into the insula. To map
627 the axonal output of input-defined neurons in the VTA and MD, anterograde *trans-*
628 synaptic AAV1-hSyn-SV40 NLS-Cre was unilaterally injected into the SC, EF1 α ::
629 DIO-mCherry was injected into the VTA and EF1 α :: DIO-EYFP was injected into MD.
630

631 **Histology**

632 Mice were given an overdose of pentobarbital and perfused with 0.9% saline followed
633 by 4% paraformaldehyde (PFA) in PBS. Brains were dissected and postfixed in 4%
634 PFA at 4 °C for 24 h then transferred to 30% sucrose for 2 d. Coronal slices (40 µm)
635 were taken across the entire rostrocaudal extent of the brain using a cryostat at –15 °C
636 and stored in 24-well plates containing cryoprotectant at 4 °C. To visualize virus
637 expression, optic fiber tips, optrode placements, and viral tracing targets, floating
638 sections were blocked with 10% normal goat serum in PBS-T (0.03% Triton-X 100),
639 and DAPI (1:50000, Cat#62248, ThermoFisher). Brain sections were mounted and
640 cover-slipped with Fluoromount aqueous mounting medium (Sigma-Aldrich, USA).
641 Sections were then photographed using an Olympus VS120 virtual microscopy slide
642 scanning system or a Zeiss LSM LSM 880 confocal microscope. Images were analyzed
643 with ImageJ, Image Pro-plus, and Photoshop software.
644

645 **c-Fos Immunolabeling**

646 To visualize c-Fos activity across the whole brain following optogenetic activation of
647 specific neural circuits, we used different optogenetic stimulus groups:
648 *CaMKIIa::ChR2*_{Insula-BLA}, *CaMKIIa::mcherry*_{Insula-BLA} (control), and
649 *CaMKIIa::ChR2*_{Insula-MD} *CaMKIIa::mcherry*_{Insula-MD} (control). Mice in each group were
650 given 3 min habituation time and 2 presentations of optogenetic stimuli (20 Hz, 5 ms,
651 2.5 s, with an interval no less than 2 min) in a looming box during a 10–20 min session.
652 Mice were sacrificed 1.5 hours following optogenetic activation and brains then stained
653 for both c-Fos and DAPI. Sections were washed and incubated in primary (1:500,
654 Cat#2250, CST) and secondary (1:300, Cat#111-547-003, Jackson immuno research)
655 antibodies and DAPI (1:50000, Cat#62248, ThermoFisher). Imagines were taken using
656 an Olympus VS120 virtual microscopy slide scanning system or a Zeiss LSM LSM 880
657 confocal microscope and then overlaid with The Mouse Brain in Stereotaxic
658 Coordinates to locate brain nuclei. Then, c-Fos positive neurons were manually counted
659 by an individual experimenter blind to the experiment groups using ImageJ and
660 Photoshop software.

661

662 **Looming test**

663 The looming test was performed in a closed Plexiglas box (40 x 40 x 30 cm) with a
664 shelter nest in one corner. An LCD monitor was placed on the ceiling to present
665 looming stimulus to the upper visual field. The stimulus was a black disc on a grey
666 background expanding from a 2° to 20° visual angle, repeated 15 times, lasting a total
667 of 5.5 seconds. Mouse behavior was recorded using a Sony FDR-AX45 camera. Mice
668 were handled and habituated for 10 min to the looming box one day prior to the test.
669 On the test day, mice were given 3 min to habituate to the box, then 10 looming stimulus
670 trials were presented. The stimulus was triggered by the experimenter when the mouse
671 was far from the shelter and the interval between each trial no less than 2 min. For
672 optogenetic activation experiments with looming stimulus, mice received blue light (10
673 Hz, 473 nm; Aurora-220-473, NEWDOON, Hangzhou) at an intensity of 8 mW at the

674 fiber tips. Light stimulation was delivered 1 s before onset of the looming stimulus and
675 continued until the stimulus ended.

676

677 **Pupillometry**

678 Mice were head-fixed and allowed to run freely on a stationary foam ball with a
679 diameter of 20 cm during testing. Mice were first habituated to the ball for 3 consecutive
680 days before recording began (day 1, 15 min; day 2, 30 min; day 3, 1 hour). One eye of
681 each mouse was illuminated with a 940 nm near-infrared light and the pupillary
682 responses were recorded using a camera (Point Grey, FL3-U3-13E4M, set to 200 fps).
683 Software (LabVIEW) was used to control the camera and process images in real time
684 to obtain pupil data, including x position, y position, diameter of the pupil and the
685 timestamp for each image. To avoid interference between pupil positions and pupil
686 diameter accuracy, the ellipse long diameter was measured instead of the cross diameter
687 and area.

688 Looming stimuli were presented using Matlab Psychtoolbox and displayed on a 19-
689 inch screen (DELL, P1917S) during pupillometry recording. An area of 60 x 60 pixels
690 in one corner of the screen light up during the test as a way of modulating brightness.
691 Brightness changes were detected using a photodiode and these signals were
692 transmitted to LabVIEW using the same circuit board and used to timestamp the stimuli
693 time with the pupillary data.

694

695 **Optogenetic manipulation**

696 A closed Plexiglas box (40 x 40 x 30 cm) with a shelter/nest in the corner was used for
697 optogenetic stimulation experiments. Animals were handled and habituated to the
698 looming box for 10 min one day prior to testing. During the looming test session, mice
699 were allowed to freely explore the looming box for 3–5 min and then received either
700 optogenetic manipulation or presentation of the looming stimuli. For optogenetic
701 stimulation experiments, the implanted optic fibers were connected to a 473-nm blue
702 light laser (Aurora-220-473, NEWDOON, Hangzhou) at approximately 15-20 mW for
703 terminals stimulation. Optogenetic activation of neural circuits began 4–5 weeks after

704 animals received stereotactic viral injections and fiber implants. During experiments,
705 light was delivered to either insula-BLA terminals, SC–VTA terminals, insula-VTA
706 terminals, SC–MD terminals or insula-MD terminals. The light was delivered into the
707 targeted regions simultaneously 1 s before onset of the looming stimulus and continued
708 until 1 s after the end of the looming stimulus. Mice received 7.5 s blue light stimulation
709 (150 laser pulses of 5 ms at 20 Hz) at axon terminals during pathway activation
710 experiments. Three repeated light stimuli trials were delivered at about 3 min intervals
711 via a manual trigger in the targeting regions and all light stimulation was manually
712 presented by the experimenter. For all gain-of function experiments (optogenetic
713 activation of ChR2), the activation was all unilateral.

714

715 **Behavioral analysis**

716 Behavioral data were analyzed using Adobe Premiere software and observers were
717 blind to experimental conditions. Mice were allowed to move freely in the open field
718 with a shelter/nest before looming stimulus or light stimulation. Individual time courses
719 were represented setting T=0 ms as the time of stimulation. Three parameters extracted
720 from the behavioral experiments were used to quantify the looming-evoked or light-
721 evoked defensive behavior: (1) rearing frequency: frequency of rearing on hindlimbs
722 and leaning against the walls with one or both forepaws were visually monitored in 1-
723 min blocks. (2) response latency: time between the onset of the looming stimulus or
724 photostimulation and the onset of the escape, escape was defined as the motion that
725 resulted in shelter entrance within stimulation period. (2) return time: the time from
726 looming stimulus or photostimulation presentation to time when the mouse entered the
727 nest. (3) Duration in nest: time spent in the nest following looming stimulus or
728 photostimulation. Data obtained from mice with imprecise fiber placements were not
729 used for analyses.

730

731 **In vivo extracellular recording**

732 Mice were habituated to the head-fixed position ~~to a magnet~~ whilst on a foam ball 1 hr
733 each day for 3 days. Then, using a 16-channel micro-electrode (Neuronexus, A4x4-

734 6mm-100-125-177-A16) and a multi-channel recording system (OmniPlex D, Plexon,
735 Dallas, USA), the target brain regions were recorded. Electrodes were connected to a
736 headstage (Plexon, Dallas, USA) containing 16-32 unity-gain operational amplifiers.
737 The headstage was connected to a 16-channel computer-controlled preamplifier (gain
738 X-100, band-pass filter from 150 Hz to 40 kHz, Plexon). Neuronal activity was
739 digitized at 40 kHz and band-pass filtered from 300 Hz to 8 kHz, and isolated by time-
740 amplitude window discrimination and template matching using a Multichannel
741 Acquisition Processor system (Plexon). To investigate optogenetic effects, we inserted
742 an optic fiber (200 μ m diameter; 0.22 NA) 50 μ m above the stimulated brain region.
743 Before optical stimulation, we recorded for approximately 3 min to establish a stable
744 electrode position inside the brain tissue. When the signal in the BLA was stable, optical
745 stimulation was delivered at 1 min intervals. At least 10 repetitions of light stimulation
746 was recorded during each session. At the conclusion of the experiment, recording sites
747 were marked with DiI cell labeling solution (Invitrogen, USA) before perfusion, and
748 electrode locations were reconstructed using standard histological techniques.

749

750 **Spike sorting**

751 Single-unit spike sorting was performed using Plexon Offline Sorter software (Plexon,
752 Inc., Dallas, TX, USA), then analyzed in Neuroexplorer (Nex Technologies, Madison,
753 AL, USA) and Matlab (MathWorks, Natick, MA, USA). Principal-component scores
754 were calculated for unsorted waveforms and plotted in a three-dimensional principal-
755 component space; clusters containing similar valid waveforms were manually defined.
756 A group of waveforms was considered to be generated from a single neuron if it defined
757 a discrete cluster in principal component space that was distinct from clusters for other
758 units and if it displayed a clear refractory period (>1 ms) in the auto-correlogram
759 histograms. To avoid analysis of the same neuron recorded on different channels, we
760 computed cross-correlation histograms. If a target neuron presented a peak of activity
761 at a time that the reference neuron fired, only one of the two neurons was considered
762 for further analysis.

763 To determine whether the firing rate of a particular BLA neuron was altered in response
764 to optogenetic activation of the insula (or SC-VTA,SC-MD, insula, insula-MD) axon
765 terminals, we used peristimulus time histograms (PSTHs) to analyze firing pattern
766 (Buzsaki et al., 2004). We calculated PSTHs using a 7.5 second period before and after
767 onset of optogenetic stimulus with a bin size of 100 ms. We calculated the basal
768 spontaneous firing rate of each neuron by averaging the PSTH over the pre-stimulus
769 bins. Peak optogenetically-evoked firing rate was then calculated as the maximum
770 value of the PSTH after stimulus onset (within 2.5 seconds from the stimulus). The
771 baseline mean was the average of the PSTH bins before stimulus onset, and the SD was
772 the standard deviation of the PSTH bins before stimulus onset. We calculated a Z-score
773 firing rate using the following equation: $Z = (FR - \text{mean of } FR_b)/SD \text{ of } FR_b$, where FR
774 indicates the firing rate for each bin and FR_b indicates the baseline firing rate before
775 the stimulus onset. A positive responding neuron was defined when the absolute value
776 of the Z-score firing rate of least one time bin after stimulation was larger than 2.
777 Negative responding neurons were defined when the absolute value of the Z-score
778 firing rate of least one time bin after stimulation was smaller than -2.

779

780 **Power spectrum analysis**

781 The LFP data before and after optogenetic stimulation was conducted with power
782 spectrum analysis, which is a technique for decomposing complex signals into simpler
783 signals based on Fourier transform. The power spectral density (PSD) for LFP data was
784 computed using the multi-taper method (TW = 3, K = 5 tapers) using the Chronux
785 toolbox using custom-written or existing functions in MATLAB (The Math Works).

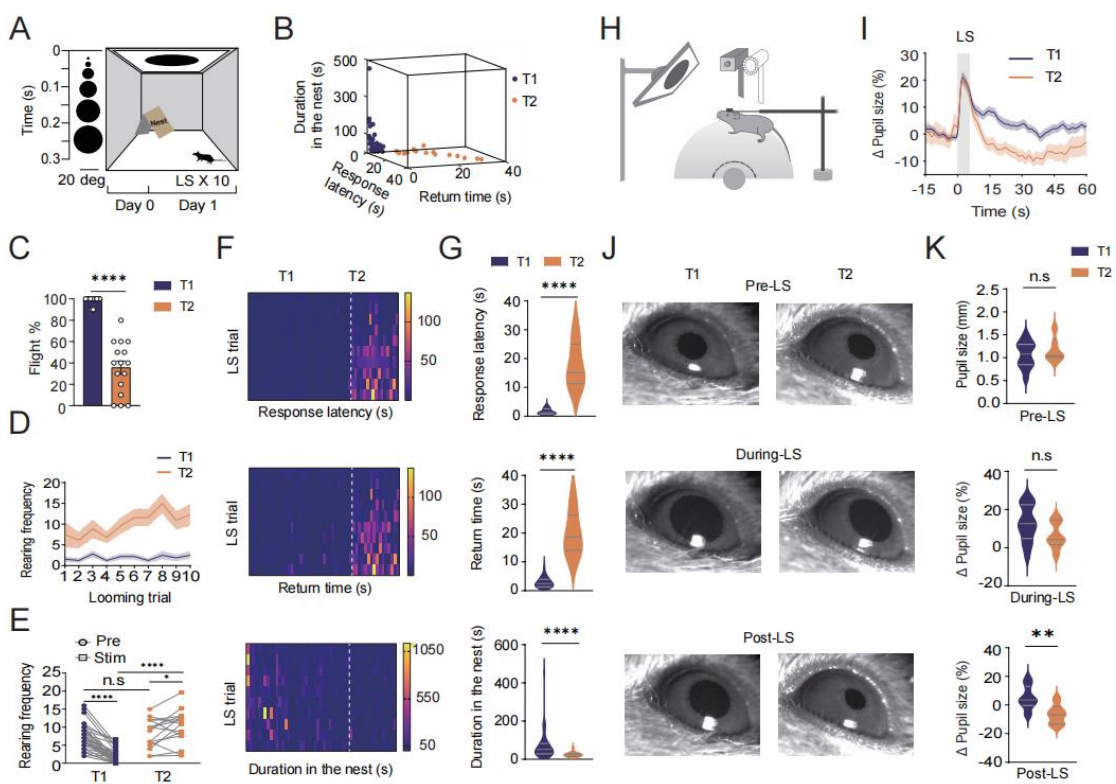
786

787 **Statistical analysis**

788 The number of biological replicates in each group was 3–6 mice per group for anatomy,
789 7–9 mice for optogenetic manipulation and looming stimulation, and 16–51 mice per
790 group for behavioral habituation to looming stimulus. Data distribution was assumed
791 to be normal, but this was not formally tested. All statistics were performed using Graph
792 Pad Prism (GraphPad Software, Inc.) and MATLAB. Paired student T-test, unpaired

793 student T-test, one-way ANOVA and two-way ANOVA were used where appropriate.
794 Bonferroni post-hoc comparisons were conducted to detect significant main effects or
795 interactions. In all statistical measures, a P value <0.05 was considered statistically
796 significant. Post-hoc significance values were set at *P< 0.05, **P< 0.01, ***P< 0.001
797 and ****P< 0.0001, and all statistical tests used are indicated in the figure legends.
798

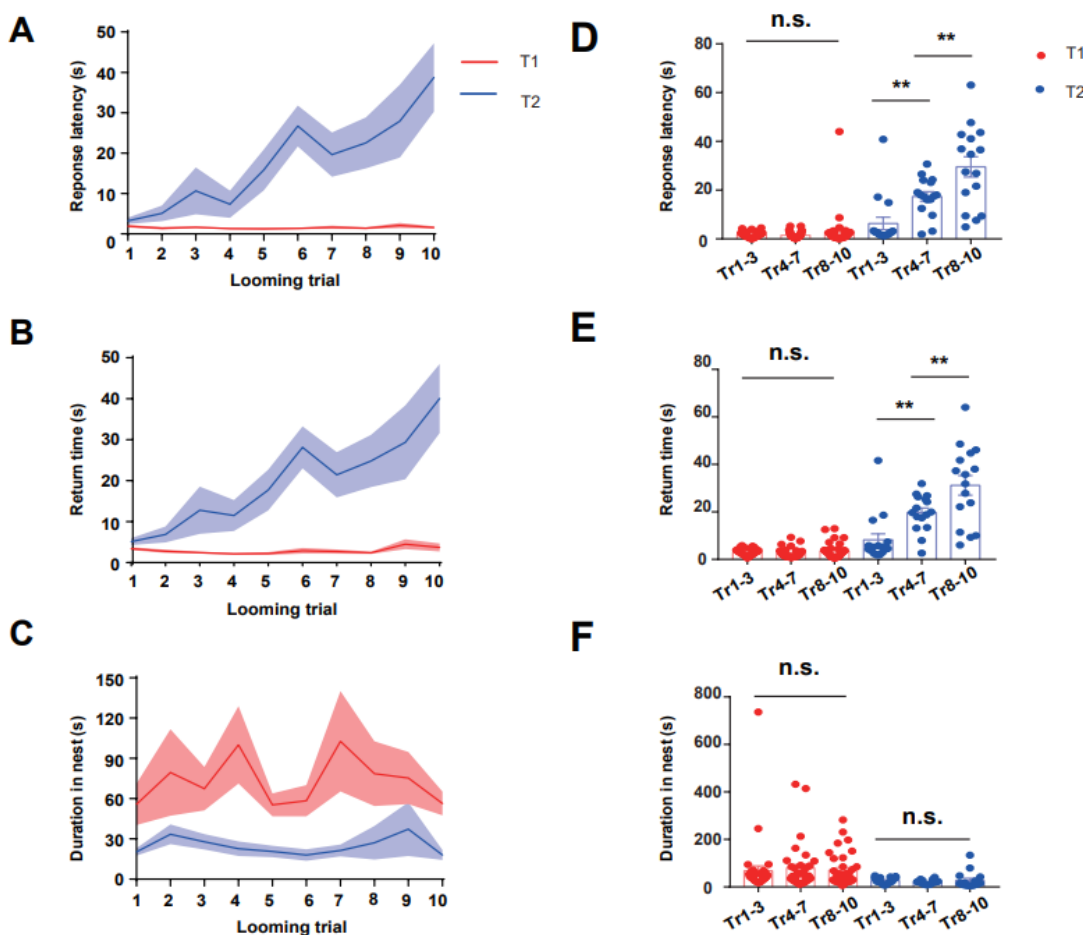
799 **Figures and figure legends**



801 **Figure 1. Individual Variability in Escape Habituation to Repeated Looming
802 Stimuli**

- 803 (A) Schematic paradigm and timeline of 10 blocks of LS. A dark disk expanding from 2 to 20° in 5.5 s. Each ISIs
804 was random within a 2-min period.
- 805 (B) 3D scatter plot of escape behavior parameters (response latency, time to return to nest and duration in nest) of
806 51 male mice categorized as one of two subgroups. T1, Type1, “low habituation” group, T2, Type 2, “high
807 habituation” group.
- 808 (C) The average proportion of trials in which escape occurred in T1 and T2 mice.
- 809 (D) Comparison of rearing frequency in each trial in T1 and T2 mice.
- 810 (E) Comparison of rearing frequency pre-LS (1 min before first LS) and during-LS in T1 and T2 mice. (Two-tailed
811 unpaired t test, $p=0.3750$, $****P<0.0001$).
- 812 (F) Heatmap showing escape behavior parameters in each trial of the 51 mice.
- 813 (G) Bar graph showing the average 1) response latency (Two-tailed unpaired t test, $****p<0.0001$), 2) return time
814 (Two-tailed unpaired t test, $****p<0.0001$) and 3) duration in nest (Two-tailed unpaired t test, $***p=0.0002$)
815 of T1 and T2 mice responding to 10 blocks of LS.
- 816 (H) Schematic of pupillometry recording paradigm with LS in head-fixed awake behaving mice on a ball treadmill.

- 817 **(I)** Graph showing the percentage of pupil-size change 15 s before LS and 60 s after LS in T1 and T2 mice.
- 818 **(J)** Representative image showing pupil diameter 5 s before LS, 5.5 s during LS and 10s after LS.
- 819 **(K)** Pupil size 5 s before LS, 5.5 s during LS and 10 s after LS.



820

821 **Supplementary Figure 1. Behavioral Characteristics of T1 and T2 Groups**

- 822 (A) Graph showing the average response latency in T1 and T2 mice.
823 (B) Graph showing the average return time in T1 and T2 mice.
824 (C) Graph showing the average time spent in nest in T1 and T2 mice.
825 (D) Bar graph showing the average response latency in trials 1–3, trials 4–7 and trials 8–10 (one-way ANOVA,
826 p>0.05, Two-tailed paired t test, **p=0.0013, Two-tailed paired t test, **p=0.0074).
827 (E) Bar graph showing the average return time in trials 1–3, 4–7 and 8–10 (one-way ANOVA, p>0.05, two-tailed
828 unpaired t test, **p=0.0011, two-tailed unpaired t test, **p=0.01).
829 (F) Bar graph showing the average duration in the nest during trials 1–3, 4–7 and 8–10 (one-way ANOVA, p>0.05,
830 two-tailed unpaired t test, p>0.05, two-tailed unpaired t test, p>0.05) of T1 and T2 mice responding to 10 blocks
831 of LS.

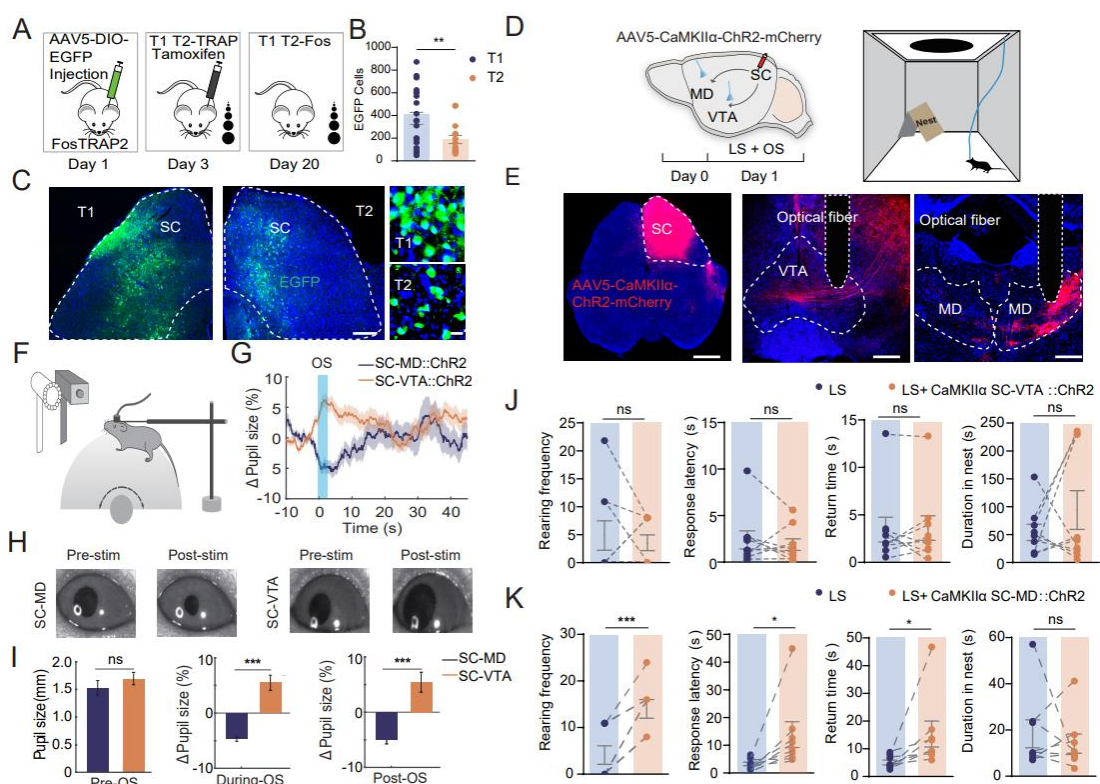
832

833

834

835

836



837

838 **Figure 2 Divergent Superior Colliculus Pathways Modulate Arousal and Escape 839 Behavior**

840 (A) Schematic showing the FosTrap2 procedure.

841 (B) The number of EGFP+ neurons in the SC in T1 and T2 mice (Two-tailed unpaired t test, **p=0.0032, n=22
842 slices from 4 mice in T1, n=15 slices from 4 mice in T2).

843 (C) Looming-associated EGFP+ neuronal activity expressed in the SC in T1 and T2 mice.

844 (D) Schematics showing the OS (optogenetic stimuli) paradigm (*left*) and the experimental procedure with LS
845 (looming stimuli, *right*).

846 (E) Injection of AAV5-CaMKIIα-ChR2-mcherry in the IDSC and fiber implantation in the VTA and MD. Optical
847 fiber positions are outlined using white dotted lines. Blue, DAPI, scale bar=20μm.

848 (F) Schematic paradigm of pupillometry recordings with OS in head-fixed awake behaving mice on a ball treadmill.
849 (G) Graph showing the percentage of change in pupil size 10 s before OS and 45 s after OS of the VTA and the
850 MD.

851 (H) Representative example of pupil diameter 5 s before OS, and 10 s after OS.

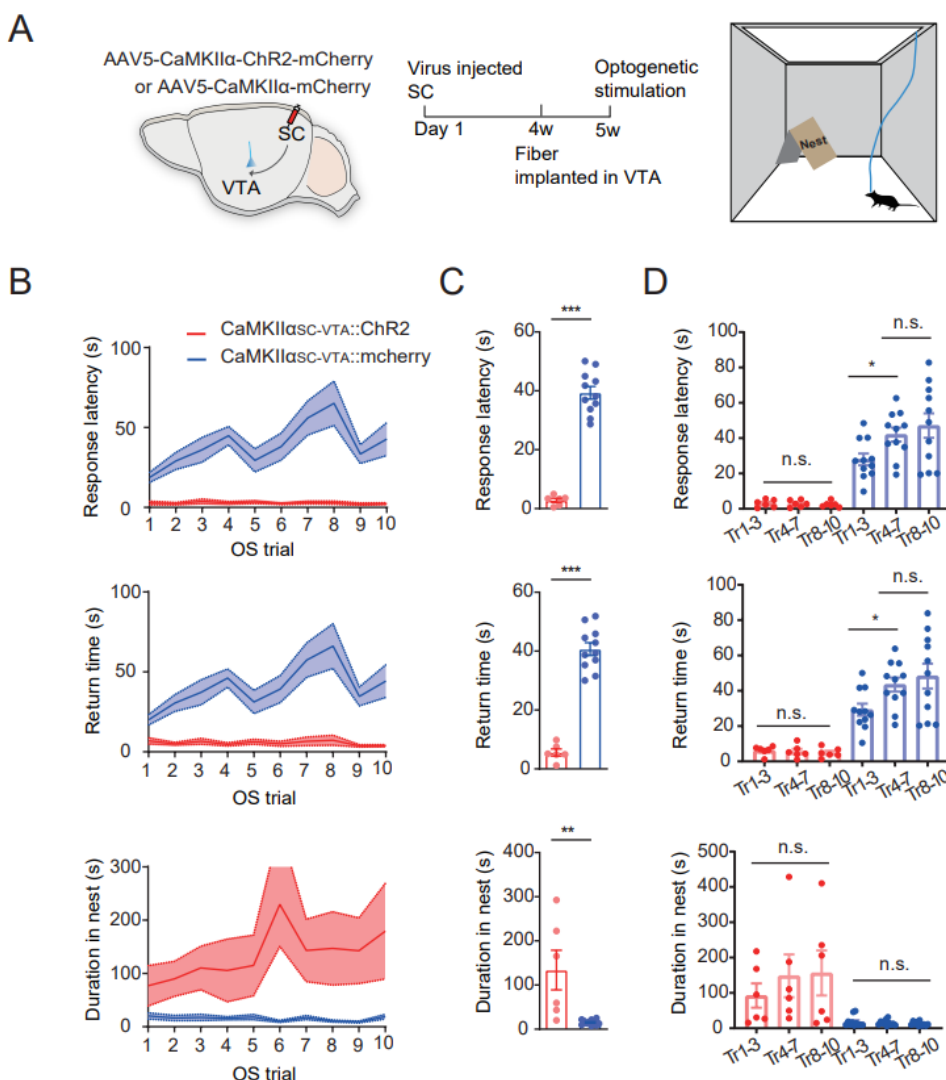
852 **(I)** Bar graph showing the change in pupil size 10 s before OS (two sample t test, p=0.35), 2.5 s during OS (two
853 sample t test, p<0.001) and 2.5 s after OS (two sample t test, p<0.001).

854 **(J)** Measurements were taken during OS (10 trials/mouse) and LS of CaMKII α _{SC-VTA:: ChR2} mice. Bar graphs
855 showing 1) rearing frequency (two-tailed paired t test, p>0.05), 2) response latency (two-tailed paired t test,
856 p>0.05), 3) return time (two-tailed paired t test, p>0.05) , and 4) duration in nest (two-tailed paired t test, p>0.05).

857 **(K)** Measurements were taken during OS (10 trials/mouse) and LS of CaMKII α _{SC-MD:: ChR2} mice. Bar graphs
858 showing 1) rearing frequency (two-tailed paired t test, ***p=0.0004), 2) response latency (two-tailed paired t
859 test, *p=0.042), 3) return time (two-tailed paired t test, *p=0.0497), and 4) duration in nest (two-tailed paired t
860 test, p>0.05) .

861

862



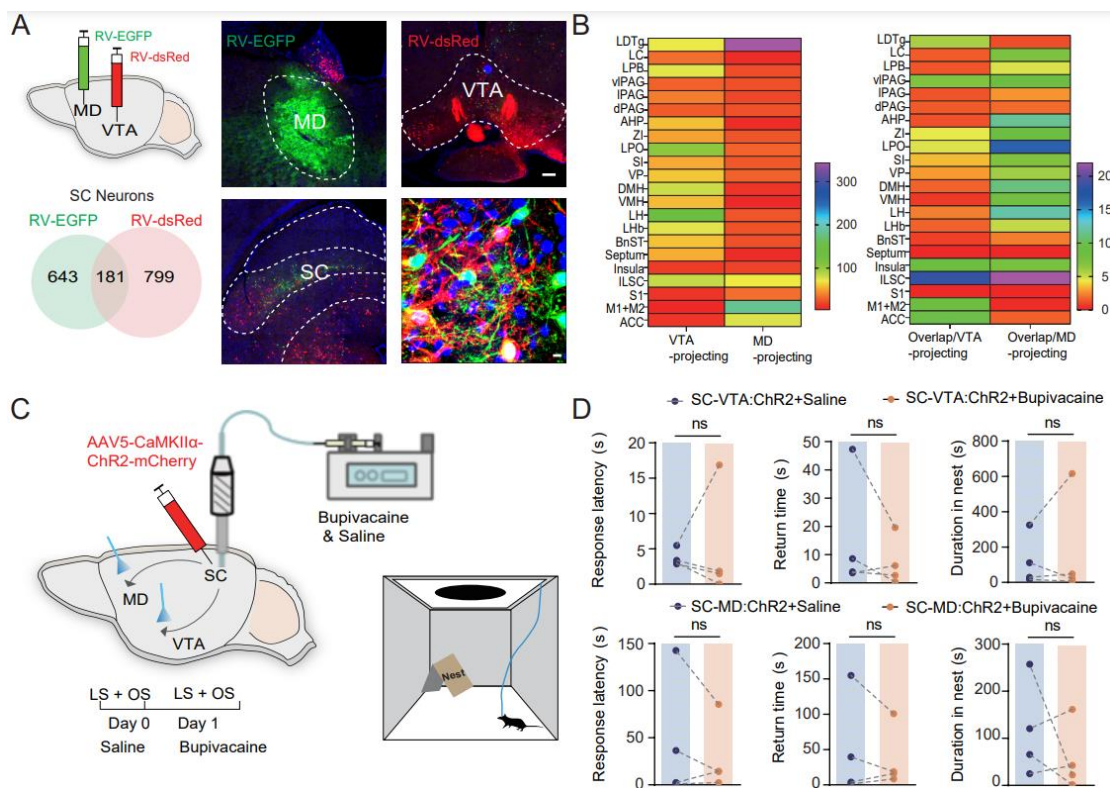
863

864 **Supplementary Figure 2 Selective repeated activation SC-VTA mimicked T1-type**
865 **behaviors**

- 866 (A) Schematic showing the injection of AAV-CaMKII α -ChR2-mcherry into the IDSC and the experimental
867 timeline and optogenetic stimulation (OS) paradigm.
- 868 (B) Time course analysis of 1) response latency, 2) return time and 3) duration in nest following optogenetic
869 stimulation of both the CaMKII α SC-VTA:: ChR2 and mcherry control groups.
- 870 (C) Measurements were taken during OS (10 trials/mouse) of the CaMKII α SC-VTA:: ChR2 and mcherry groups. Bar
871 graph showing the average 1) response latency (Two-tailed t test, **** p <0.0001), 2) return time (two-tailed t
872 test, **** p<0.0001) and 3) duration in nest (two-tailed t test, **p=0.0023).
- 873 (D) Measurements were taken during OS (10 trials/mouse) of the CaMKII α SC-VTA:: ChR2 and mcherry groups.
874 Bar graphs showing average values in trials 1–3, 4–7, and 8–10 for 1) response latency (one-way ANOVA,

875 p=0.6764, *p=0.0296), 2) return time (one-way ANOVA, p=0.3136,*p=0.0325) and 3) duration in nest (one-
876 way ANOVA, p=0.4208,p=0.4858).

877



878

879 **Supplementary Figure 3 SC Pathway Parallel Processing Modulates Variability 880 in Innate Escape Responses**

881 **(A)** Schematic showing injections of RV-dsRed and RV-EGFP into VTA, the MD and the number of SC neurons
882 labeled by each, and number that overlapped.

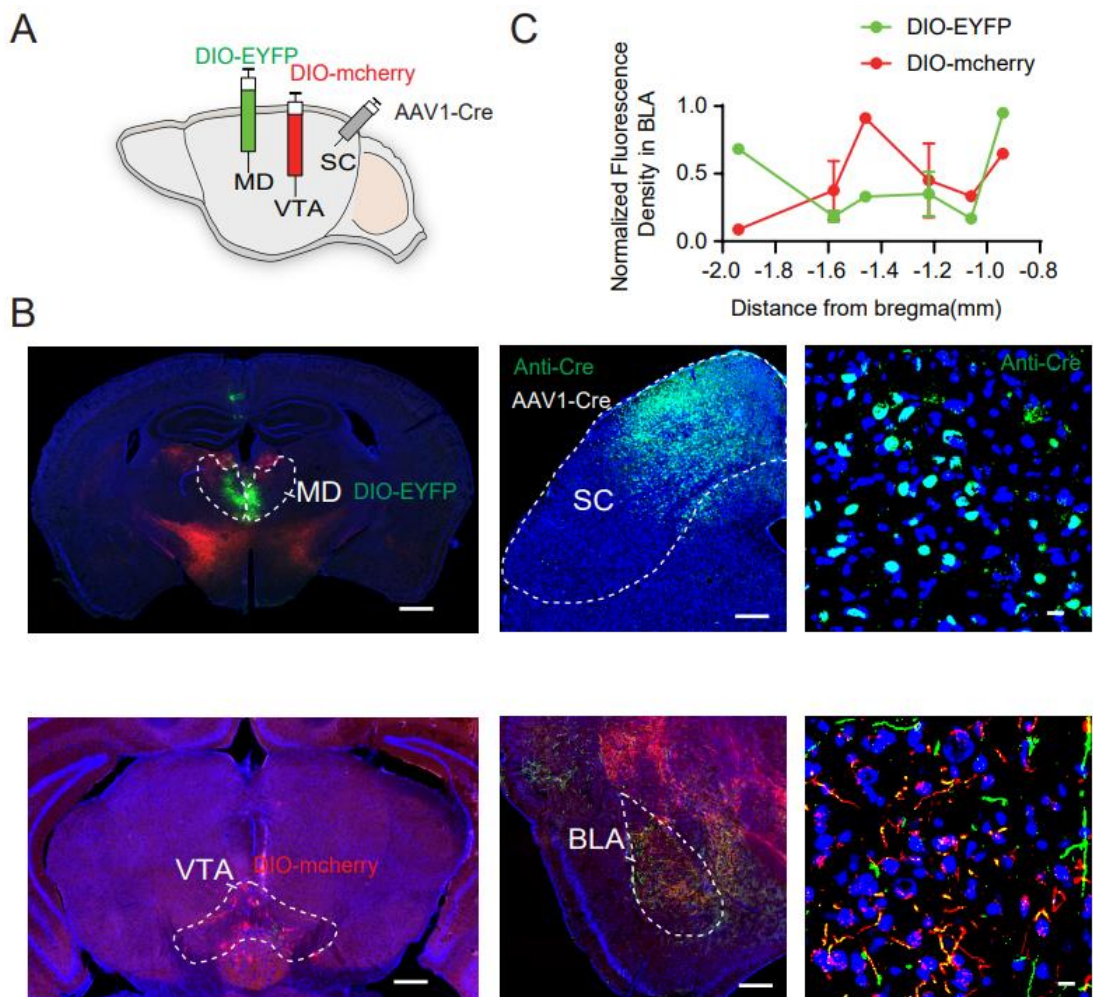
883 **(B)** Heatmap showing quantification of the number of RV-dsRed-and RV-EGFP-labeled neurons, and the amount
884 of overlap, across the whole brain.

885 **(C)** Schematic showing the blocking of neuronal backpropagation in the SC and the experimental timeline.

886 **(D)** Bupivacaine injection (0.3 μ l 4%) in the SC had no effect on stimulation of the SC-VTA and SC-MD.
887 Measurements were taken during OS (10 trials/mouse) and LS of the CaMKII α SC-VTA:: ChR2 and the
888 CaMKII α SC-MD:: ChR2 groups given either saline or bupivacaine. Average values in trials 1–3, 4–7, and 8–10
889 were calculated. *Top* Bar graphs for the CaMKII α SC-VTA:: ChR2 group showing 1) response latency (two-tailed t test, $p>0.05$), 2) return time (two-tailed t test, $p>0.05$) and 3) duration in nest (two-tailed t test, $p>0.05$).
890 *Bottom* Bar graphs for the CaMKII α SC-MD:: ChR2 group showing 1) response latency (two-tailed t test, $p>0.05$),
891 2) return time (two-tailed t test, $p>0.05$) and 3) duration in nest (two-tailed t test, $p>0.05$).

892

893



894

895 **Figure 3 VTA-projecting and MD-projecting SC neurons target the BLA**

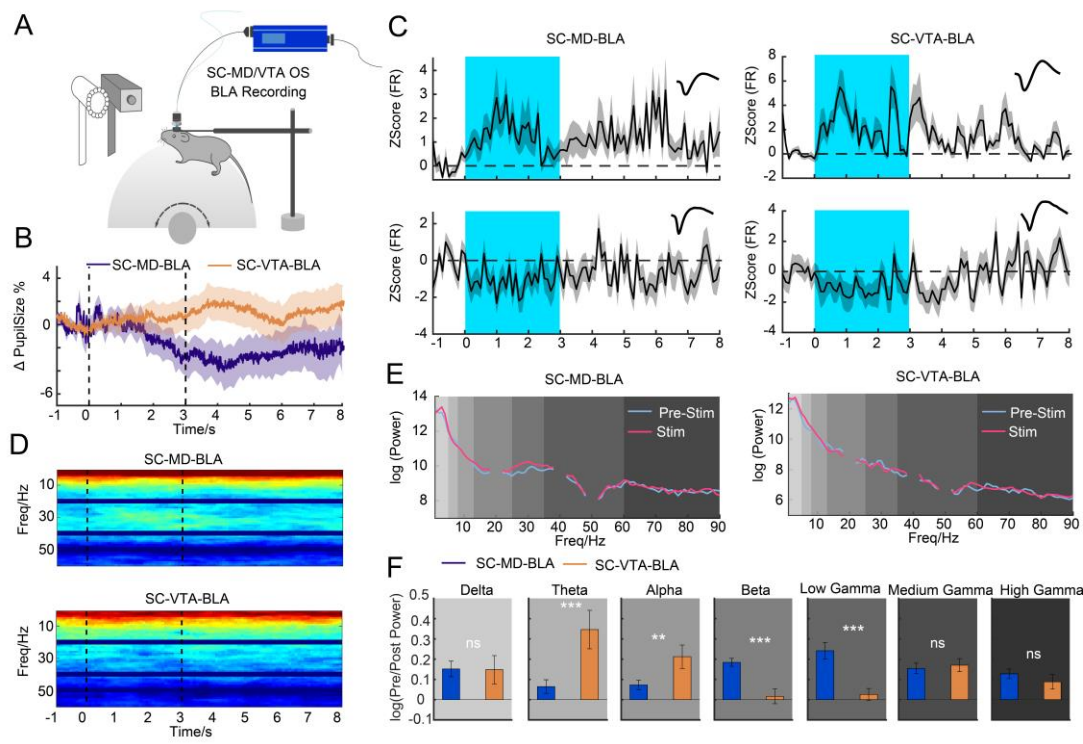
896 (A) Schematic showing injections of AAV1-Cre into the SC and AAV5-DIO-mcherry and AAV5-DIO-EYFP into
897 the VTA and the MD.

898 (B) Representative images showing AAV1-Cre virus injection and Cre immunopositive expression in the SC,
899 AAV5-DIO-EYFP in the MD, AAV5-DIO-mcherry in the VTA and fiber terminals in the BLA. Scale bar=
900 250 μ m (left), 100 μ m (middle), 10 μ m (right).

901 (C) Normalized fluorescence density of fibers labeled with mcherry and eYFP in the BLA.

902

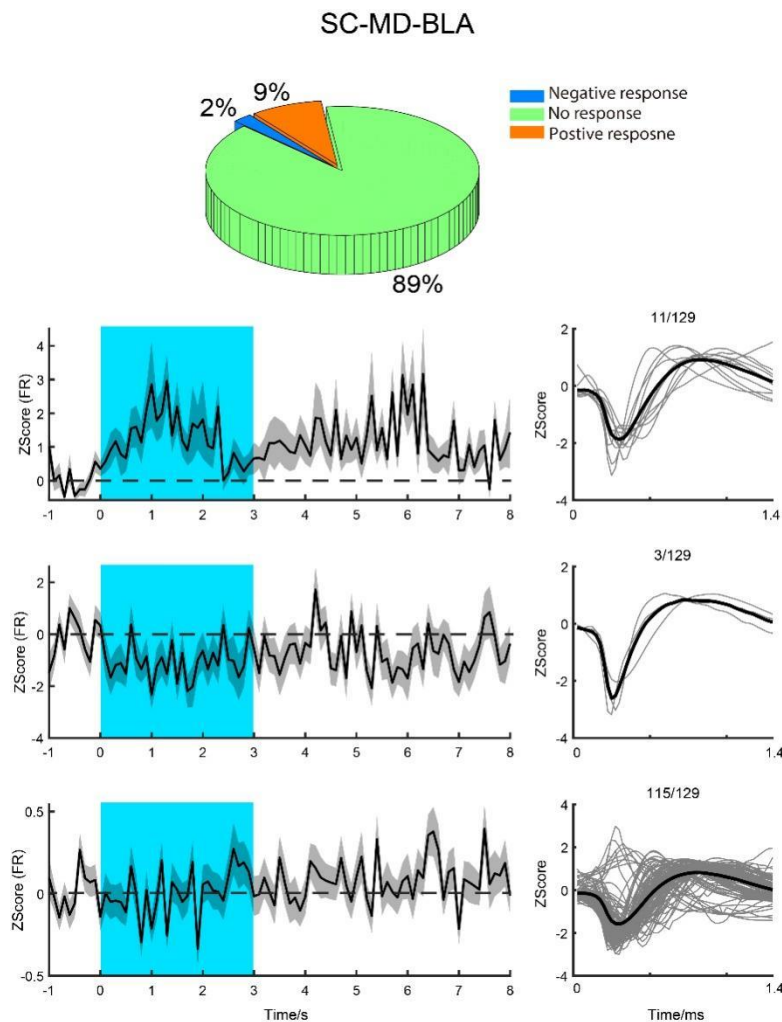
903



905 **Figure 4 SC Pathways Modulate Connectivity and Oscillations in the BLA**

906 (A) Schematic showing electrophysiological recording of VTA-projecting and MD-projecting SC neurons target
907 BLA, and an eye tracker to monitor the pupil size.
908 (B) Graph showing normalized pupil size during optogenetic stimulation (inside the two black dashed lines)
909 comparing VTA-projecting SC neurons (yellow) and MD-projecting SC neurons (blue).
910 (C) Graph showing the normalized firing rate (z-scores) of the neurons recorded in the BLA during optogenetic
911 stimulation. Examples show two types of neuron (excitation and inhibition; spike waveforms are shown above) that
912 were modulated by optogenetic stimulation (blue region, optogenetic stimulation).
913 (D) LFP spectrograms recorded in the BLA during optogenetic stimulation (inside the two black lines). *Top* example
914 from VTA-projecting SC neurons; *Bottom* example from MD-projecting SC neurons.
915 (E) Power spectrums in BLA comparing before (light blue line) and during (pink line) optogenetic stimulation for
916 VTA-projecting and MD-projecting SC neurons .
917 (F) Bar graph showing the comparison between LFP power in different frequency bands before, during and after
918 optogenetic stimulation (two sample t test, delta, p=0.95; theta, p<0.001; alpha, p=0.0029; beta, p<0.001; low gamma,
919 p<0.001; medium gamma, p=0.66; high gamma, p=0.30).

920



921

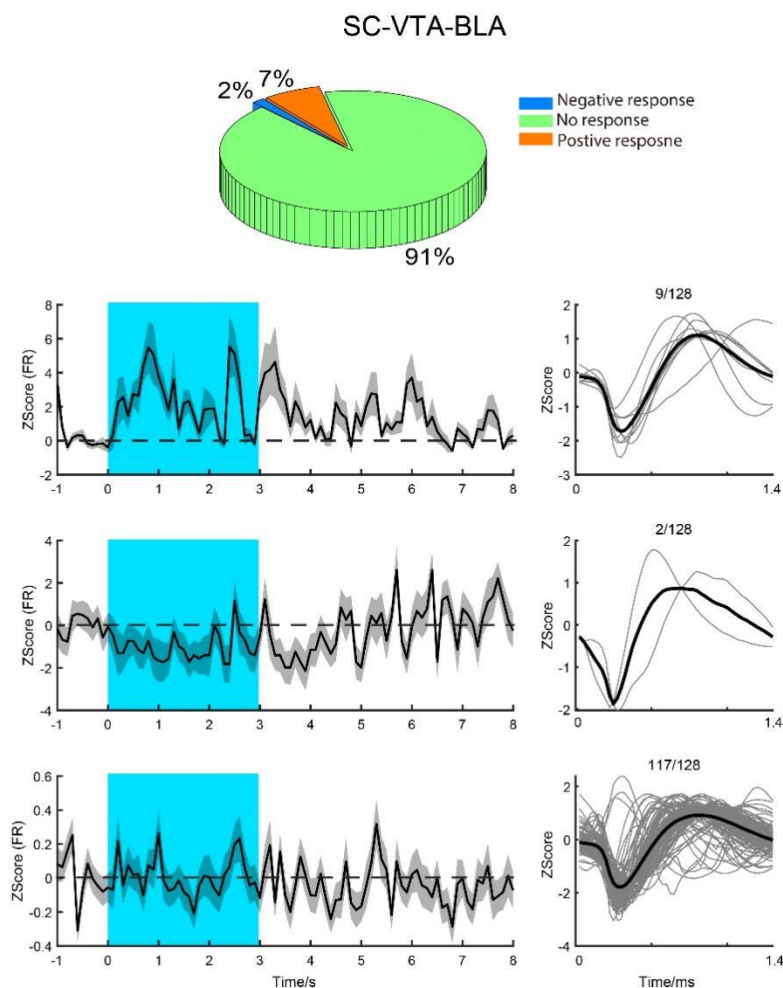
922 **Supplementary Figure 4 BLA neuronal responses to activation of the SC-MD
923 pathway**

924 Pie graph showing the proportion of neurons recorded in BLA with a positive (orange), negative (blue) and no
925 response (green) to optical stimulation of the SC-MD pathway. Line graphs showing the firing rates (z-scores) of
926 three neuronal types before, during and after optogenetic stimulation (blue shadow) alongside the corresponding
927 spike waveforms (*right*).

928

929

930



931

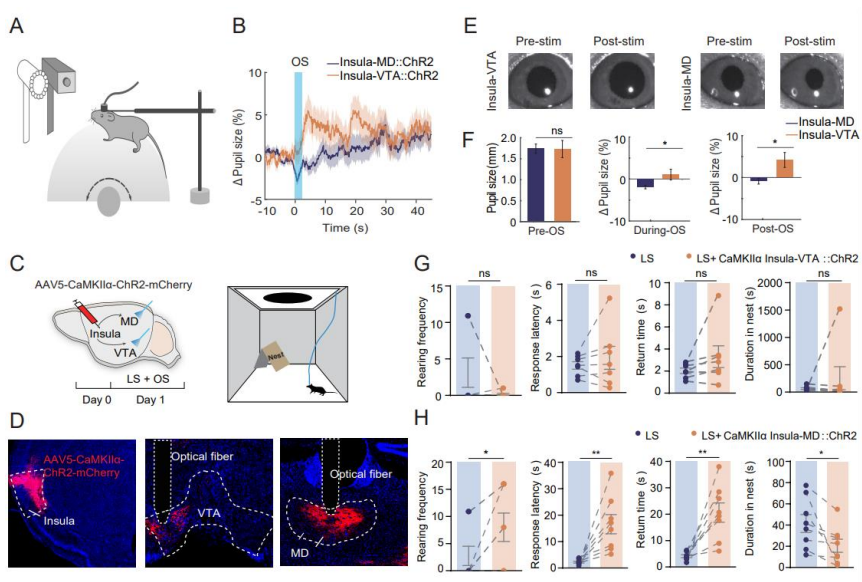
932 **Supplementary Figure 5 BLA neuronal responses to activation of the SC-VTA
933 pathway**

934 Pie graph showing the proportion of neurons recorded in the BLA with positive (orange), negative (blue) and no
935 response (green) to optogenetic stimulation of the SC-VTA pathway. Line graphs showing the firing rates (z-scores) of
936 three neuronal types before, during and after optogenetic stimulation (blue shadow) alongside the corresponding
937 spike waveforms (*right*).

938

939

940



941
942 **Figure 5 Divergent Insula Cortex Pathways modulate arousal and innate escape**
943 **behavior**

944 (A) Schematic showing the pupillometry recording paradigm.
945 (B) Graph shows the percentage of pupil size change at 10 s before OS (blue shaded bar), 2.5 s during OS and 45 s
946 after OS.
947 (C) Schematic showing the OS paradigm and the LS set-up.
948 (D) Schematic showing injection of AAV-CaMKII α -ChR2-mcherry into the insula cortex and fiber implantation in
949 the VTA and the MD. Blue, DAPI, scale bar=20 μ m.
950 (E) Representative example of pupil diameter size 5 s before and 10 s after OS of either the insula-MD or the insula-
951 VTA pathway.
952 (F) Bar graph showing pupil size change 10 s before OS (Two sample t test, p=0.97), 2.5 s during OS (Two sample
953 t test, p=0.0106) and 2.5 s after OS (Two sample t test, p=0.0025).
954 (G) Measurements were taken during OS (10 trials/mouse) and LS of CaMKII $\alpha_{\text{insula-VTA}}\text{: ChR2}$ mice. Bar graphs
955 showing 1) rearing frequency (two-tailed paired t test, p>0.05), 2) response latency (two-tailed paired t test,
956 p>0.05), 3) return time (two-tailed paired t test, p>0.05), and 4) duration in nest (two-tailed paired t test, p>0.05).
957 Measurements were taken during OS (10 trials/mouse) and LS of CaMKII $\alpha_{\text{insula-MD}}\text{: ChR2}$ mice. Bar graph
958 showing 1) rearing frequency (two-tailed paired t test, *p=0.0306), 2) response latency (two-tailed paired t test,
959 **p=0.0067), 3) return time (two-tailed paired t test, **p=0.0033), and 4) duration in nest (Two-tailed paired t test,
960 *p=0.0315).

961

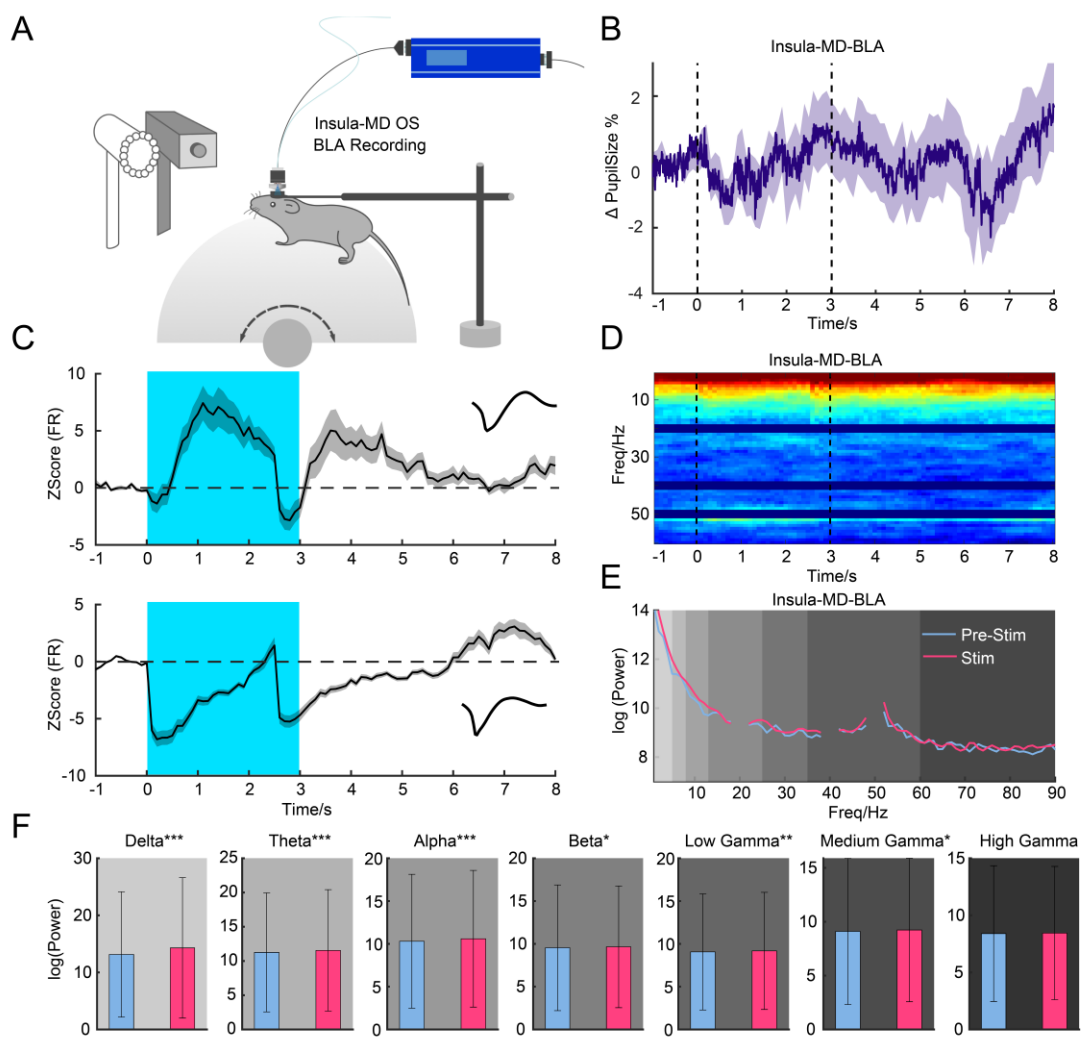
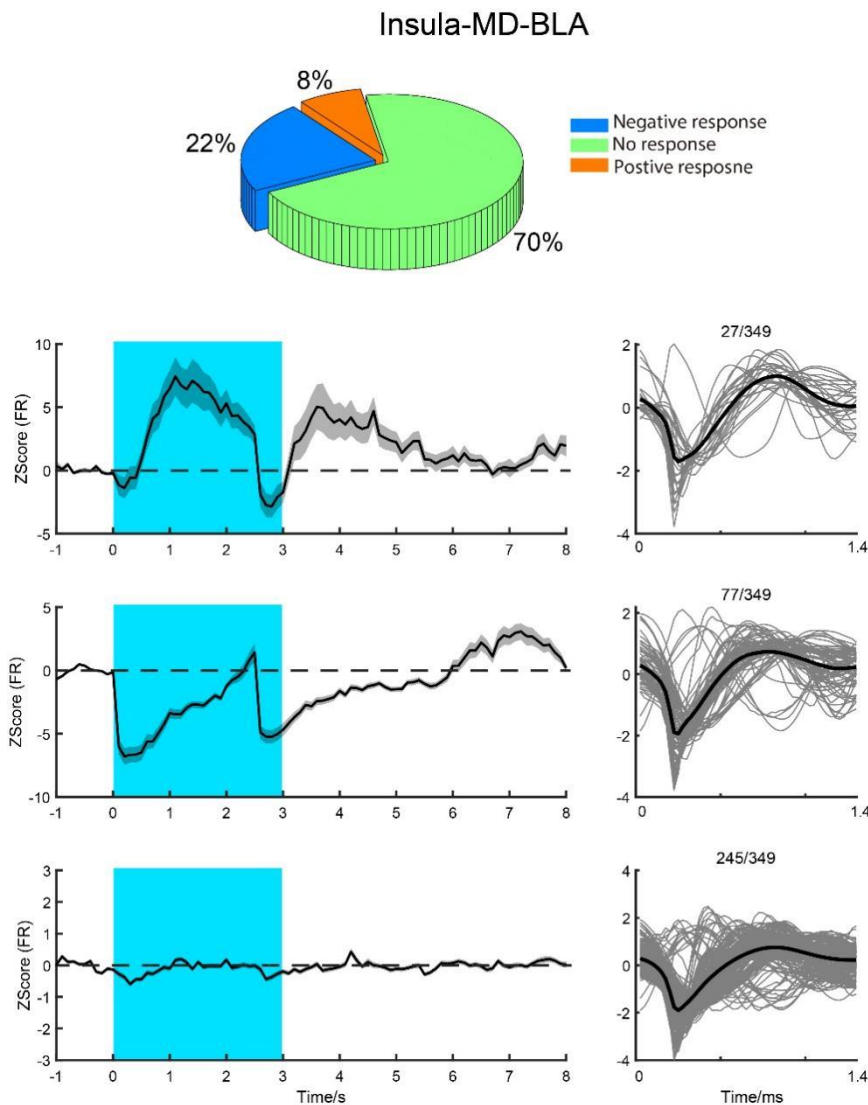
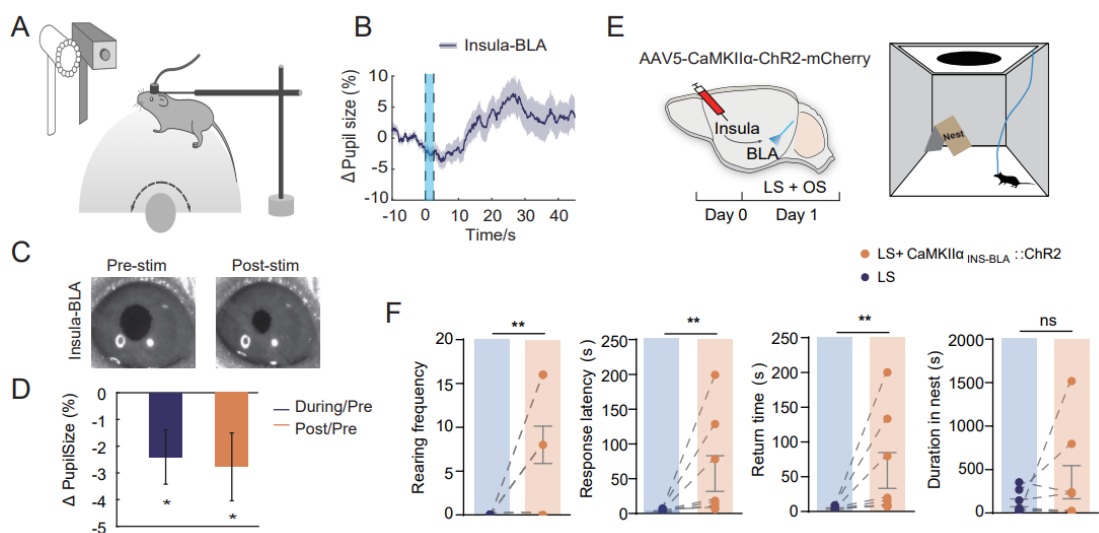


Figure 6 Insula-MD pathway modulate oscillations in the BLA

- 963 (A) Schematic showing electrophysiological recording in the BLA following OS of VTA-projecting and MD-projecting insula neurons.
- 964 (B) Graph showing normalized pupil size during OS (inside the two black dashed lines).
- 965 (C) Graph showing the firing rate of neurons recorded in the BLA during OS. Examples show two types of neuron (excitation and inhibition; spike waveforms are shown above) that were modulated by optogenetic stimulation (blue shaded region).
- 966 (D) Time course of LFP power in alpha and gamma band (optical stimulation starts and ends between black dotted lines).
- 967 (E) Averaged LFP spectrograms recorded in the BLA during OS (inside the two black lines)
- 968 (F) Bar graph showing the comparison between the LFP power in different frequency bands before, during and after optogenetic stimulation (no significant difference)





986

987 **Figure 7 Influence of Insula-BLA Pathway on Arousal and Escape Behavior**

988 (A) Schematic paradigm showing the pupillometry recording set-up.

989 (B) Graph showing the percentage of change in pupil size 10 s before OS, 2.5 s during OS, and 45 s after OS.

990 (C) Representative image showing pupil diameter 10 s before OS, 2.5 s during OS and 2.5 s after OS.

991 (D) Bar graph showing change in pupil size During/Pre OS (Two-tailed paired t test, *p=0.0195) and Post/Pre OS
992 (Two-tailed paired t test, *p=0.0294).

993 (E) Schematic showing the OS paradigm and the LS set-up

994 (F) Measurements were taken during OS (10 trials/mouse) and LS of CaMKII α insula-MD:: ChR2 mice. Bar graphs
995 showing 1) rearing frequency (two-tailed paired t test, **p=0.0072), 2) response latency (Wilcoxon matched-
996 pairs signed rank test, **p=0.0078), 3) return time (Wilcoxon matched-pairs signed rank test, **p=0.0078), and
997 4) duration in nest (two-tailed paired t test, p>0.05).

998

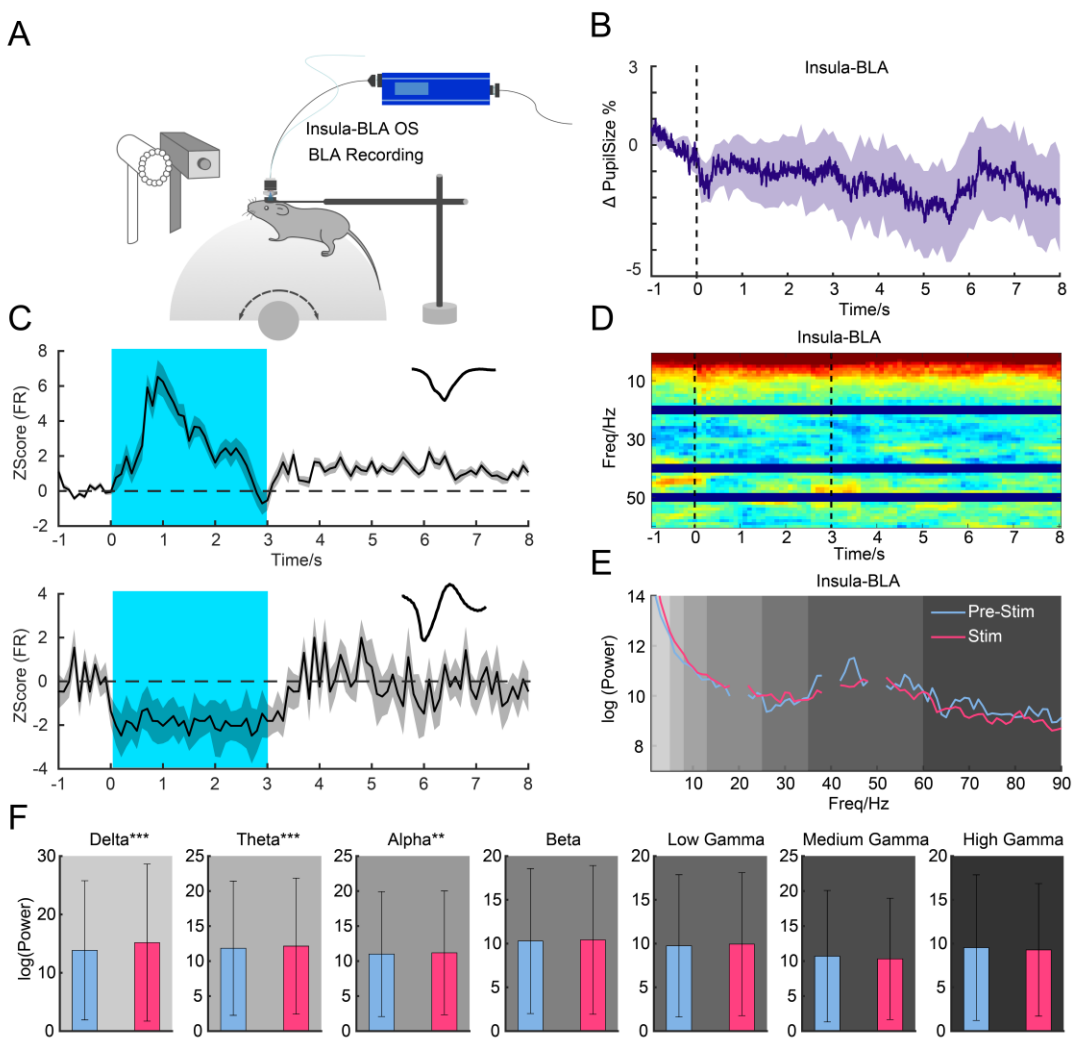


Figure 8 Insula-BLA pathway modulate oscillation in the BLA

(A) Schematic showing electrophysiological recording of neurons in the BLA during OS of the insula BLA pathway .

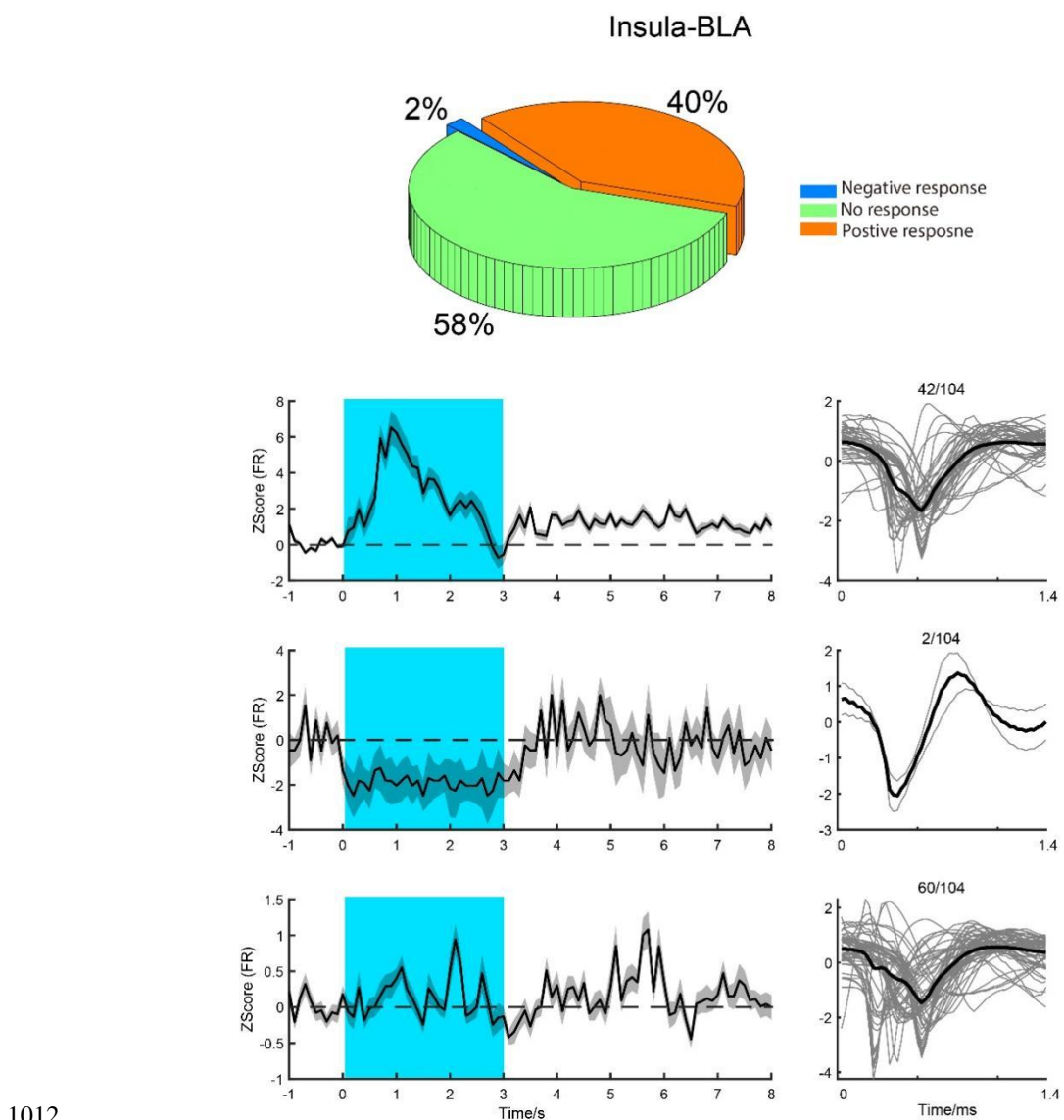
(B) Graph showing normalized pupil size during OP (inside the two black dashed lines) of the insula-BLA pathway.

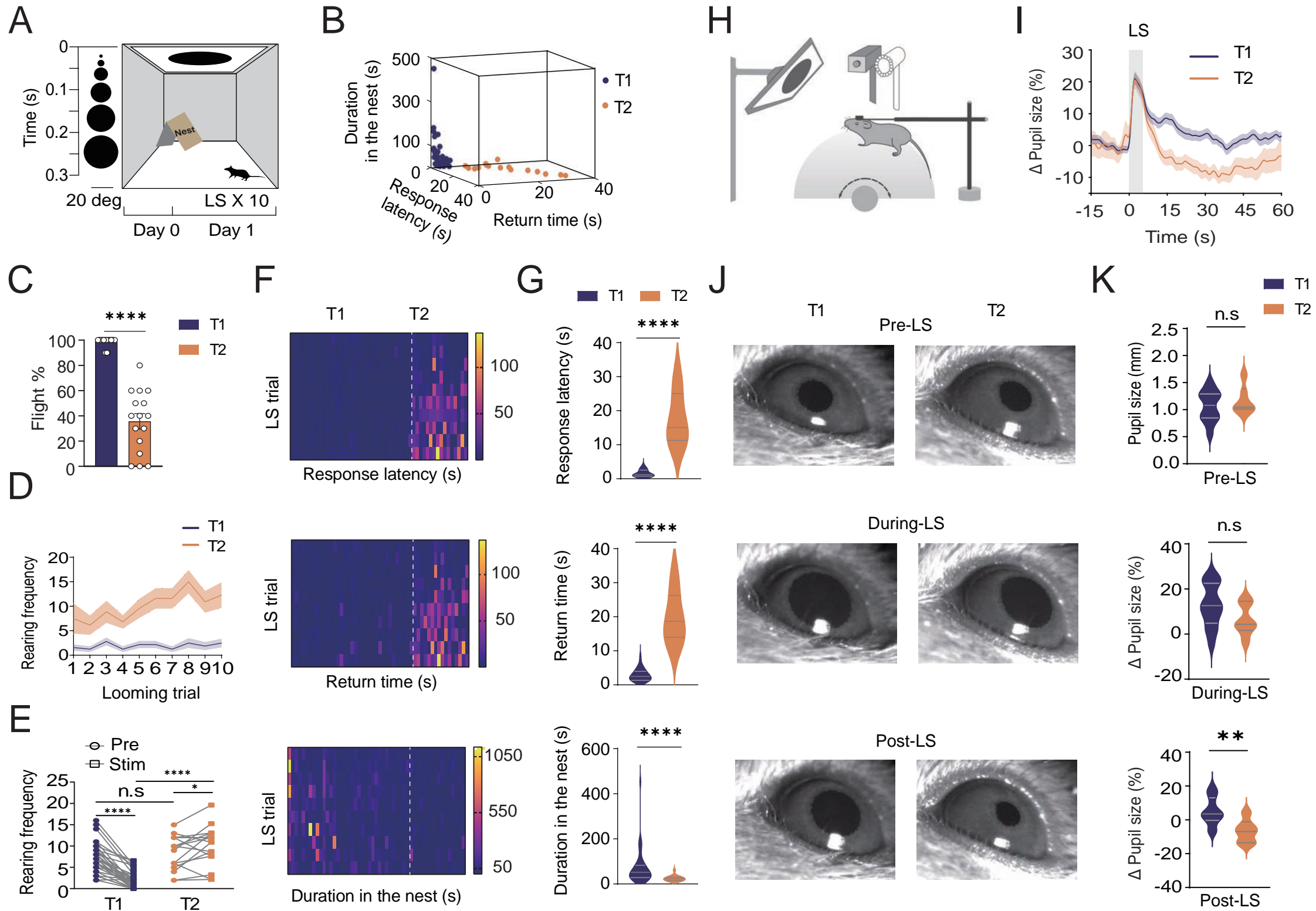
(C) Firing rate of the neurons recorded in BLA during OS. Examples show two types of neuron (excitation and inhibition; spike waveforms are shown above) that were modulated by optogenetic stimulation (blue region, optogenetic stimulation).

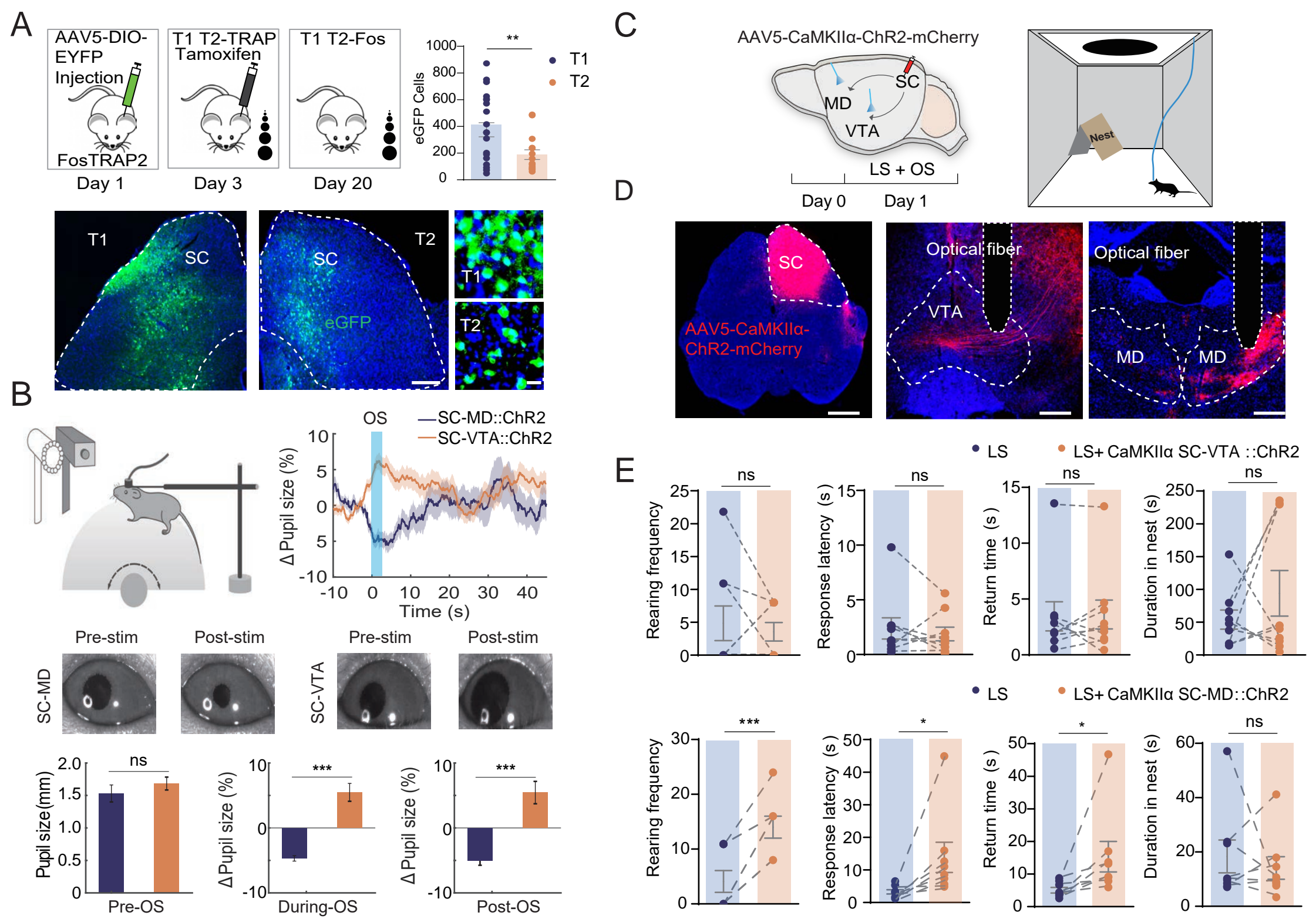
(D) Time course of LFP power in alpha and gamma band (OS inside the two black lines).

(E) Averaged spectrogram of LFP recorded in the BLA during OS (inside the two black lines).

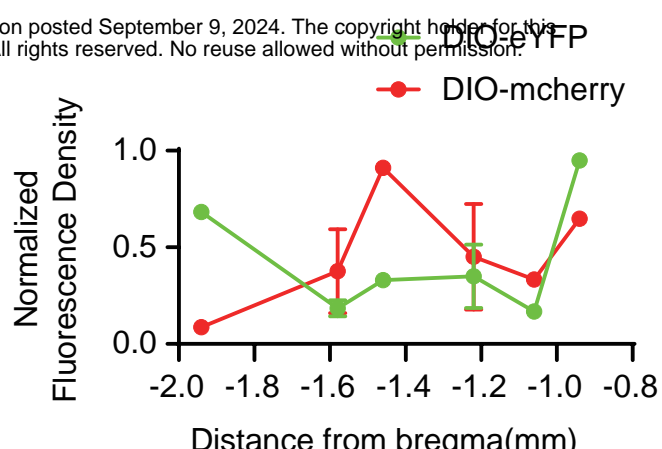
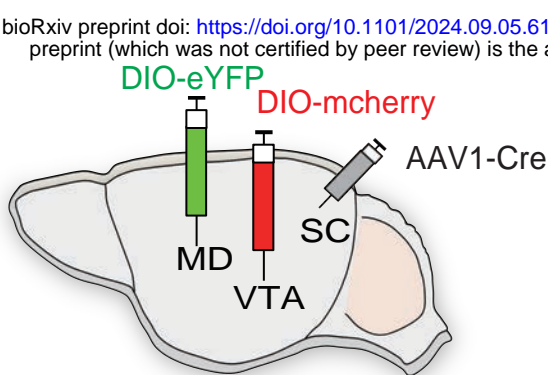
(F) Bar graph showing the comparison between the LFP power in different frequency bands before, during and after optogenetic stimulation (no significant difference)



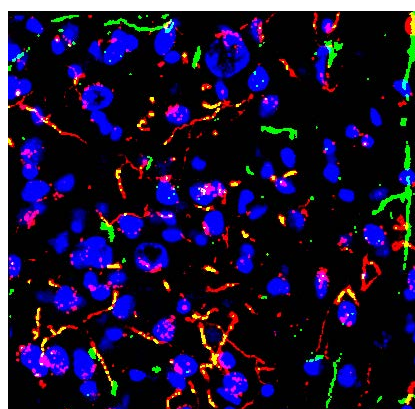
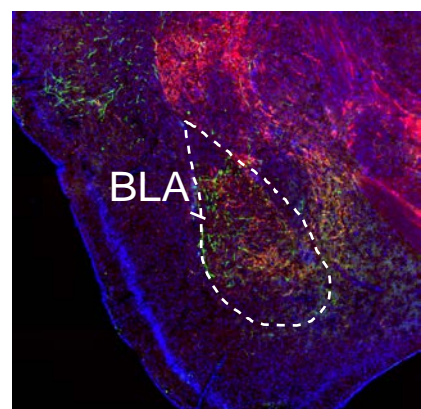
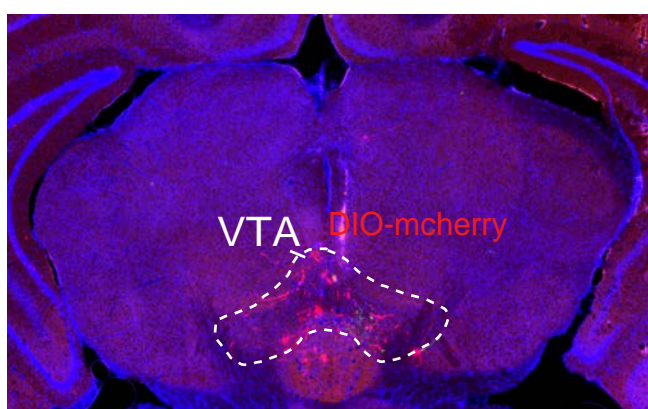
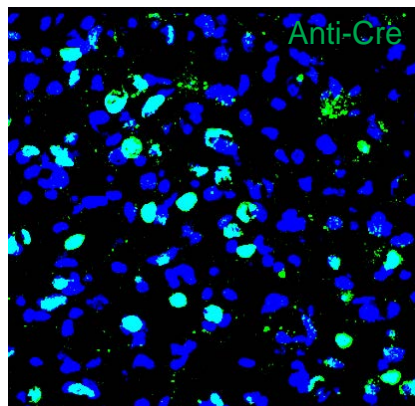
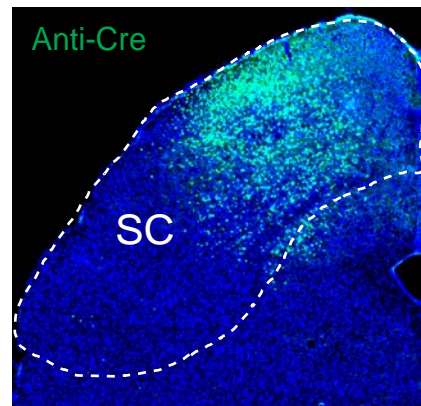
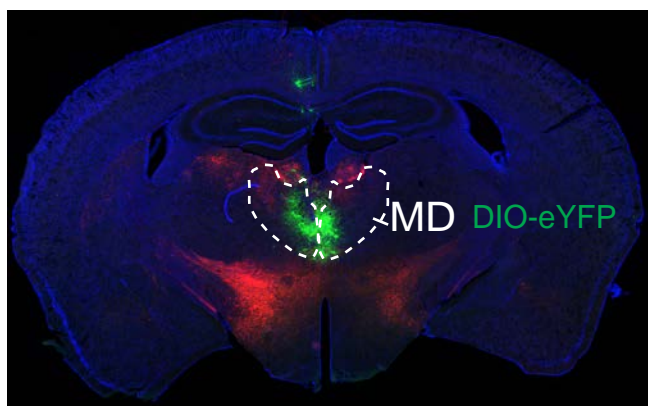


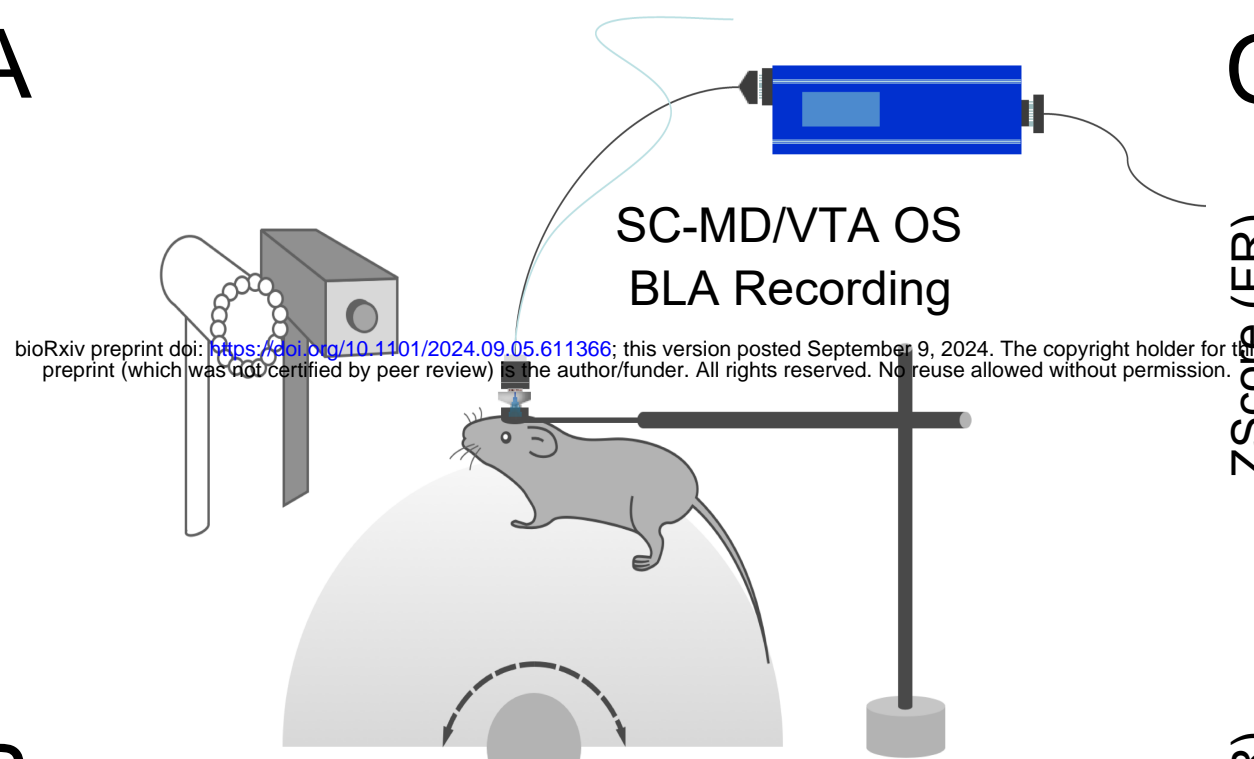
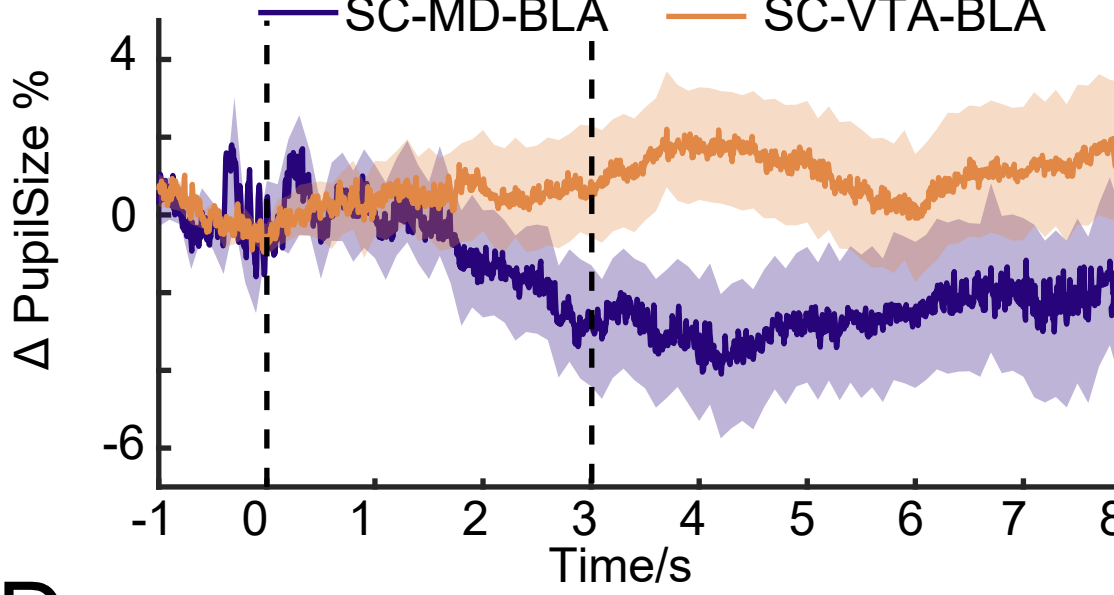
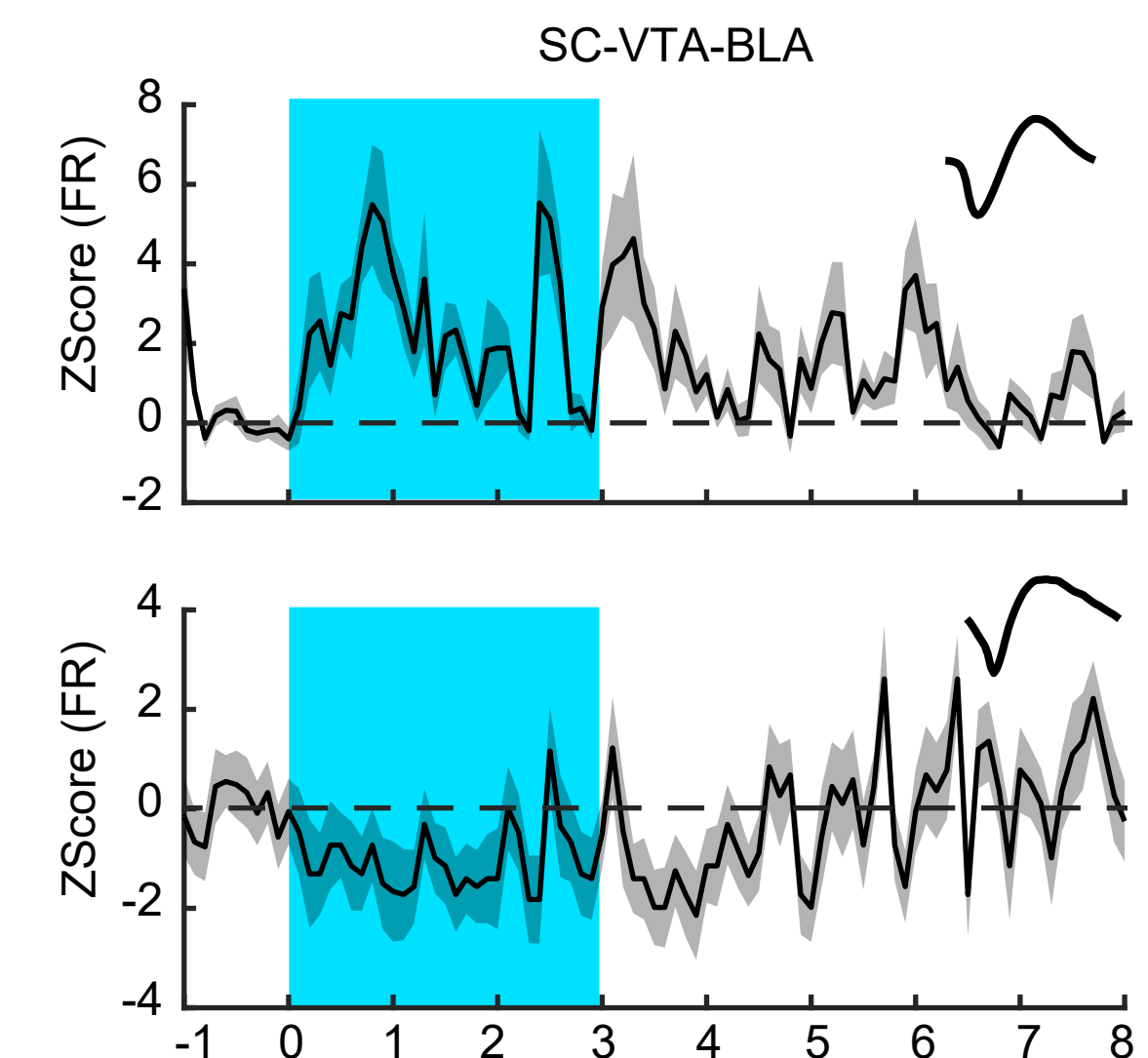
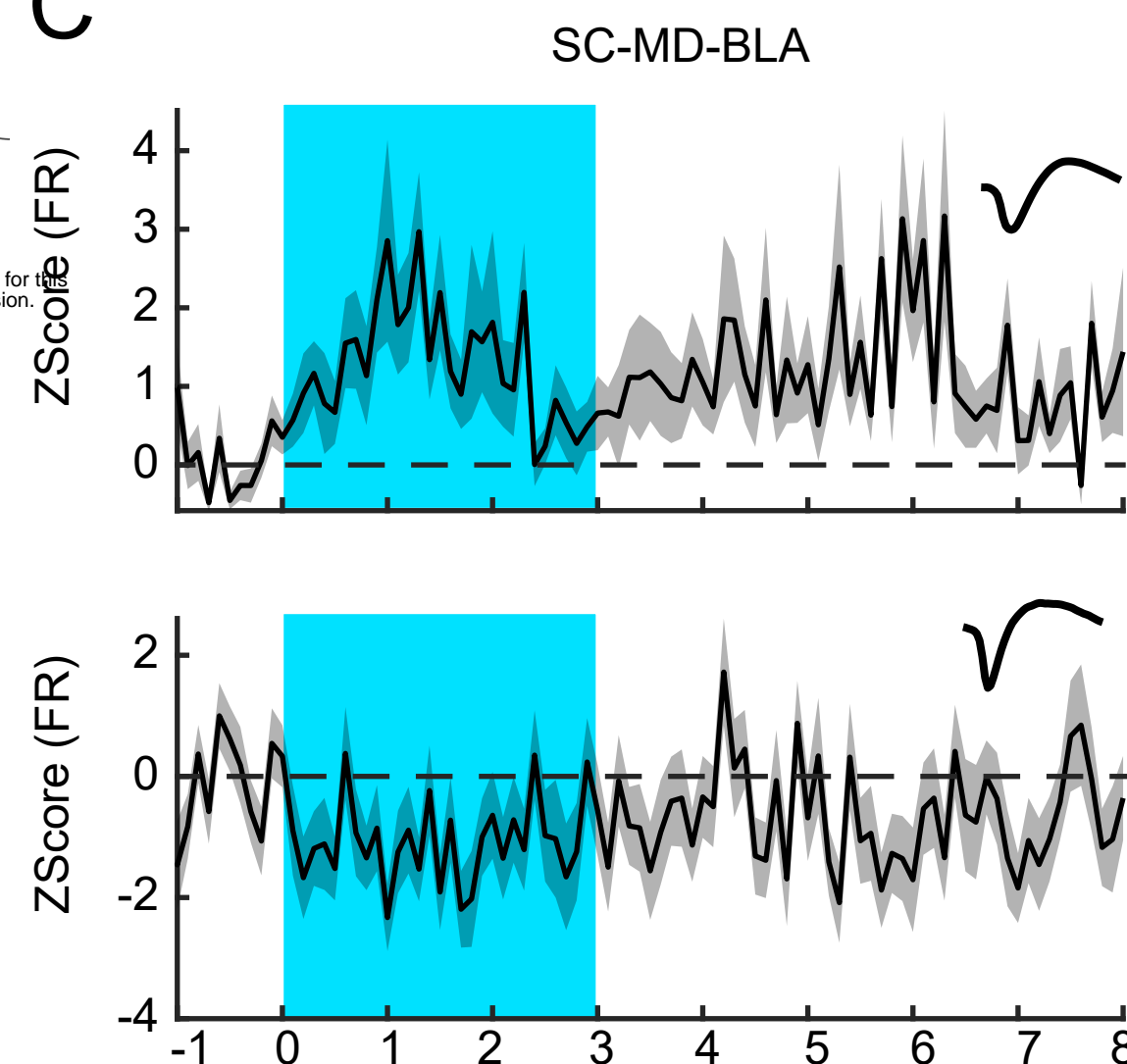
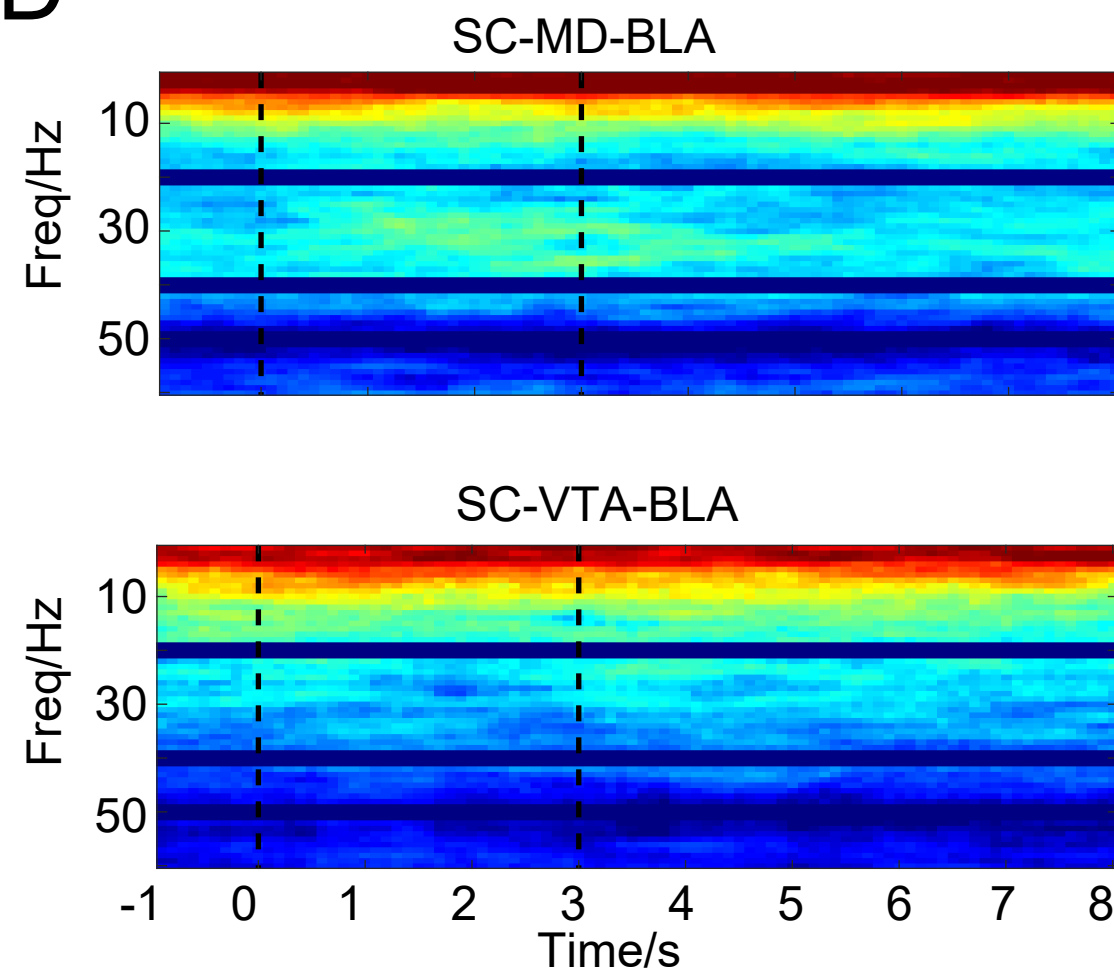
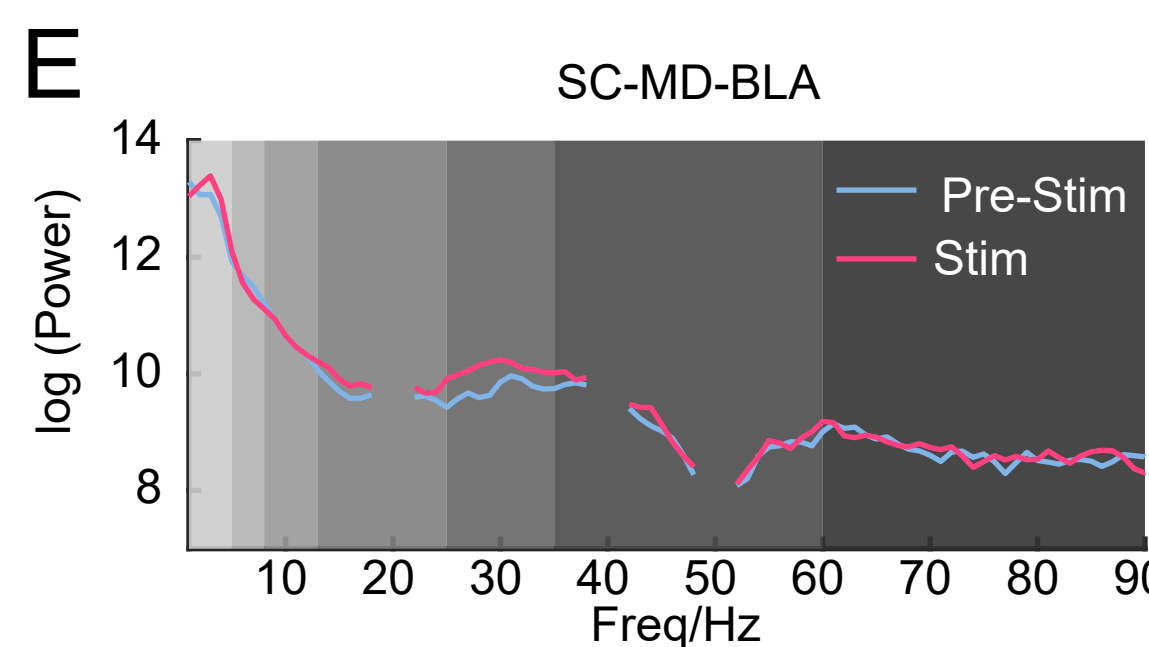
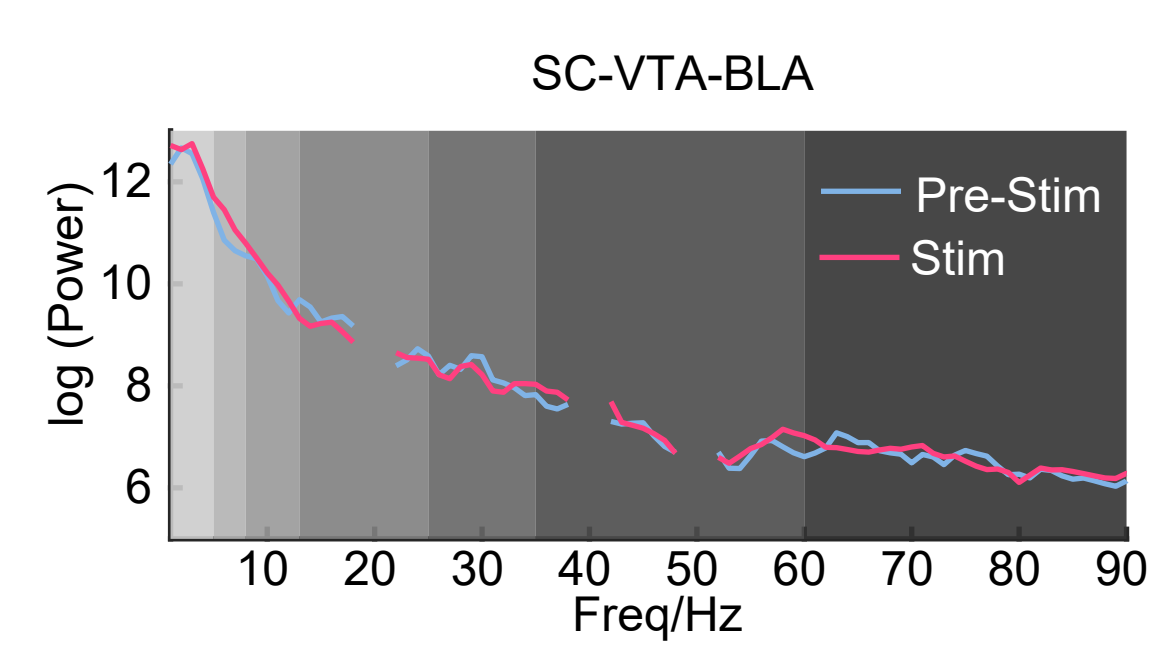
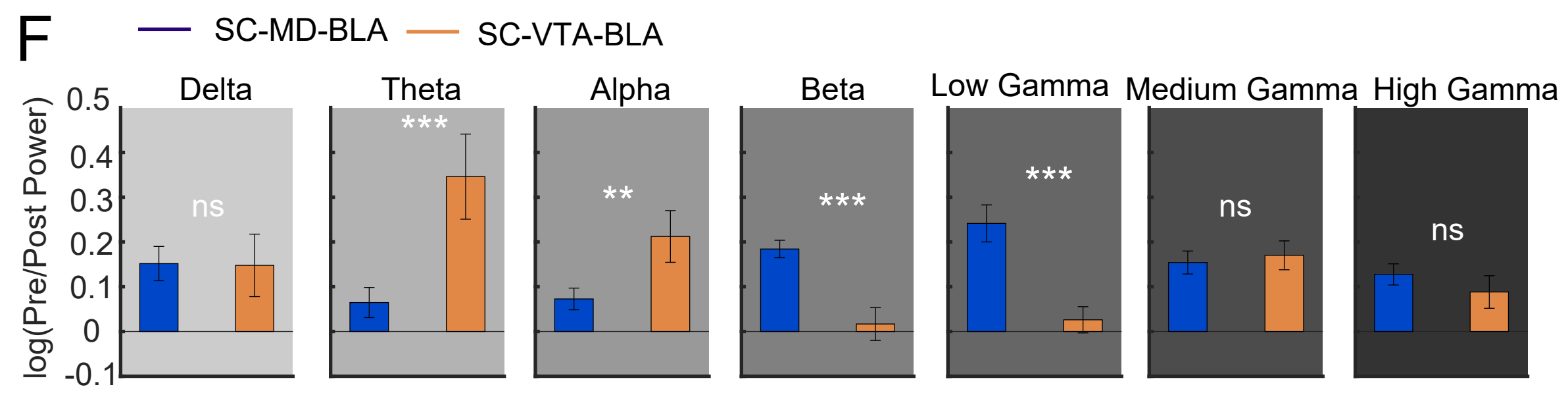


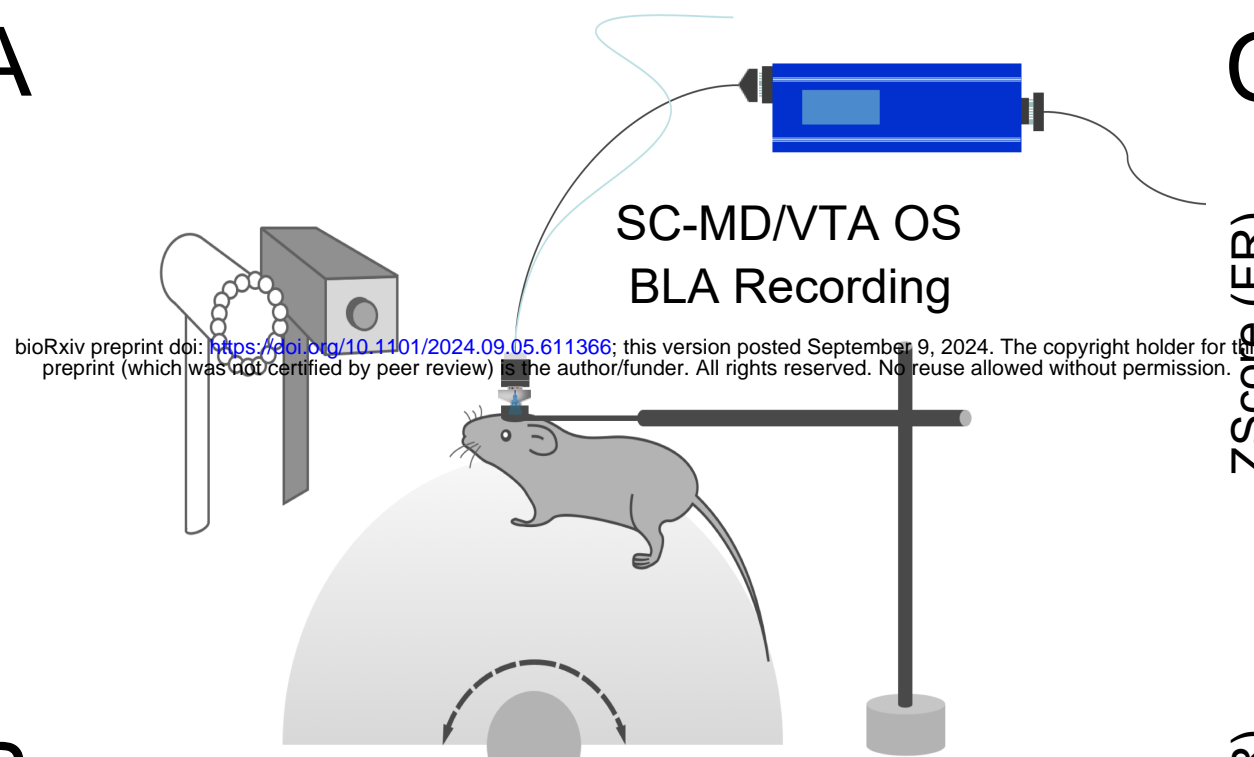
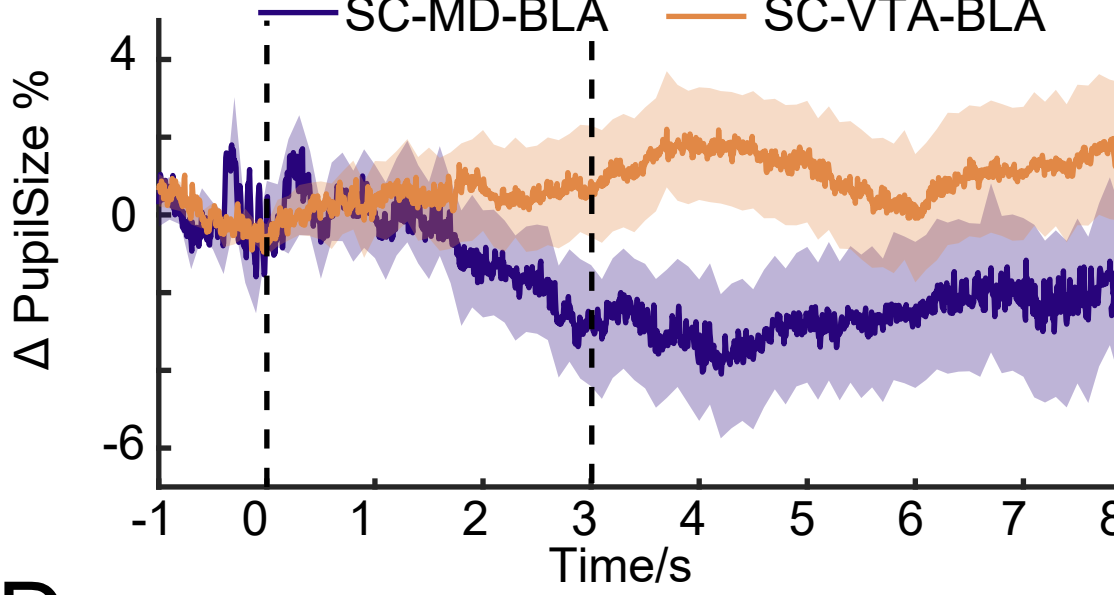
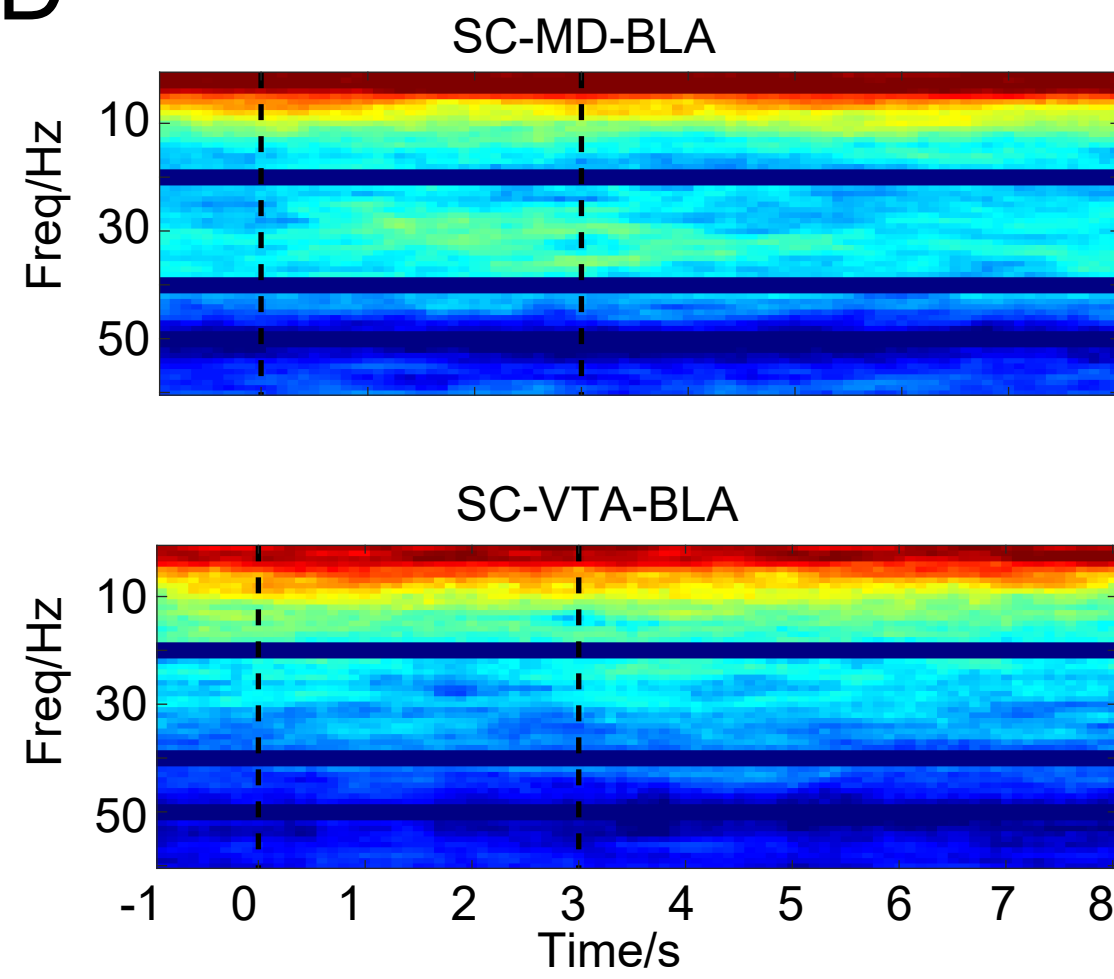
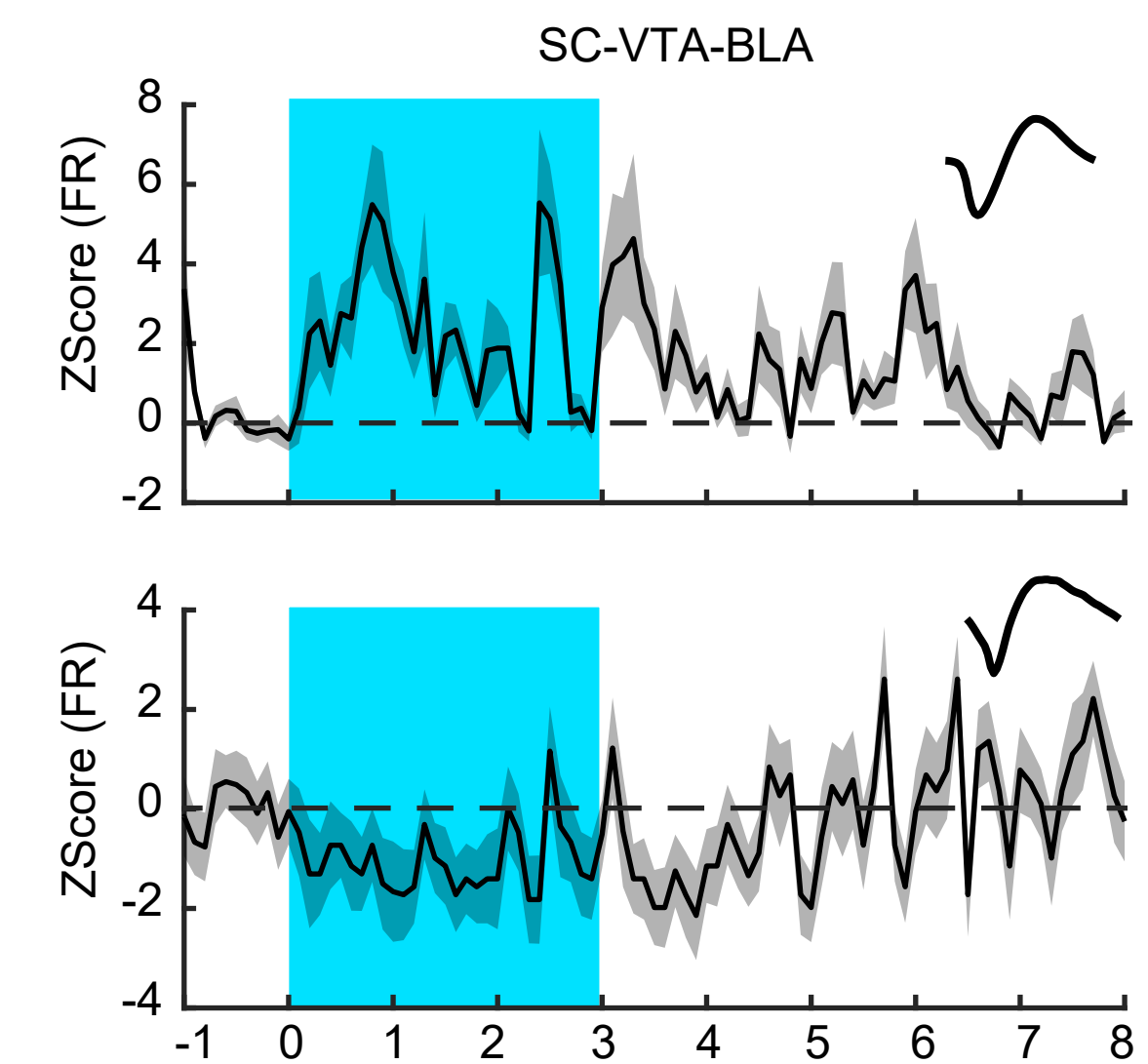
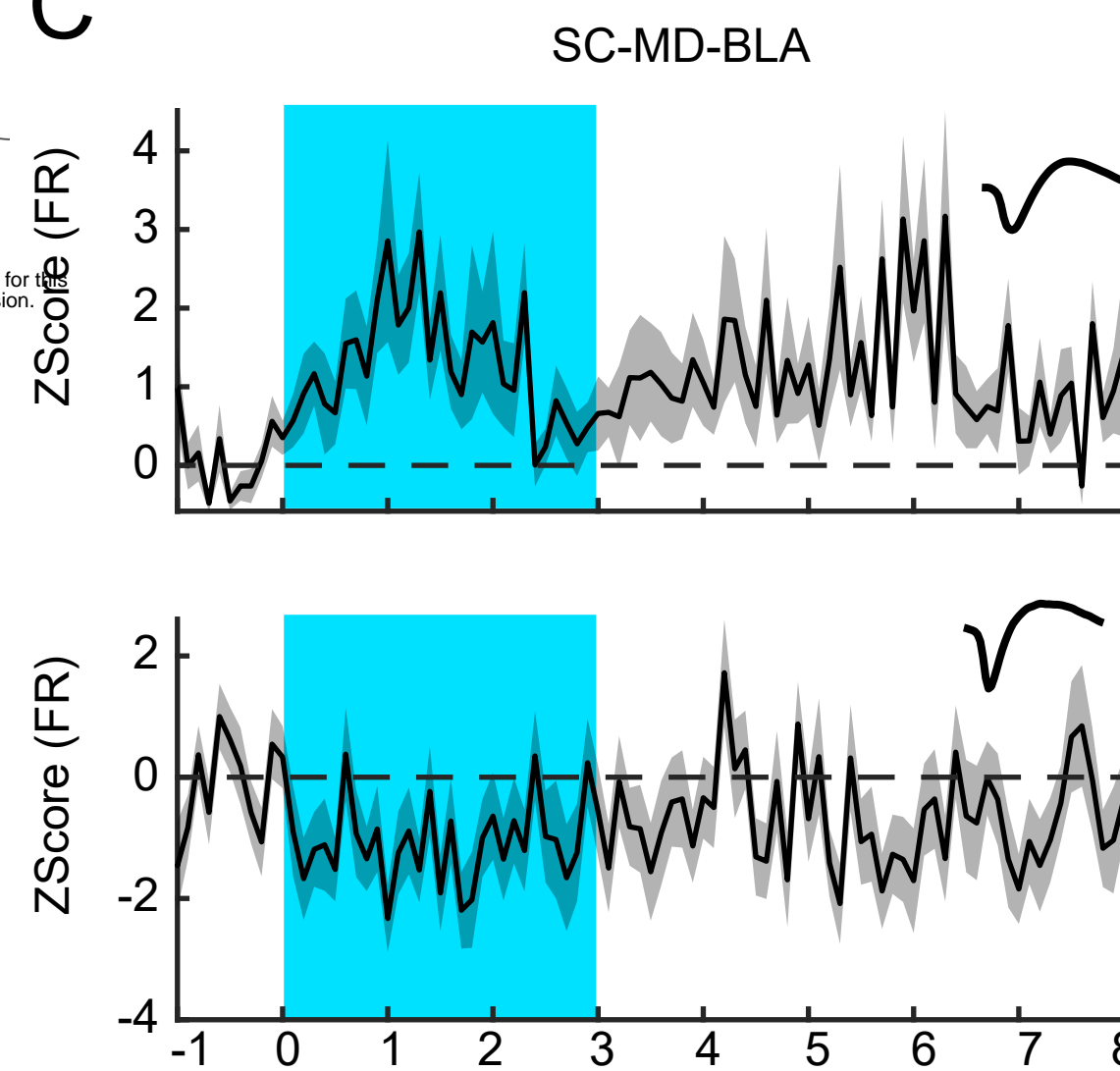
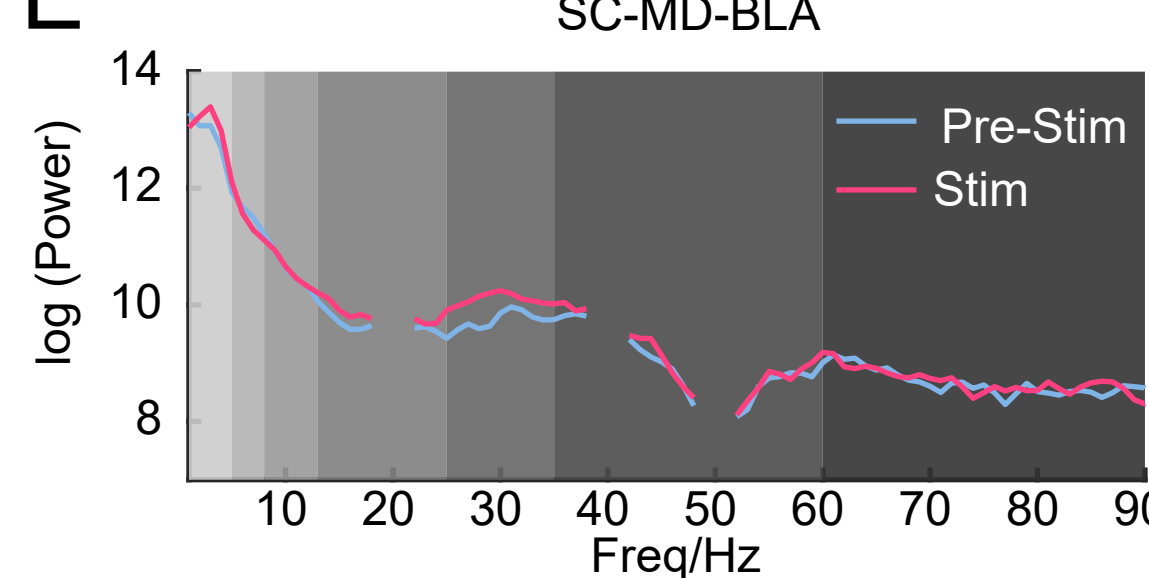
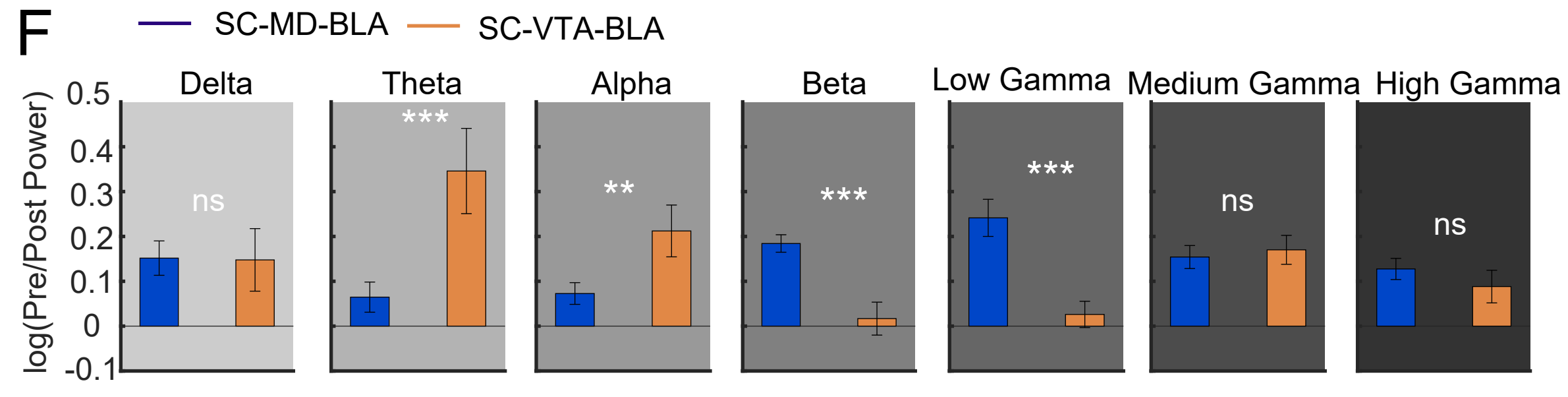
A

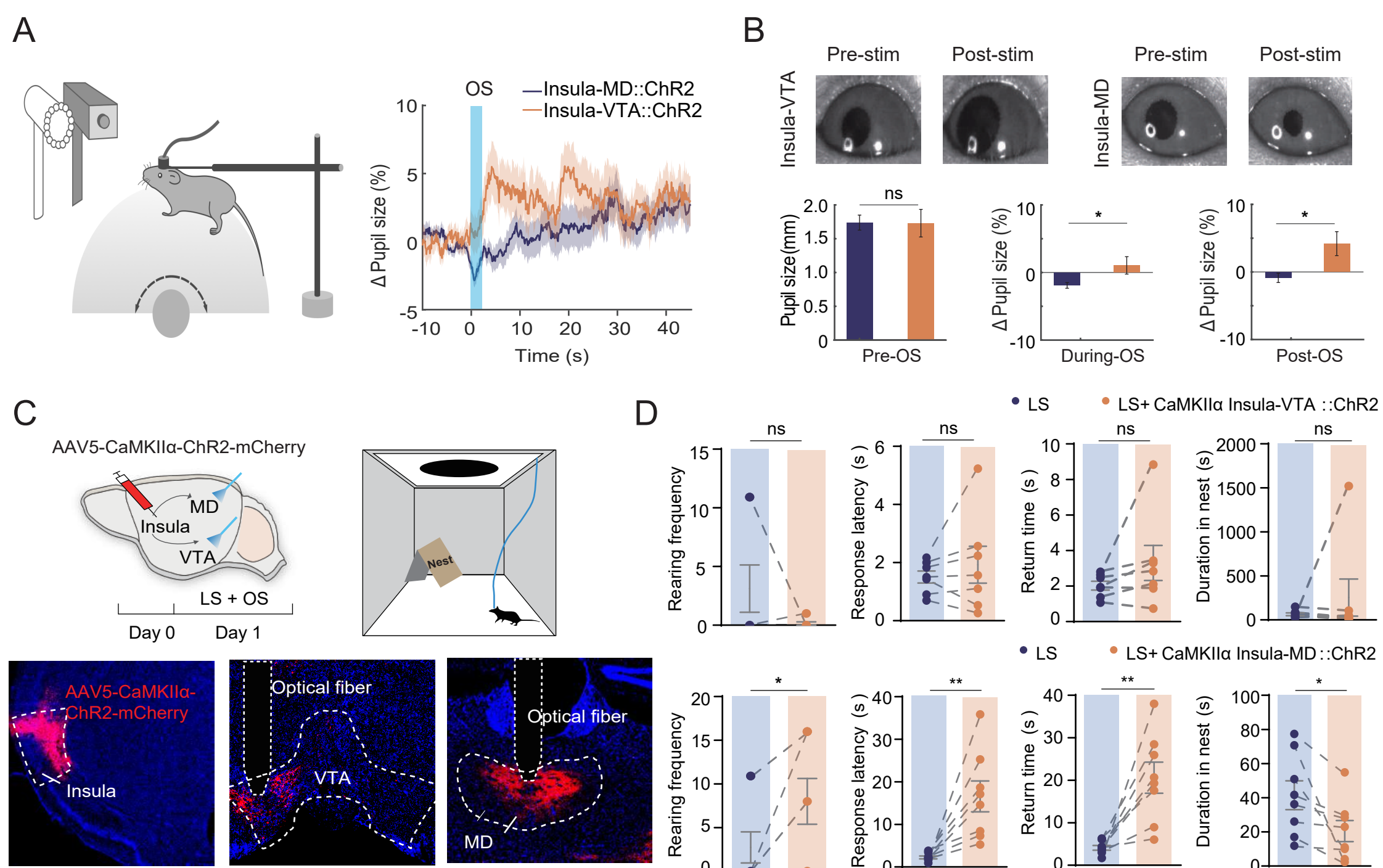


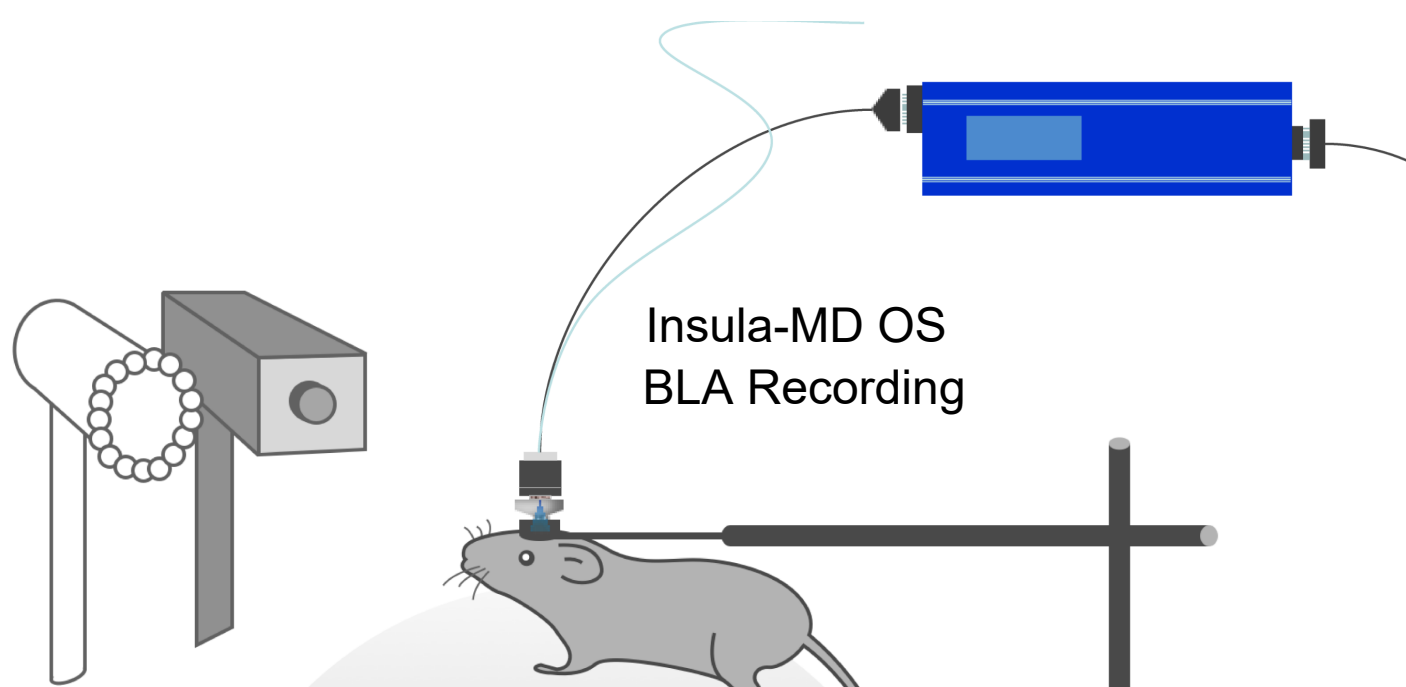
B



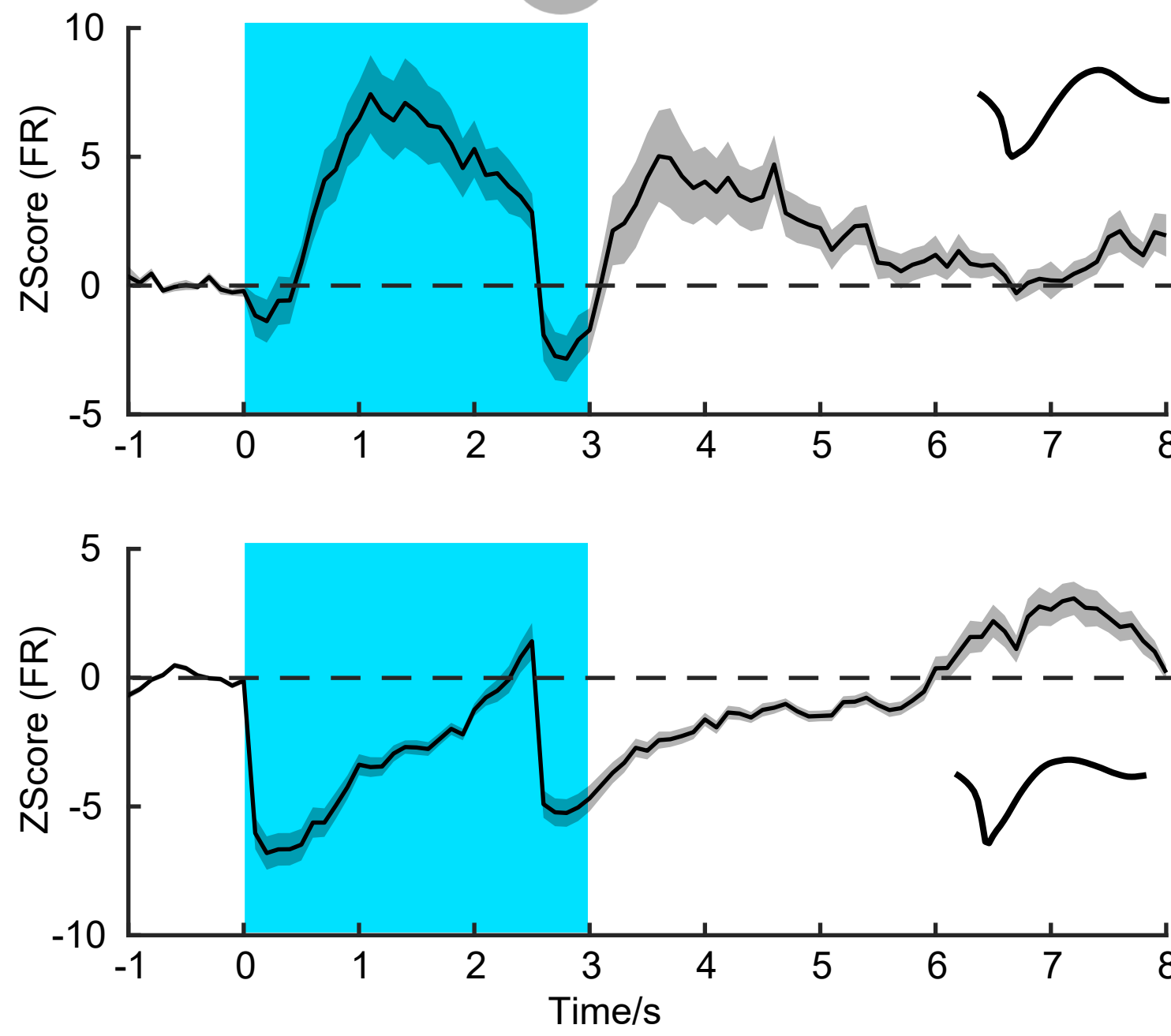
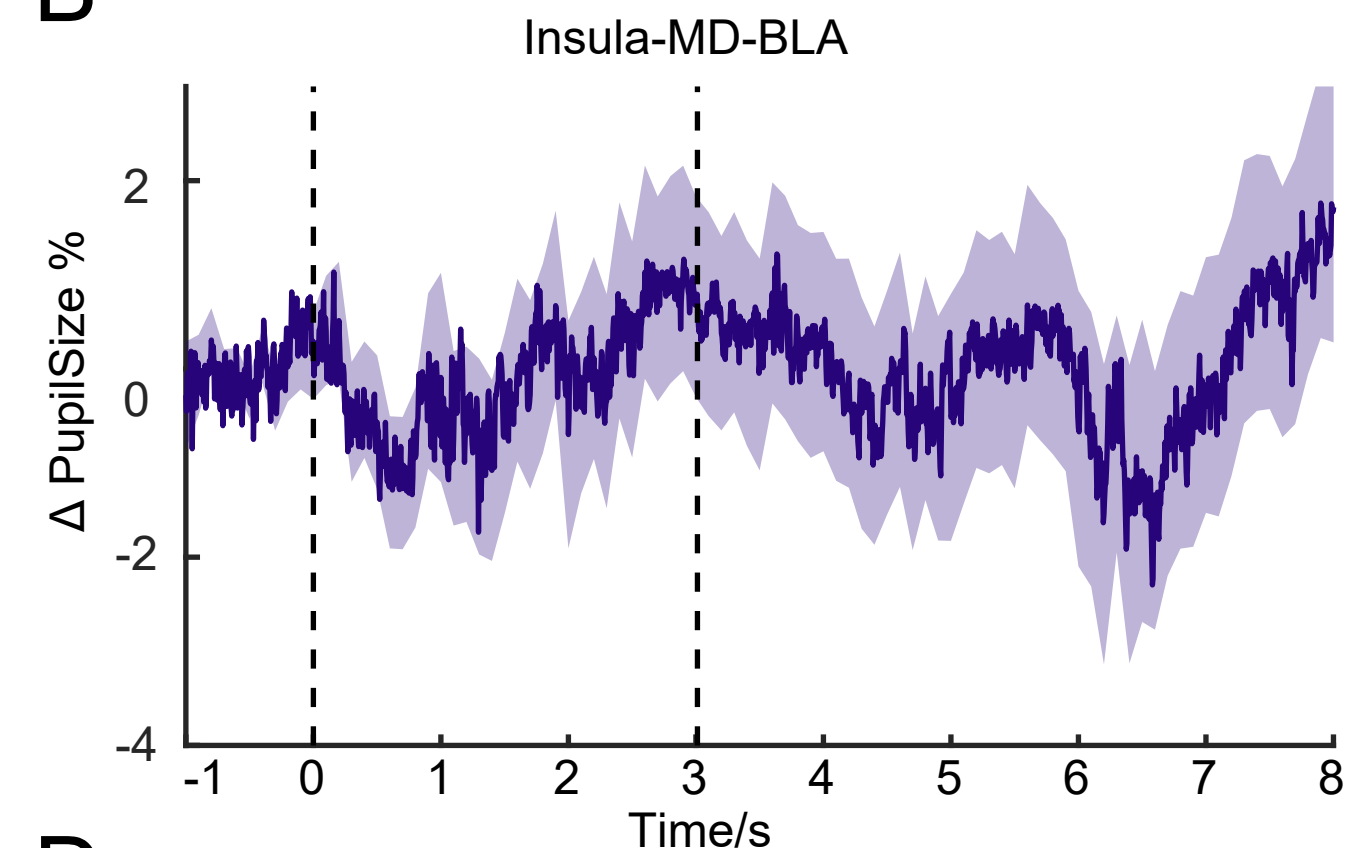
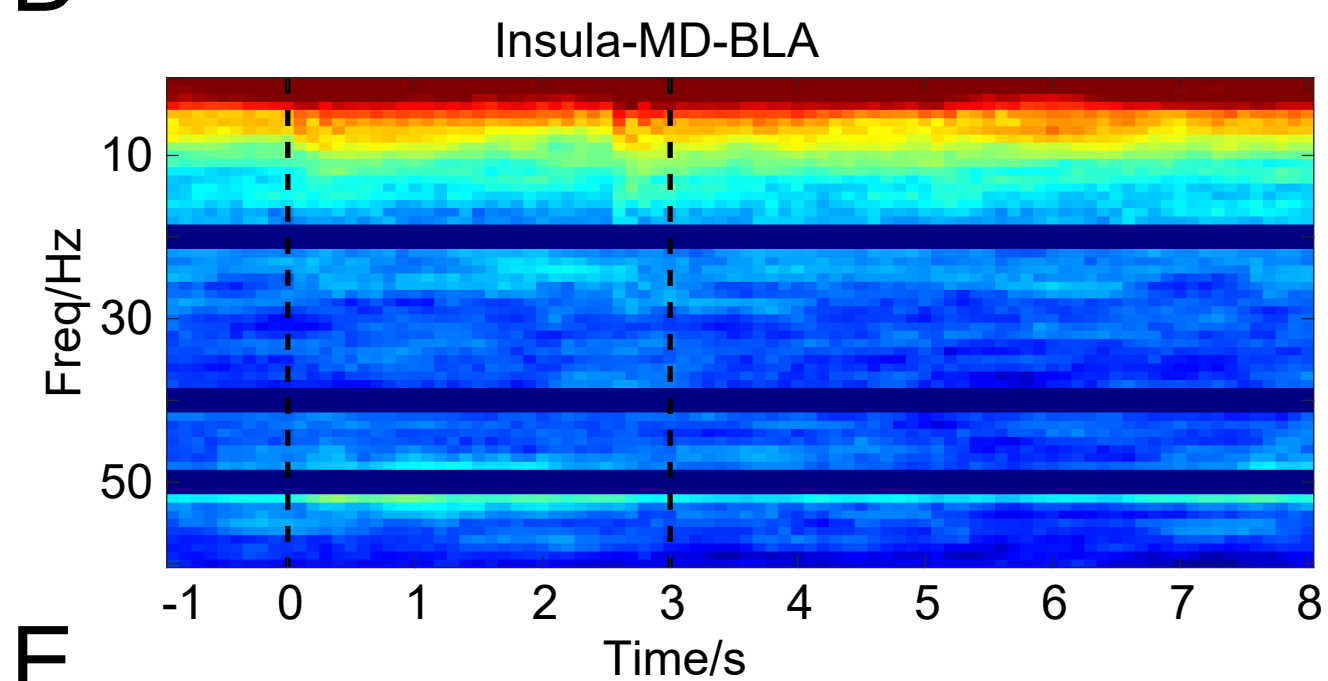
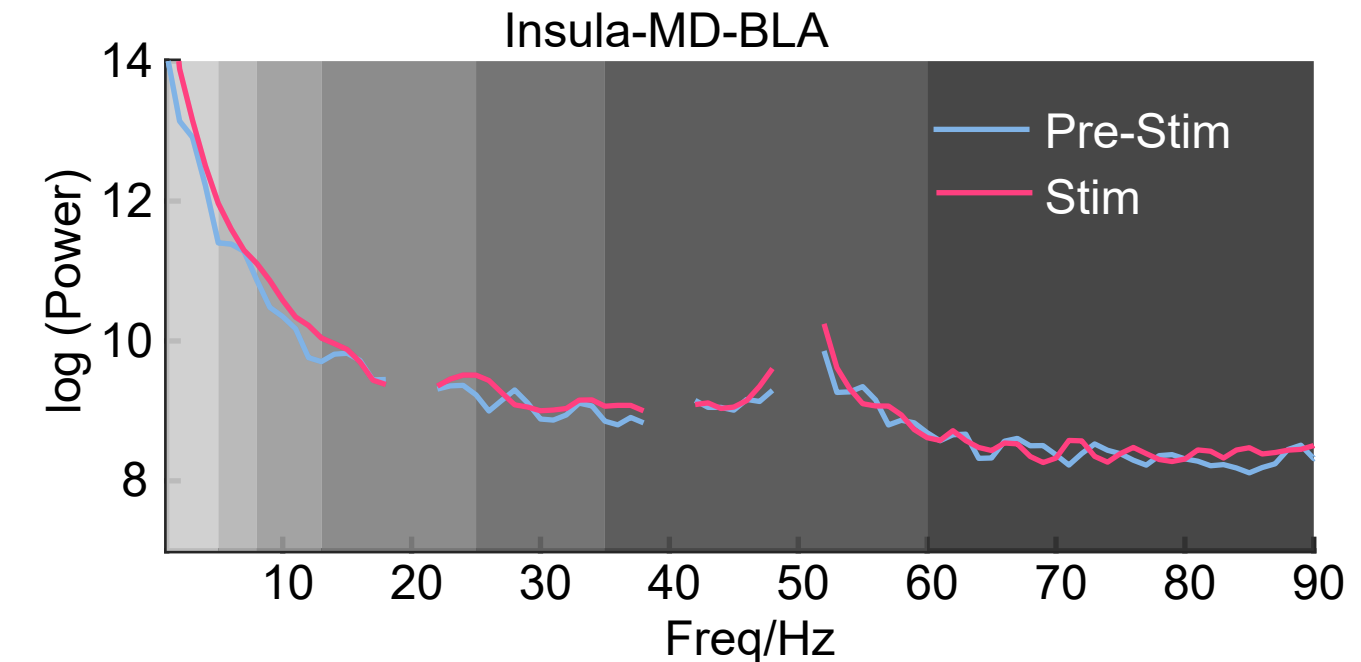
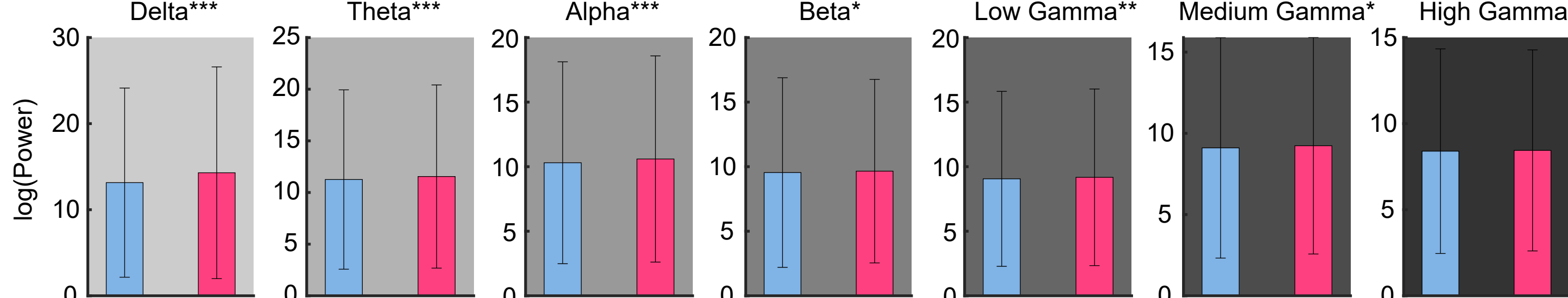
A**B****C****D****E****E****F**

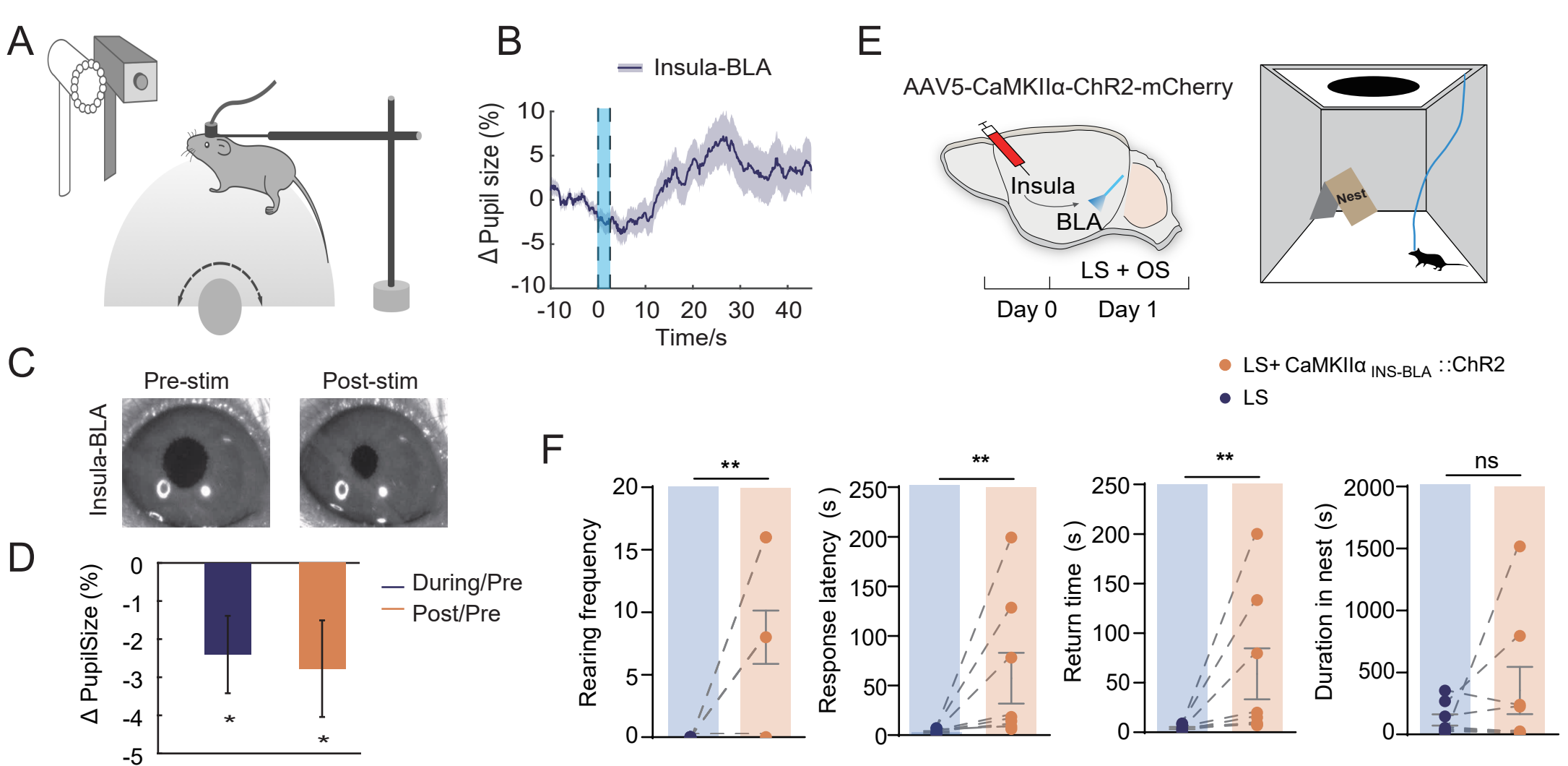
A**B****D****C****E****SC-VTA-BLA****F**

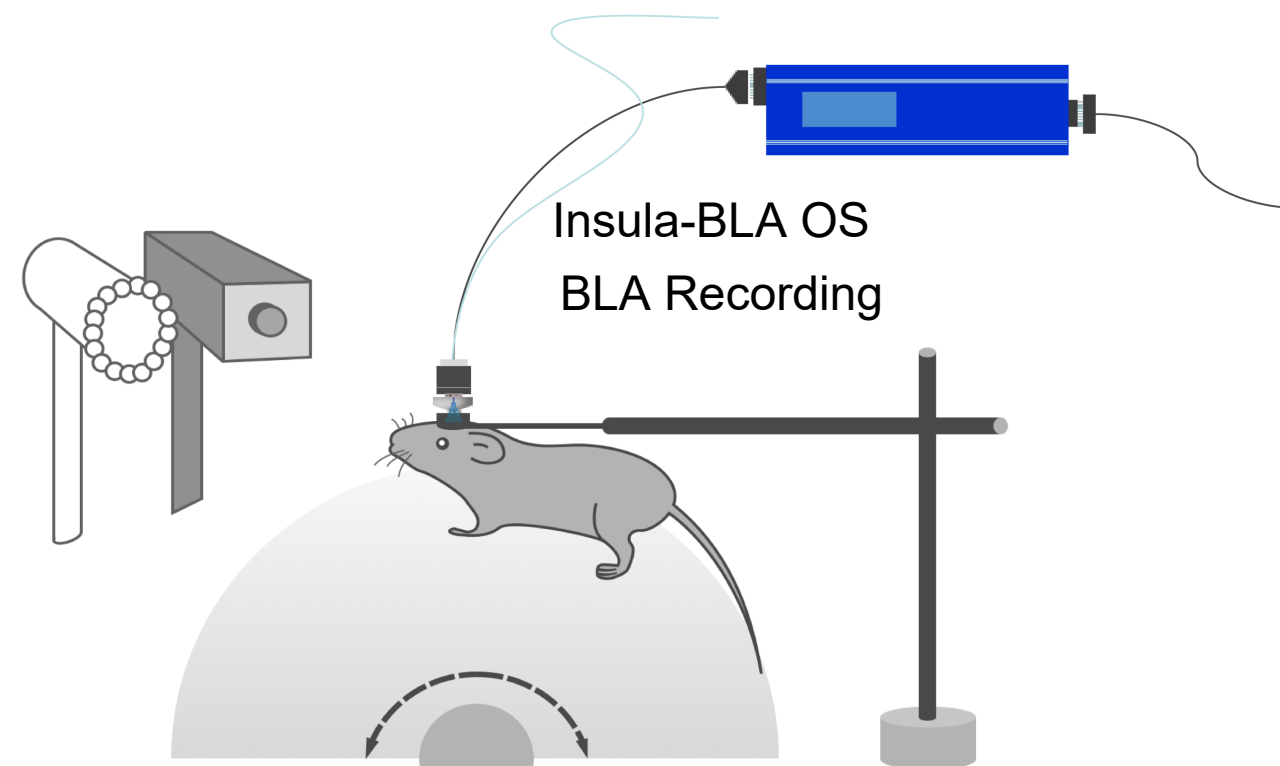
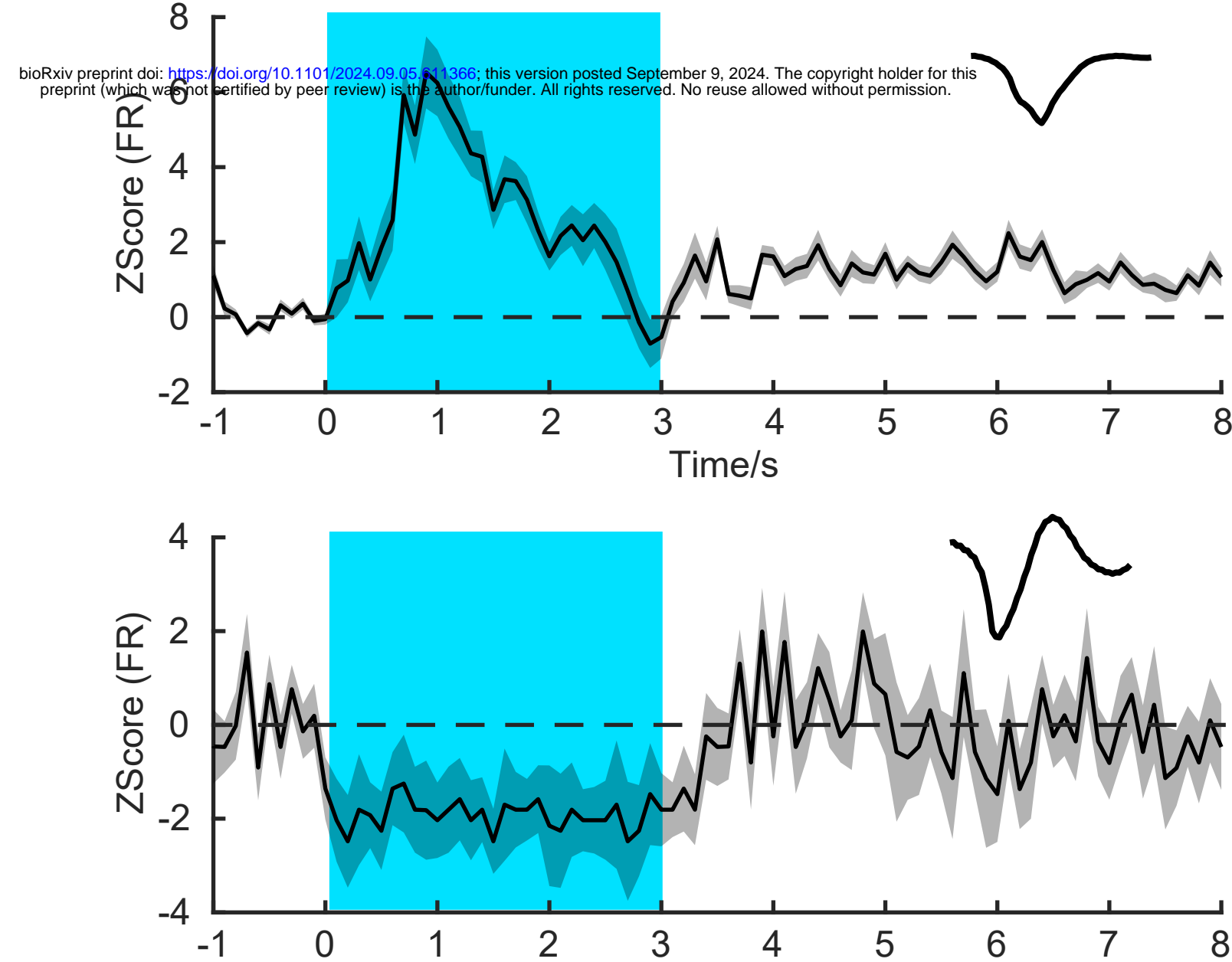
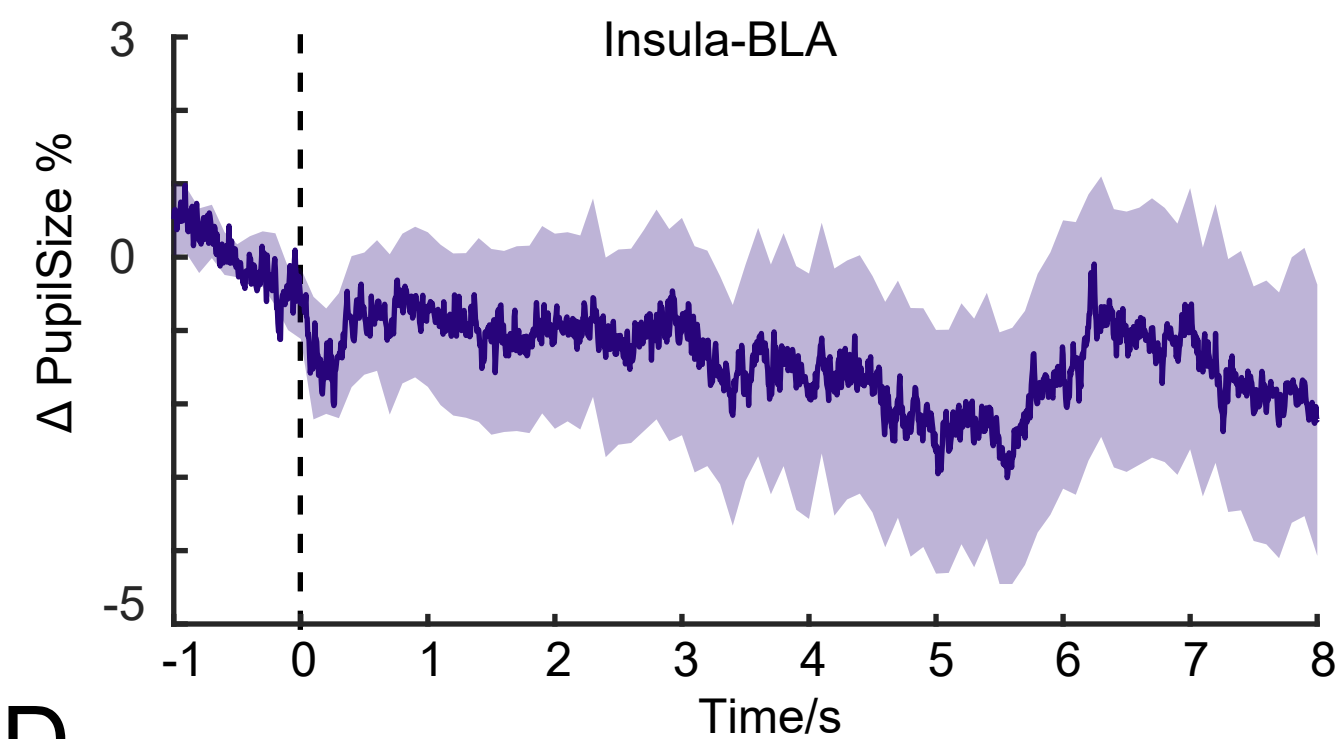
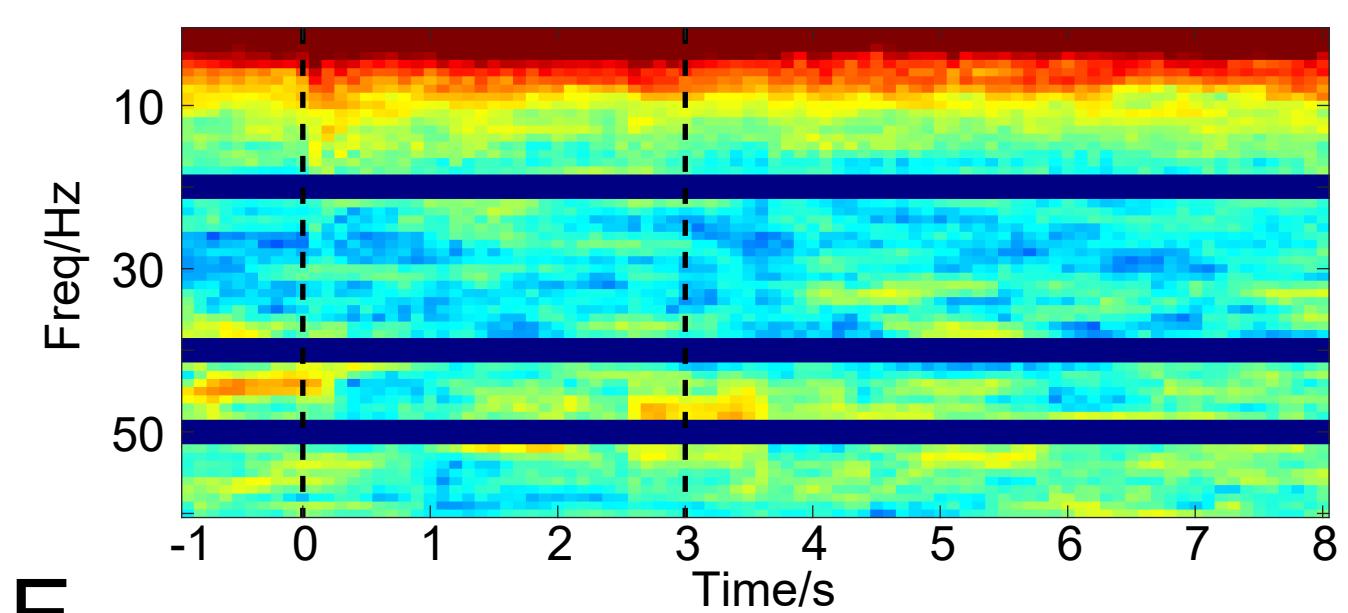
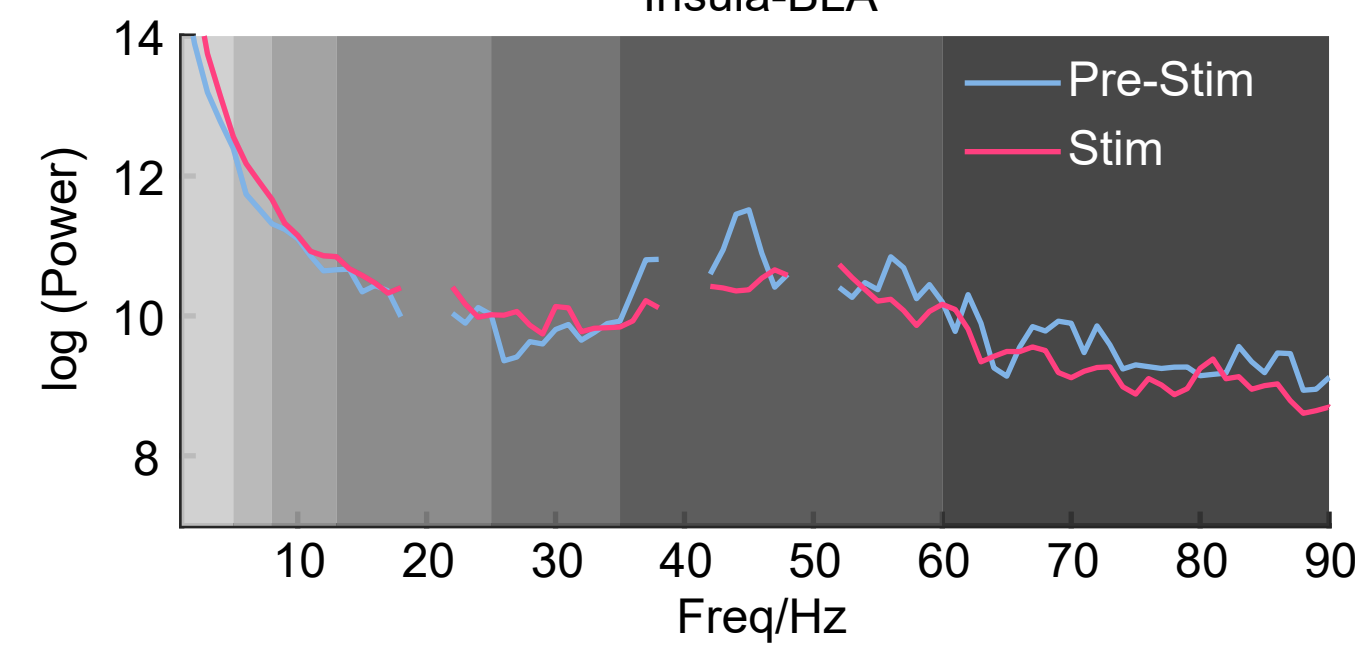


A

bioRxiv preprint doi: <https://doi.org/10.1101/2024.09.05.611366>; this version posted September 9, 2024. The copyright holder for this preprint (which was not certified by peer review) is the author/funder. All rights reserved. No reuse allowed without permission.

C**B****D****E****F**



A**C****B****D****E****F**